V. L. Mironov

**The textbook for students
of the senior courses
of higher educational institutions**

Fundamentals

of Scanning Probe Microscopy

V. L. Mironov

Textbook for students of the senior courses
of higher educational institutions

Fundamentals
of scanning probe microscopy

THE RUSSIAN ACADEMY OF SCIENCES
INSTITUTE FOR PHYSICS OF MICROSTRUCTURES

Nizhniy Novgorod

2004

V. L. Mironov
The textbook for students of the senior courses of higher educational institutions

THE RUSSIAN ACADEMY OF SCIENCES INSTITUTE
FOR PHYSICS OF MICROSTRUCTURES

Nizhniy Novgorod
2004

Abstract

This work is a text-book for senior students, dedicated to one of the most modern technique in the field of surface science: the Scanning Probe Microscopy (SPM). The book takes into account the basic SPM types: Scanning Tunneling Microscopy (STM), Atomic Force Microscopy (AFM), Electric Force Microscopy (EFM), Magnetic Force Microscopy (MFM), Scanning Near-field Optical Microscopy (SNOM), which have found the most widespread application in scientific research activities.

Foreword

This textbook is written on the basis of the course of lectures given by the author in 2002 – 2003 to the students of senior courses of the radiophysical faculty and the Advanced school for general and applied physics faculty with the State University of Nizhny Novgorod. The underlying motive for making this effort, although there is an extensive literature on scanning probe microscopy available today [1-13], was a nearly total lack of educational manuals on the SPM methodology.

The textbook was written within a short period of time (two months, actually) at the request of the NT-MDT company (Moscow, Russia), producer of scanning probe microscopes for scientific research and a special SPM educational system. I admit that within the short time available for completing this work certain drawbacks can't have been avoided and will be grateful to everyone for pointing out possible errors, inaccuracies and for other critical remarks.

The writing of the textbook was in many ways inspired by S.V.Gaponov, Director of the Institute for physics of microstructures of the Russian Academy of Science, corresponding member of the Russian Academy of Science. I express deep gratitude to the IPM RAS employees, D.G.Volgunov, S.A.Treskov and O.G.Udalov, for numerous fruitful discussions; to my wife, G.V.Mironova, for careful proof-reading of the manuscript; to Dr. V.N.Rjabokon (NT-MDT) for critical and constructive reviewing of the Russian version of this book; to Dr. G.Torzo (Research Director at ICIS-CNR University in Padova, Italy) for careful reviewing and correction of the English version. I am also sincerely grateful to the NT-MDT company, especially to V.A.Bykov, V.V.Kotov and A.V.Bykov, for their support of the publishing project.

V.L.Mironov

Introduction

The scanning probe microscopy (SPM) is one of the powerful modern research techniques that allow to investigate the morphology and the local properties of the solid body surface with high spatial resolution. During last 10 years the scanning probe microscopy has turned from an exotic technique accessible only to a limited number of research groups, to a widespread and successfully used research tool of surface properties. Currently, practically every research in the field of surface physics and thin-film technologies applies the SPM techniques. The scanning probe microscopy has formed also a basis for development of new methods in nanotechnology, i.e. the technology of creation of structures at nanometric scales.

The scanning tunneling microscope (STM) is the first in the probe microscopes family; it was invented in 1981 by the Swiss scientists Gerd Binnig and Heinrich Rohrer [14,15]. In their works they have shown, that this is a quite simple and rather effective way to study a surface with spatial resolution down to atomic one. Their technique was fully acknowledged after visualization of the atomic structure of the surface of some materials and, particularly, the reconstructed surface of silicon. In 1986, G.Binnig and H.Rohrer were awarded the Nobel Prize in physics for invention of the tunneling microscope.

After the tunneling microscope creation, atomic force microscope (AFM), magnetic force microscope (MFM), electric force microscope (EFM), scanning near-field optical microscope (SNOM) and many other devices having similar working principles and named as scanning probe microscopes (SPM) have been created within a short period of time. Now the probe microscopy is a rapidly developing area of technology and applied scientific research.

1. The scanning probe microscopy technique

1.1. *Working principles of scanning probe microscopes*

The analysis of a surface micro relief and of its local properties is performed by scanning probe microscopes using specially prepared tips in the form of needles. The size of the working part of such tips (the apex) is about ten nanometers. The usual tip - surface distance in probe microscopes is about $0.1 - 10$ nanometers. Various types of interaction of the tip with the surface are exploited in different types of probe microscopes. For example the tunnel microscope is based on the phenomenon of a tunneling current between a metal needle and a conducting sample; various types of interactive force underlie the working mechanism of atomic force, magnetic force and electric force microscopes. We will consider the common features inherent to various probe microscopes. Let the interaction of a tip with a surface be characterized by some parameter P.

If there is a sharp enough and unique (single valued) dependence $P = P\ (z)$ of that parameter on the tip-sample distance, then P can be used in the feedback system (*FS*) that control the distance between the tip and the sample. A block-diagram of the feedback system in scanning probe microscope is shown on Fig. 1.
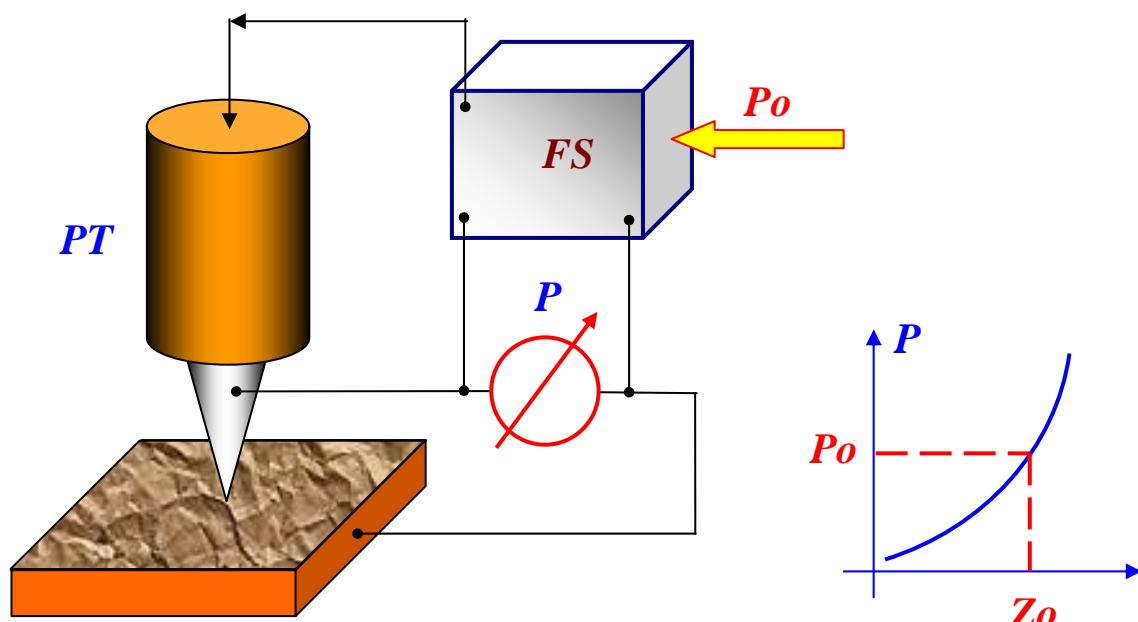

Fig. 1. The block diagram of the feedback system in a probe microscope

The feedback system keeps constant the value of the parameter P (equal to the value Po , set by the operator). If the tip-sample distance changes, there is a change in the parameter P. In the feedback system a differential signal is amplified and fed to the piezo transducer (*PT*) that controls the tip-sample separation. The transducer uses the signal ΔP to change the separation, bringing it back to the initial value, corresponding to a differential signal close to zero. Thus it is possible to control the tip-sample distance with high accuracy. In existing probe microscopes the accuracy in the tip-surface distance control reaches the value of ~ 0.01 Å. During tip movement along the sample surface the sample topography induces changes in the interaction parameter P. The feedback system restores the preset value of the tip-sample distance (i.e. of the interaction parameter Po) in

real time, so that when the tip is moved to a point *x,y* over the sample, the signal *V(x,y)* fed to the transducer is proportional to the local departure of the sample surface from the ideal plane *X,Y(z = 0)*. This makes possible to use the values *V(x,y)* to map the surface topography, ad to obtain an SPM image. During scanning the tip first moves above the sample along a certain line (line scan), thus the value of the signal fed to the transducer, proportional to the height value in the surface topography, is recorded in the computer memory. Then the tip comes back to the initial point and steps to the next scanning line (frame scan), and the process repeats again. The feedback signal recorded during scanning is processed by the computer, and then the SPM surface topography image *Z = f (x,y)* is plotted by means of computer graphics. Alongside with investigation of the sample topography, probe microscopes allow to study various properties of a surface: mechanical, electric, magnetic, optical and many others.

1.2. Scanning elements (scanners)

It is necessary to control the working tip-sample distance and to move the tip over the sample surface with high accuracy (at a level of Angstrom fractions) in order to make the probe microscopes properly working. This problem is solved with the help of special transducers, or scanning elements (scanners). The probe microscope scanners are made of piezoelectric materials. Piezoelectric materials change their sizes in an external electric field. The inverse piezoeffect equation for crystals is as follows:

$$u_{ij} = d_{ijk} E_k ,$$

where u_{ij} is the deformation tensor, E_k are the electric field components, d_{ijk} are the components of piezoelectric tensor. The piezoelectric coefficients are defined by the type of crystal symmetry.

Transducers made from piezoceramic materials are widely used in various technical applications. The piezoceramics is polarized polycrystalline material obtained by powder sintering from crystal ferroelectrics. Polarization of ceramics is performed as follows. The ceramic is heated up above its Curie temperature T_c (for the majority of piezoceramics T_c <300°C), and then it is slowly cooled in a strong electric field (about 3 kV/cm). After cooling below Tc, piezoceramic retains the induced polarization and gets the ability to change its sizes (by increasing or reducing it depending on the mutual direction of the polarization vector and the vector of the applied electric field). The basic characteristics of ceramic materials used in technical equipment can be found in the book [16]. The piezoelectric tensor for piezoceramics has only three coefficients, which are not zero: d_{33}, d_{31}, d_{15}, describing respectively the longitudinal, the cross (with respect to the polarization vector) and the shift deformations. We shall consider a flat piezoceramic plate (Fig. 2) in an external field. Let the polarization vector $\vec{P}$ and the vector of the applied electric field $\vec{E}$ be directed both along the X axis. Then, designating $d_{||} = d_{33}$ and $d_{\perp} = d_{31}$, we get that the piezoceramic deformation in the direction parallel to the field is $u_{xx} = d_{||} E_x$, and in the direction perpendicular to the field it is $u_{rr} = d_{\perp} E_x .$
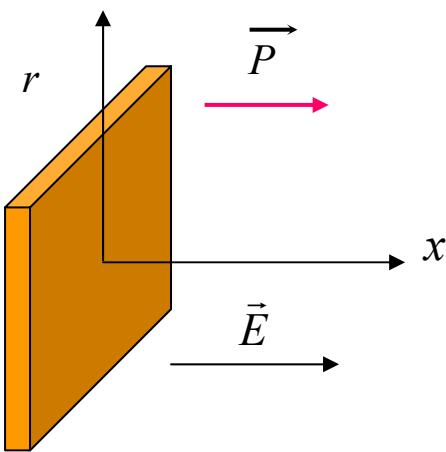
Fig. 2. Piezoceramic plate in an external electric field

Tubular piezoelements (Fig. 3) are widely used in scanning probe microscopy. They allow obtaining large enough movements with rather small control voltages. Tubular piezoelements are hollow thin-walled cylinders with electrodes (thin metal layers), plated on the external and internal tube surfaces, and the end tube faces remain uncovered.
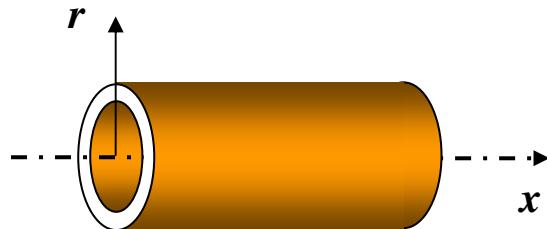
Fig. 3. Tubular piezoelement

Under the influence of a potential difference between internal and external electrodes the tube changes its length. The relative longitudinal deformation under the influence of a radial electric field can be written as:

$$u_{xx} = \frac{\Delta x}{l_0} = d_\perp E_r,$$

where l_0 is the length of the unstressed tube. The absolute lengthening of the piezo-tube is :

$$\Delta x = d_\perp \frac{l_0}{h} V,$$

where h is the thickness of the tube wall, V is the potential difference between internal and external electrodes. Thus, for the same applied voltage, the tube lengthening will be larger, for longer and thinner tubes.

Assembly of three tubes into one unit (Fig. 4) allows to produce precise movements in three mutually perpendicular directions. Such scanning element is referred to as tripod.
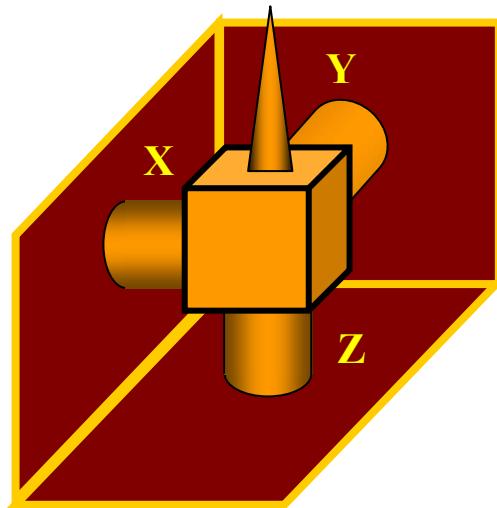
Fig. 4. Scanning element as tripod, assembled on tubular piezoelements

The drawbacks of such scanner are the complexity of manufacturing and the strong asymmetry of its structure. Today the scanners made of one tubular element are most widely used in scanning probe microscopy. The structure of a tubular scanner and the arrangement of electrodes are presented in Fig. 5. The polarization vector is radially directed.
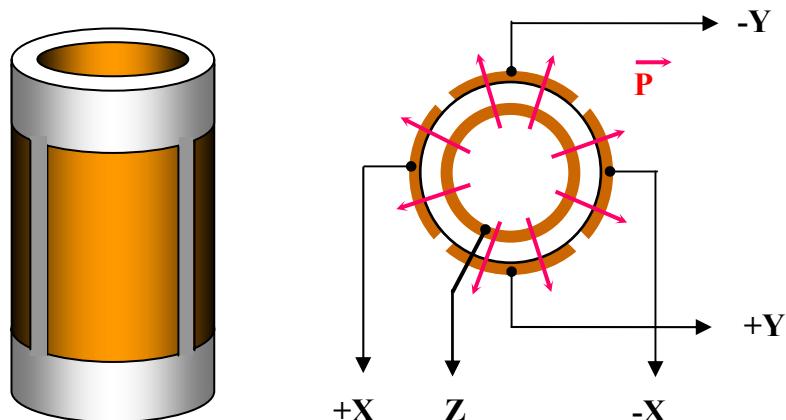

Fig. 5. Tubular piezo-scanner

The internal electrode is usually continuous. The external electrode is divided by cylinder generatrixes into four sections. When differential-mode voltage is applied on opposite sections of the external electrode (with respect to the internal electrode) part of the tube reduces in length (where the field direction coincides with the polarization direction), and increases (where field and polarization directions are opposite). This leads to a bend of the tube. Scanning in the X,Y plane is done in this manner. Change of the internal electrode potential with respect to all external sections results in lengthening or reduction of the tube along Z axis. Thus, it is possible to implement the three-coordinate scanner on the basis of one piezo-tube. Real scanning elements frequently have a more complex structure; however the working principle remain the same.

Scanners based on bimorph cells are also widely used. Bimorph is made of two plates of piezoelectric material, which have been glued together with opposite polarization vectors as shown in Fig. 6. If a voltage is applied to bimorph electrodes, as shown on Fig. 6, one of the plates will

extend, and the other one will be compressed, resulting in a bend of the whole element. In real constructions of bimorph elements the potential difference between the internal common electrode and external electrodes is created so that in one element the field coincides with the direction of a polarization vector, and in another element it is oppositely directed.
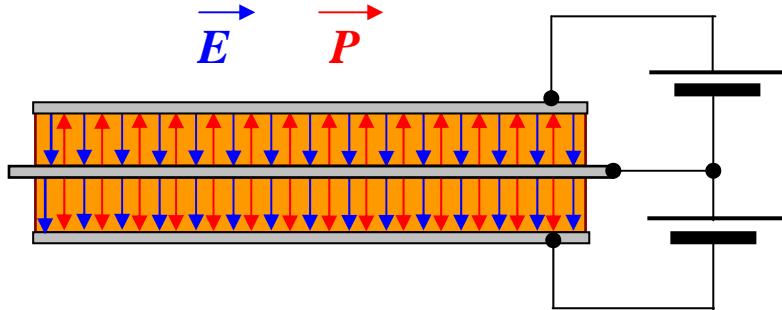

Fig. 6. Structure of a bimorph cell

The bimorph bending under the influence of electric fields is the working mechanism of bimorph piezo-scanners. Combining three bimorph elements in one device makes possible to implement a tripod (Fig. 7).
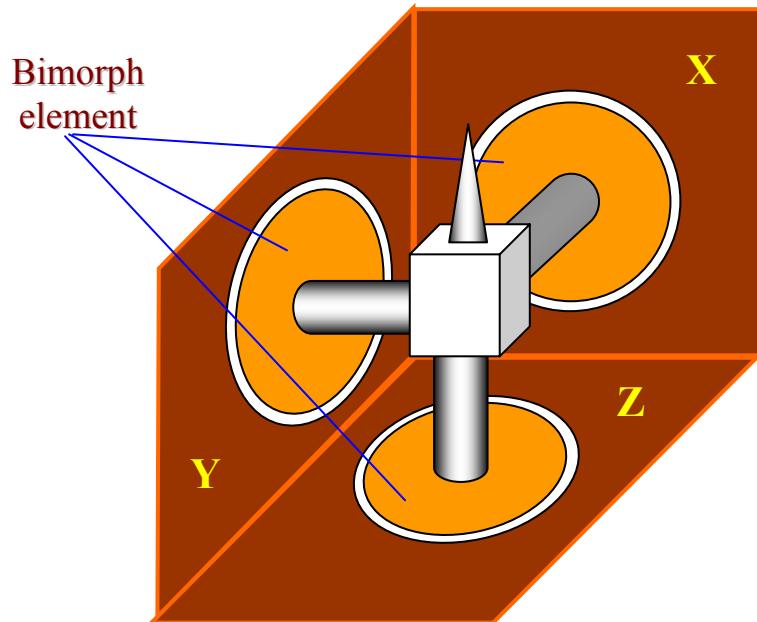

Fig. 7. Three-coordinate scanner made of three bimorph elements

If external electrodes of a bimorph element are divided into four sectors, then it is possible to move a stem (e.g. holding a tip) along the Z axis and in the X, Y plane using a single bimorph element (Fig. 8).
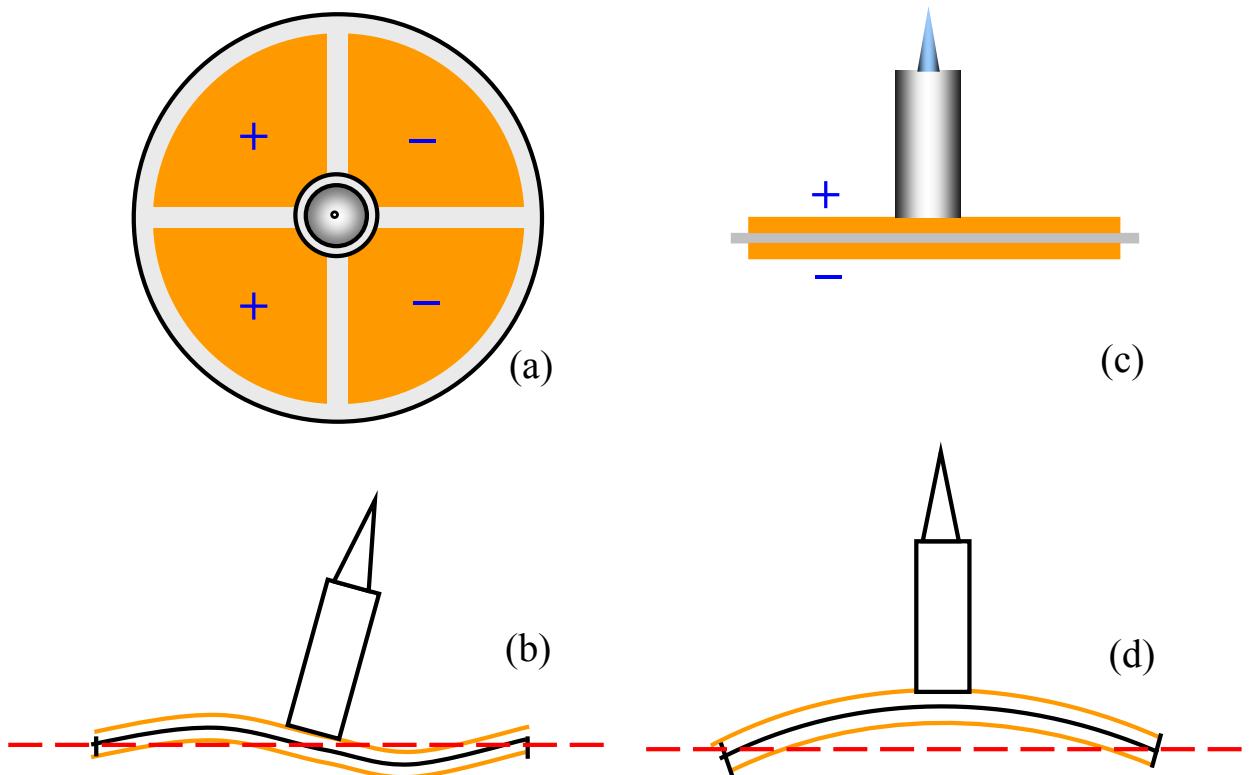
Fig. 8. Schematic representation of a bimorph piezo-scanner working mechanism

Indeed, applying a differential-mode voltage on opposite pairs of external electrodes sections makes bending the bimorph so that the tip will move in the X,Y plane (Fig. 8 (a, b)). On the other hand, a potential applied to the internal electrode with respect to all sections of external electrodes makes bending the bimorph, so that the tip moves in the Z axis direction (Fig. 8 (c, d)).

<u>Piezoceramics nonlinearity</u>

Despite of a number of technological advantages over crystals, piezoceramics have some drawbacks. One is the nonlinearity of piezoelectric properties. The dependence of the piezo-tube shift size in Z direction on the value of the applied field is schematically shown in Fig. 9 as an example. Generally (especially at large control fields) the piezoceramics are characterized by nonlinear dependence of the deformation on the field (i.e. on the control voltage). Thus, deformation of piezoceramics is a complex function of the applied electric field:

$$u_{ij} = u_{ij}(\vec{E}).$$

For small control fields the given dependence can be represented in the following way:

$$u_{ij} = d_{ijk} E_k + \alpha_{ijkl} E_k E_l + ...,$$

where d_{ijk} and α_{ijkl} are the first and second order piezoelectric coefficients, respectively.
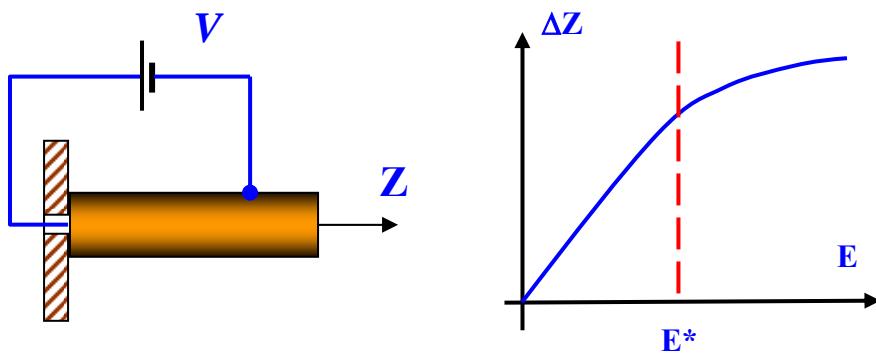
**Fig. 9. Schematic representation of dependence
of ceramics shift on the size of applied electric field**

Typical values of fields E*, at which nonlinear effects cannot be neglected, are about 100 V/mm. Therefore in scanning elements the control fields are usually kept small (within the linear range E<E*).

Piezoceramics creep

Another drawback of piezoceramics is the so-called *creep*, a delay in the response to sudden change of the control electric field value. Time diagrams of control fields change and corresponding shifts of the scanner along the Z axis and in the X,Y plane are schematically shown in Fig. 10.
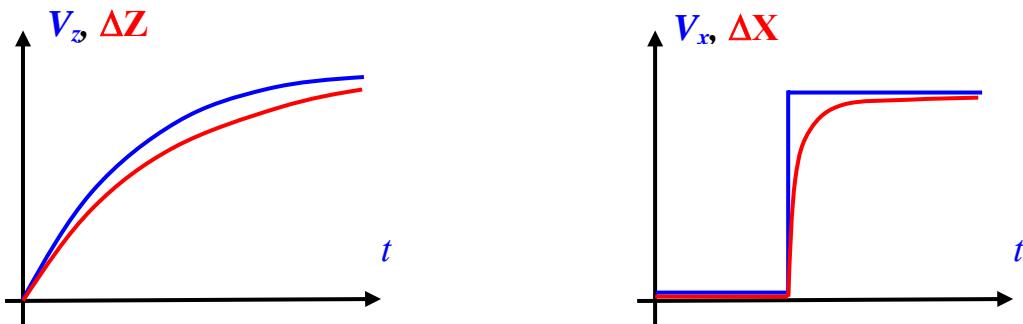
**Fig. 10. Schematic time diagrams of changes of the control voltages during scanning (blue lines),
and of the corresponding scanner shifts along Z and X axes (red lines)**

The creep results in appearance of geometrical distortions in SPM images. Specifically strong influence of the creep occurs, on initial stages of the scanning process, or after a large displacement of the starting point of the scanned area. Time delays are used to reduce the effect of creep, allowing to partially compensate the scanner delay.

Piezoceramics hysteresis

Another drawback of piezoceramics is the presence of hysteresis in the transfer function $\Delta Z = f(V)$, i.e. the piezoceramic deformation depends on the sign of previously applied electric field.
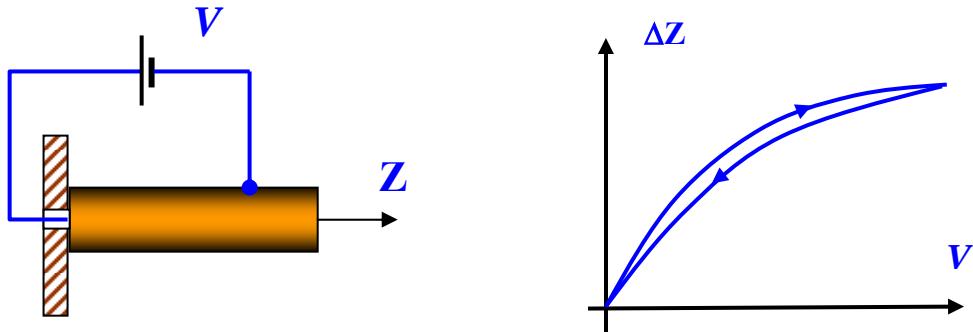

**Fig. 11. Dependence of the piezo-tube shift on the
value and direction of the applied voltage**

In other words the piezoceramic shift ΔZ describes, in the $(\Delta Z, V)$ plane, a looped trajectory where different ΔZ values are taken, depending on the time derivative of the control voltage V (Fig. 11). To avoid distortions in the SPM images caused by piezoceramics hysteresis, information is stored, in a sample scanning, only while tracing one of the loop branches $\Delta Z = f(V)$.

1.3. Devices for precise control of tip and sample positions

One of the important technical requirements in scanning probe microscopy is the precision of movements of tip and sample, aiming at an accurate selection of the sampled area. Several types of devices performing movements of objects with high accuracy are used to solve this problem. Various mechanical reducers, in which coarse movements are converted into fine movements, became widely spread. For example lever devices, in which the reduction of movement is produced by the different length of the lever arms, are widely applied. The lever reducer is schematically presented in Fig. 12.
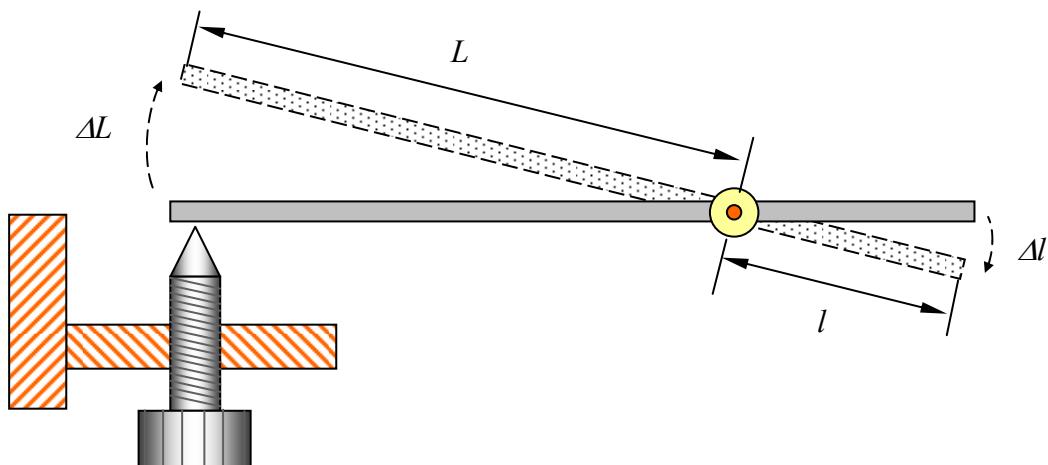

Fig. 12. Lever movement reducer schematic

The mechanical lever downscales the movement by the following factor:

$$R = \frac{\Delta L}{\Delta l} = \frac{L}{l} \ .$$

Thus, the larger is the ratio between the arm L to the arm l, the more precisely the process of tip to sample approach can be controlled.

Spring/cantilever reducers are also widely used in constructions of microscopes, in which the movements are scaled down exploiting the difference in stiffness of two elastic elements in series (Fig. 13). The structure usually consists of a rigid base, a spring and an elastic beam (cantilever). The elastic constant of the spring k and of the cantilever K are selected so that the condition $k < K$ is satisfied.
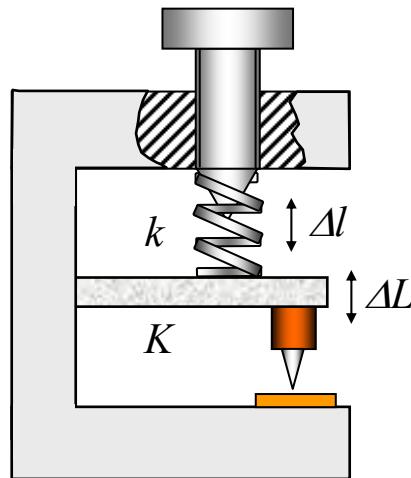

Fig. 13. Schematic of spring/cantilever movements reducer

From the equilibrium condition it follows, that

$$F_{elast} = k \cdot \Delta l = K \cdot \Delta L \ ,$$

where Δl and ΔL are the spring and cantilever displacements, respectively. In this case the reduction coefficient equals the ratio between the elastic constant of the elastic elements:

$$R = \frac{\Delta l}{\Delta L} = \frac{K}{k} \ .$$

Thus, the larger is the cantilever stiffness with respect to the spring stiffness, the more precisely it is possible to control the displacement of the cantilever end.

Stepping motors

Stepping motors (SM) are electromechanical actuators, which transform electric pulses into discrete mechanical movements (rotations). The important advantage of stepping motors is that they provide a reliable correspondence between the angular displacement of the rotor and the number of actuating current pulses. In SM the torque is created by magnetic coupling between the stator and

the rotor poles. The stator has several poles, made of high magnetic permeability material and assembled from separate plates to reduce the losses by eddy currents. The torque is proportional to the magnetic field value, which is proportional to the current and to the number of coils. If the current in one of the windings is switched on, the rotor takes a certain position. By switching off the current in that winding and switching it on in another one, it is possible to move the rotor to the next position, etc. Thus, controlling the current in windings, it is possible to rotate the SM rotor in a step-by-step mode. It will remain in the position set by the last switched on winding until the external applied torque does not exceed a threshold value called the holding torque. With higher applied torque the rotor will turn and try to take one of the following equilibrium positions.

The simplest structure of a stepping motor is schematically shown in Fig. 14. It consists of a stator with windings and a rotor with permanent magnets. The rotor poles have rectangular shape parallel to the motor axis. The motor shown in figure has 3 pairs of rotor poles and 2 pairs of stator poles. The stator has 2 independent windings, each one wound up on two opposite poles. The motor shown in Fig. 14 has an incremental step of 30 grad. When the current is switched on in one of the windings, the rotor tends to take the position at which the unlike poles of rotor and stator are opposite to each other. To produce the continuous rotation it is necessary to switch on the windings alternatively by applying a sequence of current pulses.
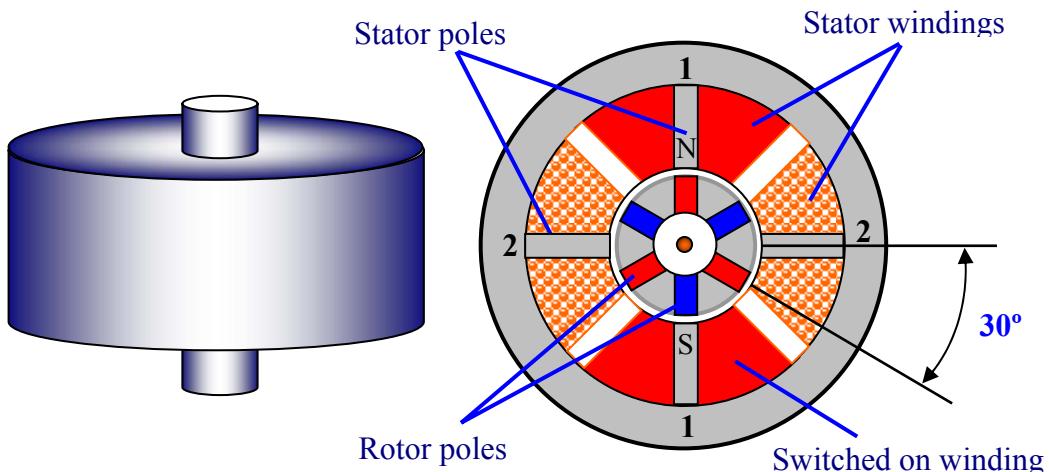

Fig. 14. Stepping motor with permanent magnet rotor

Stepping motors having more complex structure and providing from 100 to 400 steps per revolution (incremental step from 3.6 to 0.9 degrees) are used in practice. If such motor drives a threaded axis with a pitch of 1 mm, then an accuracy in object positioning better than 1 micron may be obtained. Additional mechanical reducers are applied to increase the accuracy. The possibility of electric control allows the use stepping motors in automated systems to approach a tip to a sample in scanning probe microscopes.

Step-by-step piezoelectric motors

Requirements of good insulation from external vibrations and necessity of working under vacuum impose serious restrictions on application of mechanical devices for tip and sample movements. In this respect, devices based on piezoelectric converters, allowing to perform remote control of objects movement, became widely used in probe microscopes.

One of the devices used for this purpose is the step-by-step inertial piezo-motor presented in Fig. 15. This device includes the base (1) on which the piezoelectric tube (2) is fixed. The tube has electrodes (3) on external and internal surfaces. The split spring (4) holds a cylinder with polished surface, massive enough (5) that supports the object to be moved. The moved object can be fixed to the cylinder with the help of a spring or a captive nut that allows the device to work at any orientation in space.


1. – base;
2. – piezoelectric tube;
3. – electrodes;
4. – split spring;
5. – cylindrical object holder
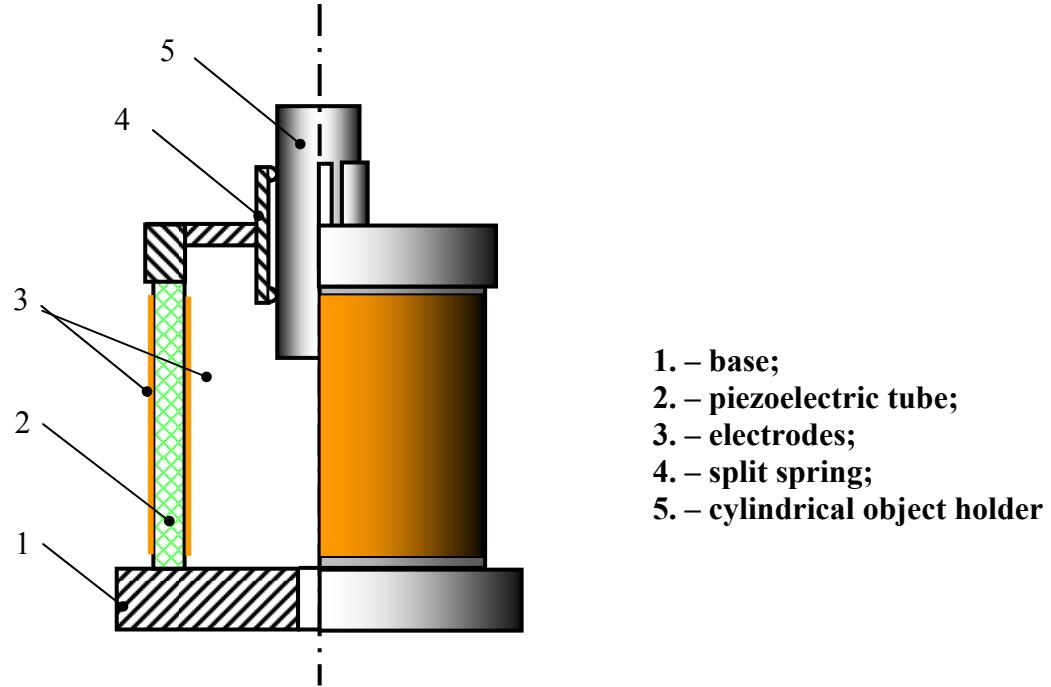
Fig. 15. – Step-by-step piezoelectric motor

The device works as follows. To move the object holder in the Z axis direction a saw tooth voltage signal is applied to electrodes of the piezo-tube. The characteristic form of a control voltage pulse is presented on Fig. 16.
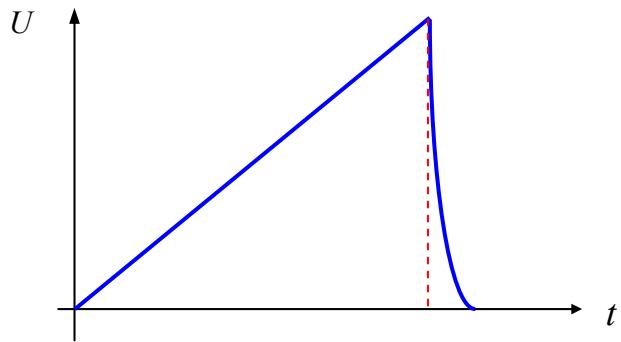
Fig. 16. Control voltage pulse form of a step-by-step inertial piezoelectric motor

The tube is smoothly extended or compressed (depending on the voltage polarity), and at the ramp end, the object holder is shifted of the following amount:

$$\Delta l = d_{31} \frac{l}{h} U \,.$$

At the end of the voltage ramp the tube returns suddenly to the starting position with an acceleration a, which has its maximal value in the beginning:

$$a = \Delta l \omega^2 ,$$

where ω is the resonant frequency of longitudinal oscillations of the tube. If the following condition is satisfied :

$$F_{fr} < ma$$

(m is the weight of the object holder, F_{fr} the friction force between the object holder and the split spring) then the object holder, due to its inertia, slides relatively to the split spring. As a result, the object holder makes a step $K\Delta l$ with respect to the starting position. The K factor depends on the cylinder weight and on the stiffness of the split spring. When the polarity of the control voltage pulses is reversed, the object movement direction changes. Thus, applying a saw tooth voltage of various polarities to the piezo-tube electrodes, it is possible to move the object in space and to approach the tip to the sample in a scanning probe microscope.

1.4. Protection of SPM against external influences

Protection against vibrations

Any scanning probe microscope is an oscillatory system with its own resonant frequencies ω_k. External mechanical vibrations with frequencies coinciding with ω_k, may excite resonance in the measuring heads structure, which results in fluctuations of the tip relatively to the sample that is perceived as a parasitic periodic noise deforming and dithering the SPM images of samples surface. To reduce the influence of external vibrations the measuring heads are made of massive metal details with high (more than 100 kHz) resonant frequencies. Scanners have low resonant frequencies. In the design of modern SPM it is necessary to reach a compromise between the scanner range (the size of maximum scanned area) and its resonant frequency. Typical values for resonant frequencies are in the range 10 - 100 kHz.

Various types of vibration-insulating systems can be distinguished as passive and active ones. The basic idea incorporated in passive vibration-insulating systems is the following. The amplitude of forced oscillations of a mechanical system quickly decays at large values of the difference between the excitation frequency and own resonant frequency of the system (see Fig. 17).
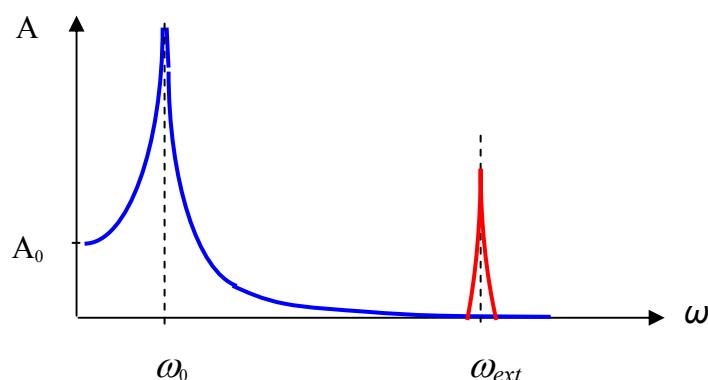
**Fig. 17. Blue color: SPM resonant curve
Red color : frequency spectrum of external vibrations**

Therefore external vibrations with frequencies $\omega_{ext} \gg \omega_0$ practically do not affect the oscillatory system. Hence, if the measuring head of a probe microscope is placed on a vibration-insulating platform or on an elastic suspension (Fig. 18), then only external fluctuations with frequencies close to the resonant frequency of the vibration-insulating system will be picked-up by the microscope. Since the resonant frequencies of SPM heads are in the range 10 - 100 kHz, choosing the resonant frequency of vibration-insulating systems low enough (about 5 - 10 Hz), it is possible to protect the device from external vibrations rather effectively. In order to quench oscillations even at their own resonant frequencies, dissipative elements with viscous friction are introduced into vibration-insulating systems.
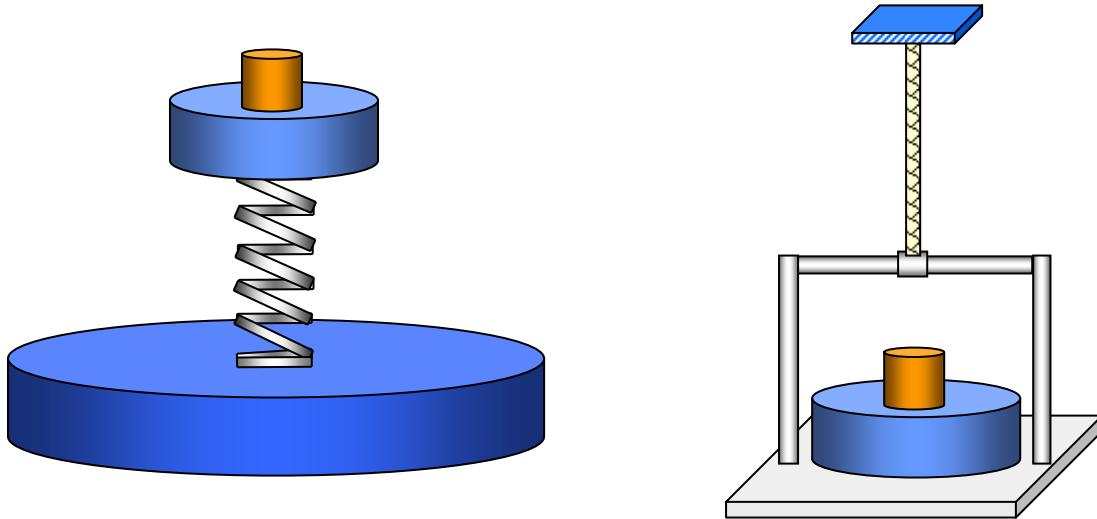

Fig. 18. Passive vibration- insulating systems

Thus, to reach effective protection it is necessary to make the resonant frequency of the vibration-insulating system as small as possible. However, it is difficult to realize in practice very low frequencies. For spring platforms and elastic suspensions the resonant frequency is

$$\omega_0 = \sqrt{\frac{k}{m}},$$

where k is the spring (or suspension) elastic constant, m the weight of the vibration-insulating platform together with the SPM head. We shall estimate parameters of the vibration-insulating system providing suppression of high-frequency vibrations. From the equilibrium condition it follows, that

$$mg = k\Delta l,$$

where Δl is the lengthening (or compression) of the elastic element, g is the gravitational acceleration. Then, for the size of lengthening:

$$\Delta l = \frac{gm}{k} = \frac{g}{\omega_p^2} = \frac{g}{(2\pi\nu)^2} \cong 0.25 \cdot \frac{1}{\nu^2}.$$

Thus, in order to obtain for the vibration-insulating system a resonant frequency smaller than 1 Hz, the lengthening (or compression) of the elastic element must be more than 25 cm. Such lengthening can be obtained in the simplest way using springs or rubber suspensions. Taking into account, that

the relative stretching of springs can reach 100 %, the length of the suspension elastic element may be 25 cm, and, hence, the total size of the vibration-isolating system will be 50 cm. If resonant frequency requirements are less stringent, it is possible a substantial reduction of the of the vibration-insulating system size. So, for a frequency cut-off of 10 Hz the compression should be only 2,5 mm. Such compression is may be easily obtained using a stack of metal plates with rubber spacers, which considerably reduces the dimensions of the system.

Active systems for suppression of external vibrations are also successfully used to protect the SPM heads. Such devices are electromechanical systems with a negative feedback, which stabilizes the vibration-insulating platform (Fig. 19).
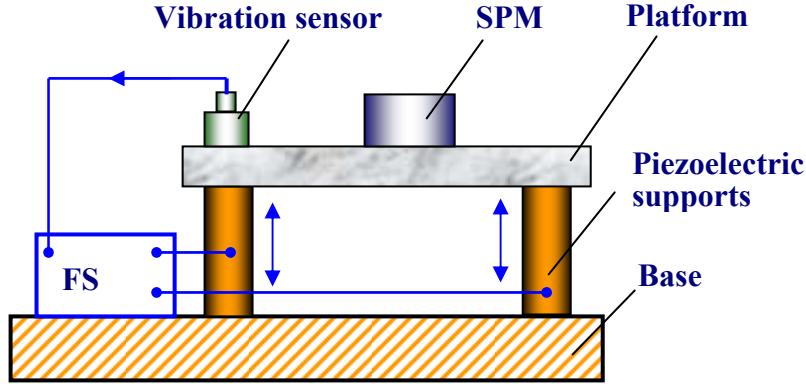

Fig. 19. Active vibration-insulating system schematic

The working principle of active systems is the following. The vibration sensor (accelerometer) installed on the platform produces a signal that is fed to the feedback system (FS) where it is inverted, amplified and transmitted to the piezoelectric actuators, placed under the platform legs, canceling the platform acceleration. This is the so-called proportional adjustment. In fact, let the platform oscillate with the frequency $\rceil$ under the action of external force, with amplitude u:

$$u = u_0\, sin(\,\omega t\,).$$

Then the platform acceleration is

$$\ddot{u} = -\omega^2 u_0\, sin(\,\omega t\,).$$

The feedback system provides an antiphase signal $u_f = -a\, sin(\,\omega t\,)$ to the supports; therefore the platform displacement is due the superposition of two excitations:

$$u = u_0 = (\,u_0 - a\,)\,sin(\,\omega t\,).$$

The feedback system will adjust the amplitude of the signal fed to the actuators until the platform acceleration reaches zero:

$$\ddot{u} = -\omega^2 (\,u_0 - a\,)\,sin(\,\omega t\,).$$

Multistage constructions of vibration-insulating systems of various types are commonly used, allowing to increase the degree of protection of devices against external vibrations.

Protection against acoustic noise

Another source of vibrations in the probe microscopes structure are acoustic noises of various nature.
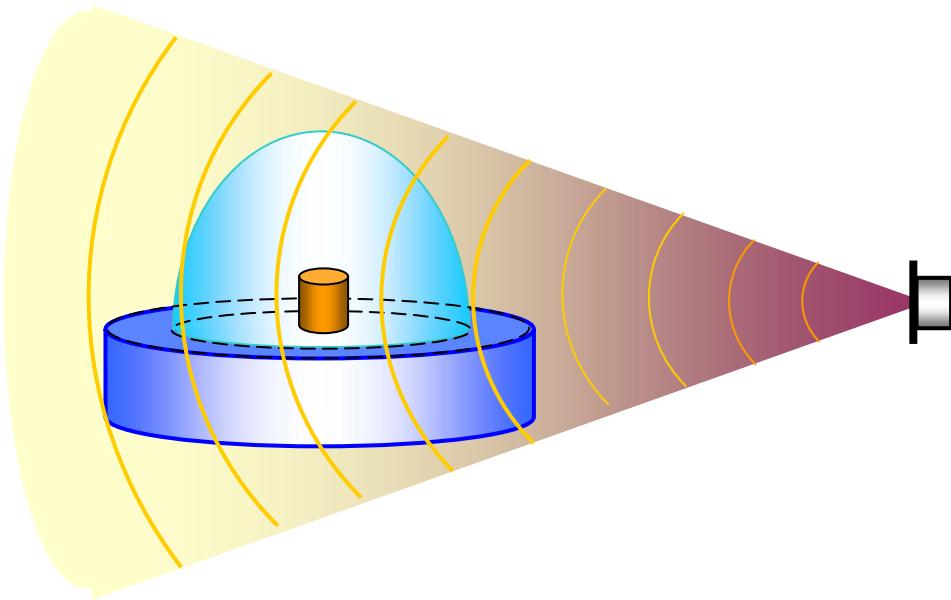

Fig. 20. SPM protection against acoustic noise

Acoustic waves directly affect elements of SPM heads, resulting in oscillations of the tip with respect to the sample surface. Various protective enclosures, allowing a sensible reduction of the level of acoustic noise are used to protect the SPM. The most effective protection against acoustic noise is to place the measuring head into a vacuum chamber.

Reduction of the thermal drift of the tip position above the surface

One of important problems in the SPM is the stabilization of the tip position above the sample surface. The main source of tip instability is the change of the room temperature or the warming up of SPM elements during operation. Temperature change of a body results in thermo elastic deformations:

$$u_{ik} = \alpha_{ik} \Delta T,$$

where u_{ik} is the deformations tensor, α_{ik} are the components of thermal expansion tensor, ΔT is the temperature increment. For isotropic materials the thermal expansion coefficient is a scalar:

$$\alpha_{ik} = \alpha \cdot \delta_{ik},$$

where δ_{ik} is the ordinary Kronecker tensor, α is the thermal expansion coefficient. Absolute lengthening of microscope construction elements can be estimated from the following equations:

$$u = \frac{\Delta l}{l_0} = \alpha \cdot \Delta T; \qquad \Delta l = l_0 \alpha \cdot \Delta T.$$

Typical values of expansion coefficients are in the rang $10^{-5} - 10^{-6}$ K^{-1}. Thus, heating a 10 cm long body by 1°C its length increases on about 1 micron. Such deformations affect substantially the SPM performance. To reduce the thermal drift, thermoregulation of SPM heads is used, or temperature-compensating elements are introduced in the head structure. The idea of temperature-compensation consists in the following. Any SPM model can be schematized as a set of elements with different thermal expansion coefficients (Fig. 21 (a)).


(a)   **(b)**
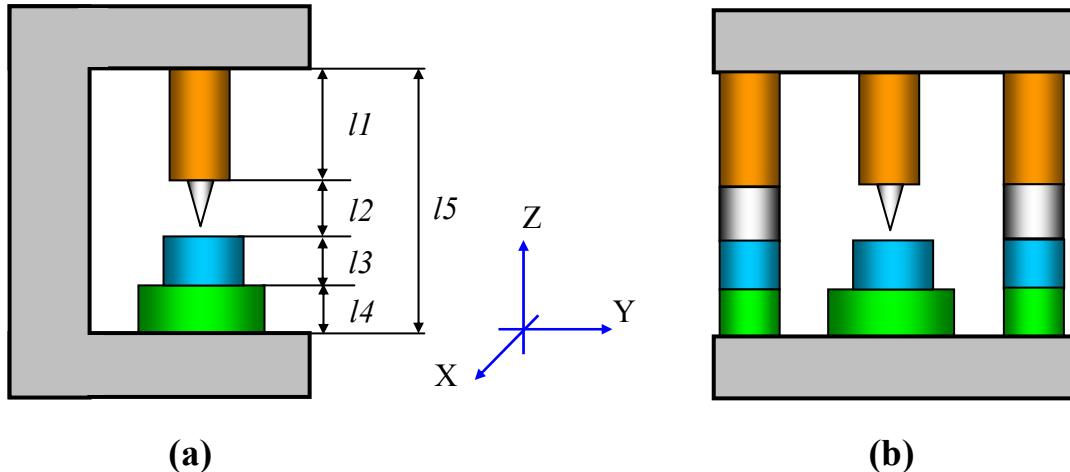
Fig. 21. Compensation of thermal expansions in SPM

In order to reduce the thermal drift in the SPM measuring heads, compensating elements with different expansion coefficients are introduced, in a geometry that brings to zero the sum of temperature expansions in various parts of the structure:

$$\Delta L = \sum_i \Delta l_i = \Delta T \sum_i \alpha_i l_i \Rightarrow 0 \,.$$

The simplest way to reduce the thermal drifts is to introduce in the SPM construction compensating elements made of the same material and with the same characteristic sizes, as the basic elements of the SPM head (Fig. 21 (b)). When the temperature of such arrangement changes, the shift of the tip in Z direction is minimal. The measuring head of microscopes are axial-symmetric designed to stabilize the position of the tip in the X, Y plane.

1.5. Acquisition and processing of SPM images

Scanning a surface in a SPM is like moving an electronic beam on the screen in the cathode ray tube of a TV. The tip goes along a (row) first in forward, and then in the reverse direction (horizontal scanning), then passes to the next line (frame scanning). Movement of the tip is done in small steps by the scanner that is driven by a saw tooth voltage produced by digital-to-analog converters. The surface topographic information is stored, as a rule, during the forward pass.
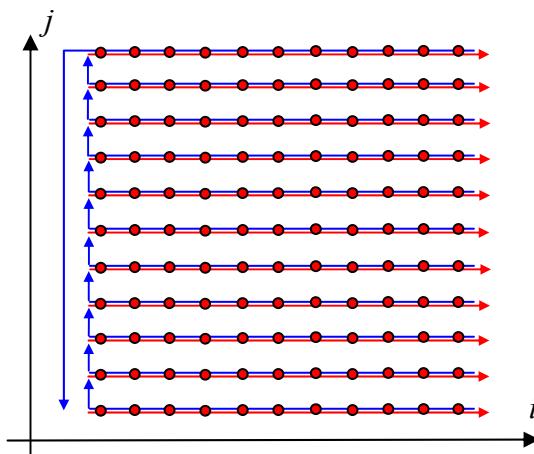
Fig. 22. Schematic illustration of the scanning process.
The direction of the forward motion of the scanner is indicated by red arrows
Reverse motion of the scanner is indicated by dark blue arrows
Registration of the information is made in points on direct pass

The information collected by the scanning probe microscope, is stored as a two-dimensional file of integer numbers a_{ij} (matrix). The physical meaning of these numbers is determined by the kind of interaction, which was measured during scanning. To each value of *ij* pair of indexes corresponds a certain point of a surface within the scanning area. Coordinates of points of the sampled area are calculated simply multiplying the corresponding index by the value of the distance between points:

$$x_i = x_0 \cdot i, \qquad y_j = y_0 \cdot j.$$

Here x_0 and y_0 are the distances between adjacent points, along X and Y axes, where the information was recorded. As a rule, the SPM frames are square matrixes (whose size is commonly 256×256 or 512×512 elements). Visualization of the SPM frame is done by computer graphics, basically, as three-dimensional (3D) or two-dimensional brightness (2D) images. At 3D visualization the image of a surface $Z = f(x,y)$, is plotted in an axonometric view by pixels or lines. In addition to this, various ways of pixels brightening corresponding to various height of the surface topography are used. The most effective way of 3D images coloring is obtained simulating the surface illumination by a point source located in some point of space above the surface (Fig. 23). Thus it is possible to emphasize small-scale topography inequalities. Same graphical instruments and computer processing are used for scaling and rotation of 3D SPM images. In 2D visualization (also named ″Top View″ image) to each point of the surface $Z = f(x,y)$ is assigned a color (or a brightness) that corresponds to its z-value according to a given color-scale (or gray-scale). As an example, the 2D image of a surface area is presented on Fig. 24.
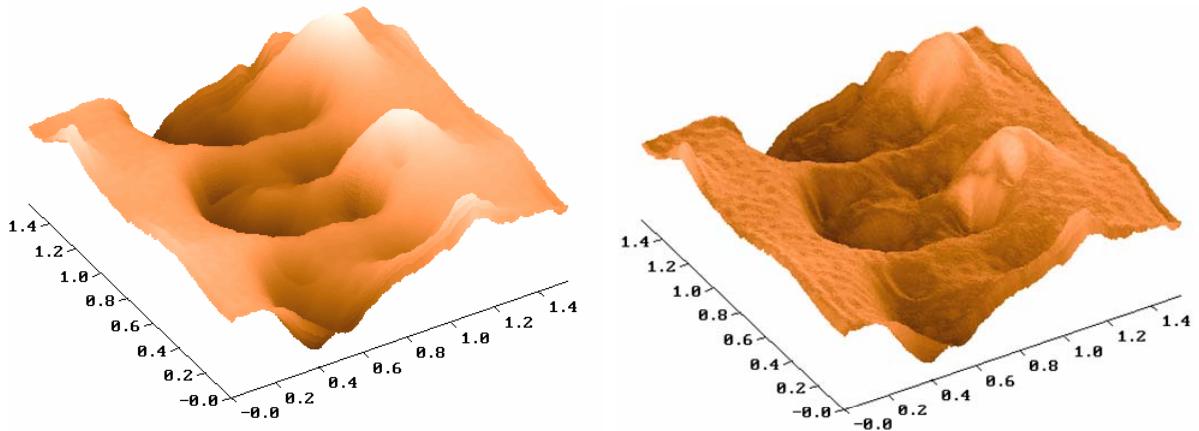
**Fig. 23. 3D visualization of a surface topography with illumination on height (a)
and with lateral illumination (b)**
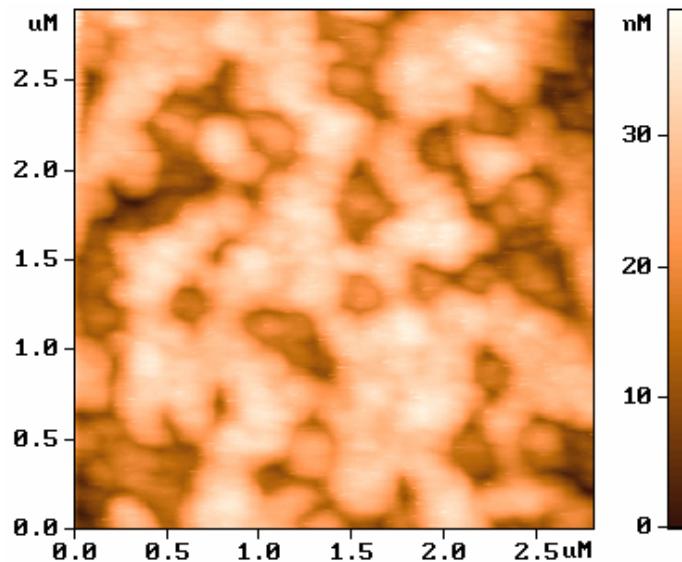
Fig. 24. 2D brightness image of a surface topography

The physical meaning of SPM images depend on the parameter that is used in the feedback loop. For example, the values stored in the $Z = f(x,y)$ matrix may depend on the electric current value flowing through the tip-surface contact with constant applied voltage, or they may depend on the main tip-surface interactive force (electric, magnetic, etc.). Besides these "maps" of the tip-sample interaction over the scanned area, a different type of information may be retrieved using SPM. For example, on a single point of the sample surface we may collect the dependence of the tunneling current on the applied voltage, the dependence of the interactive force on the tip-sample distance, etc. This information is stored as vector files or as matrixes of 2×N dimension, that may be displayed or printed using a set of standard tools for graphic presentation provided by the SPM software. SPM images, alongside with the helpful information, contain also a lot of secondary information affecting the data and appearing as image distortions. Possible distortions in SPM images caused by imperfection of the equipment and by external parasitic influences are schematically presented on Fig. 25.
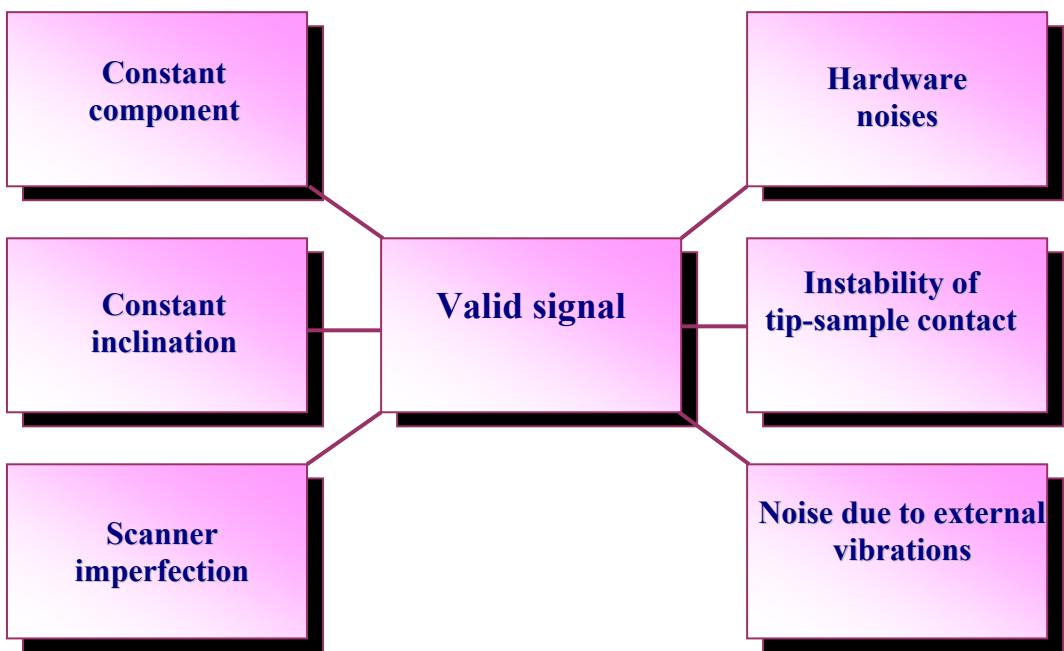
Fig. 25. Possible distortions in the SPM images

Subtraction of a constant component

As a rule, the SPM images contain a constant component, which does not bear useful information about the surface topography, but reflects the accuracy of sample approaching into the center of the dynamic range of scanner movement along the Z axis. The constant component is removed from the SPM frame using software tools so the new values of the topography heights in the frame are equal to

$$Z'_{ij} = Z_{ij} - \overline{Z}, \qquad \text{where } \overline{Z} = \frac{1}{N^2}\sum_{ij} Z_{ij}.$$

Subtraction of a constant inclination

Surface images acquired using probe microscopes, as a rule, show inclination. It can be due to several reasons. First, the inclination may appear as a result of a tilted installation of the sample onto the scanner or due to non-flatness of the sample; second, it might be connected with a temperature drift, which results in tip shifting with respect to the sample; third, it might be due to a non-linearity of the piezo-scanner movement. Inclined images take a large portion of Z-axis, so that the small image details become not visible. To eliminate this inconvenience, a subtraction of the constant inclination is usually performed. For this purpose at the first stage the method of least squares is used to find an approximating plane $P^{(1)}(x,y)$, which has minimal deviations from the surface topography $Z = f(x,y)$ (Fig. 26). Then the best-fit plane is subtracted from the SPM image. It is reasonable to subtract in various ways, depending on the inclination nature. If the inclination in the SPM image is caused by sample tilt relative to the tip axis, we may rotate the plane by an angle corresponding to the angle between the axis $\vec{n}$ orthogonal to the best-fit plane and the Z axis; thus the coordinates of the surface $Z = f(x,y)$ will be transformed according to such rotation. However, this transformation may give a multiple-valued function $Z = f(x,y)$. If the inclination is caused by a

thermal drift, the procedure of inclination subtraction affects only the Z-coordinates of the SPM image:

$$Z'_{ij} = Z_{ij} - P_{ij}^{(1)}.$$

This allows to keep correct geometrical relations in the X,Y plane between objects in the SPM image.
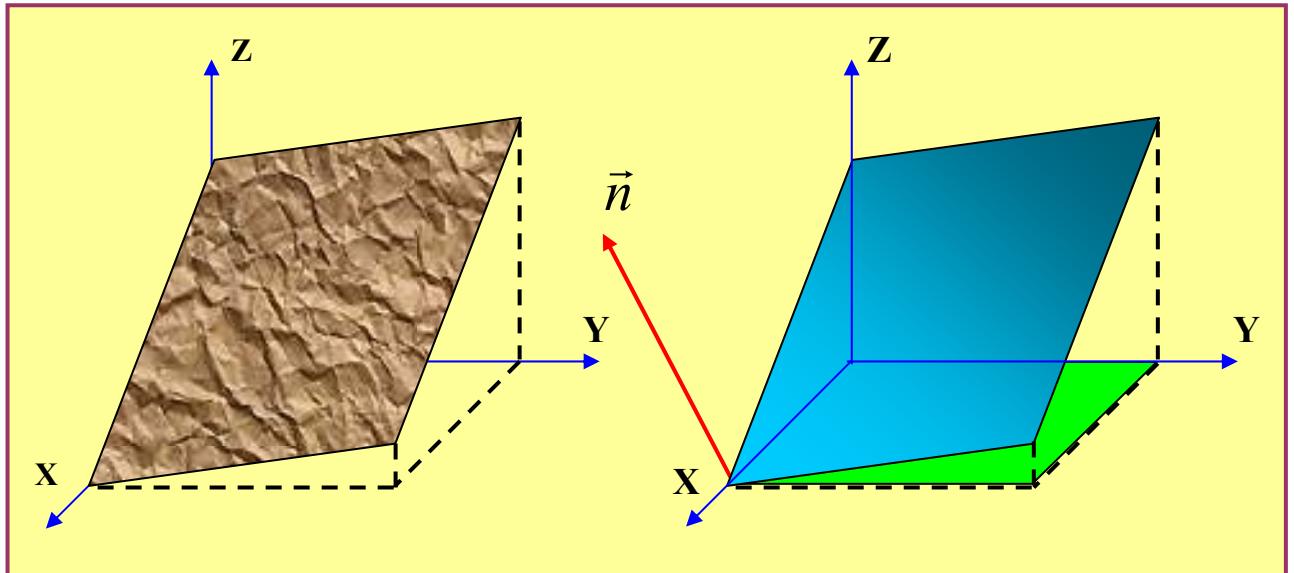

Fig. 26. Inclined plane interpolating the SPM image

Finally, an array with a smaller range of Z-values is obtained, and fine details of the image will be displayed with much larger contrast, becoming more visible.

The result of plane subtraction from a real AFM image is presented on Fig. 27.
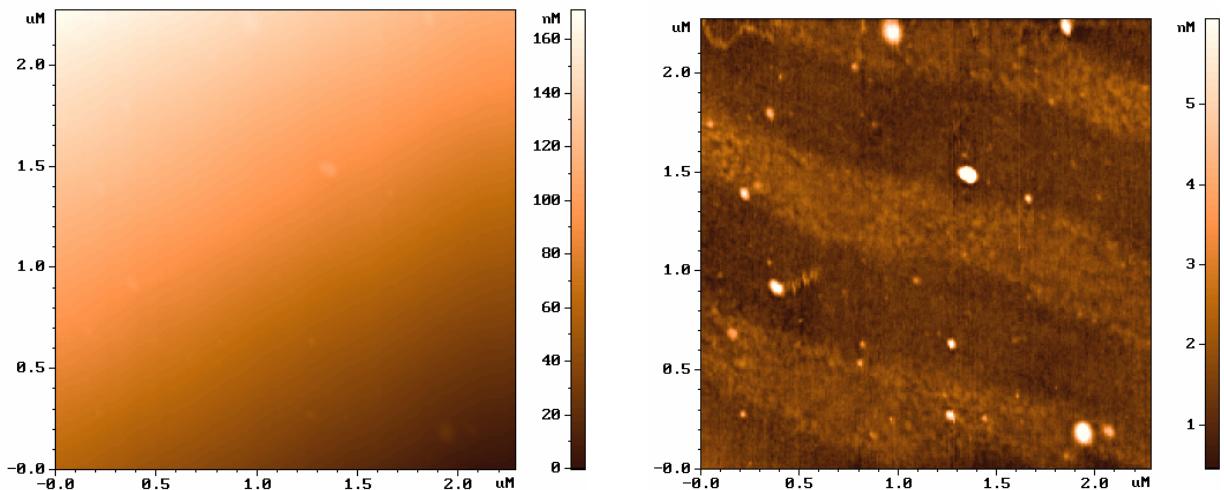

Fig. 27. Subtraction of an inclined plane from AFM image

Elimination of the distortions due to scanner imperfection

Imperfection of the piezo-scanner properties leads to artifacts in the SPM image. The scanner imperfections, such as hysteresis (differences in direct and reverse motions), creep and nonlinearity may be partially compensated by the hardware and by selection of optimum modes of scanning. In any case the SPM images contain residual distortions, which are difficult to remove on the hardware level. In particular, since the scanner movement in X and Y directions affects the tip – sample distance (z-axis), the SPM images represent a superposition of the actual topography and some surface of the second (and sometimes higher) order (Fig. 28).
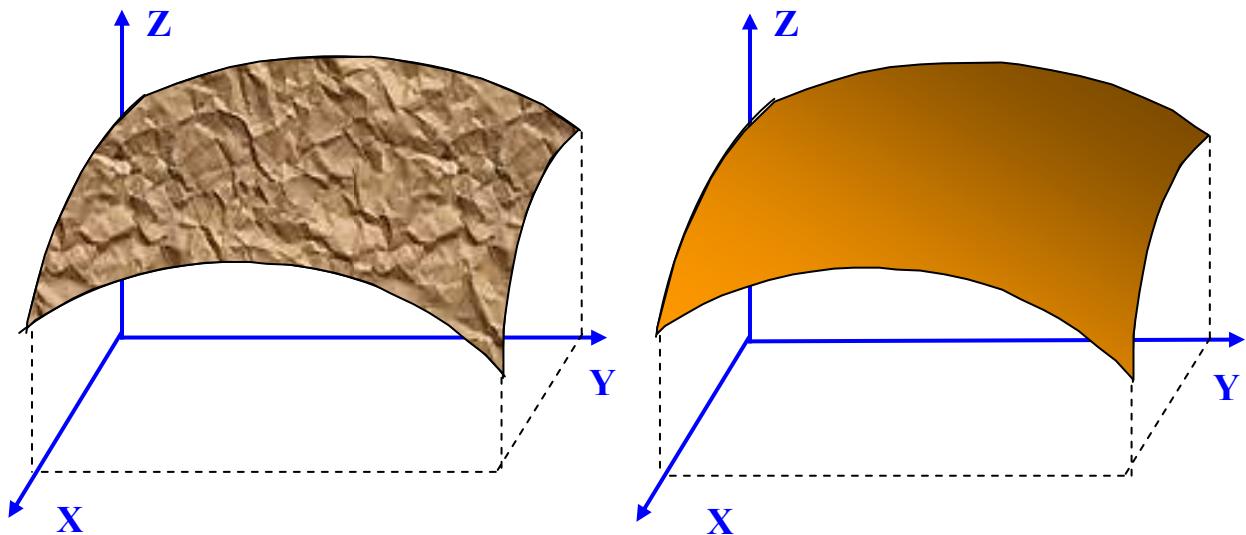
Fig. 28. Subtraction of a surface of the second order from the SPM image

The approximating surface of the second order $P^{(2)}(x,y)$ is calculated using the least-squares method, The fitting surface (with minimal deviations from the topographic surface $Z = f(x,y)$, is then subtracted from the original SPM image:

$$Z'_{ij} = Z_{ij} - P^{(2)}_{ij} .$$

The result of subtraction of the second order surface from the real AFM image is presented in Fig. 29.
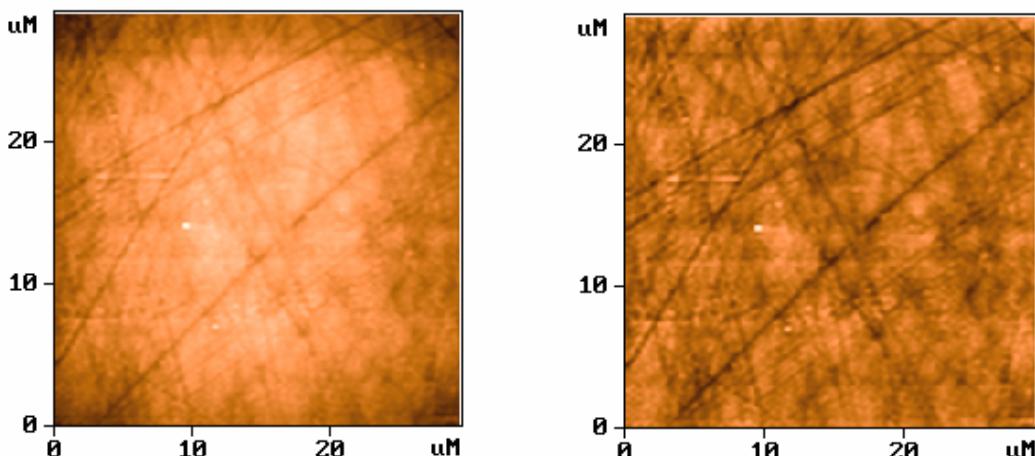
Fig. 29. Subtraction of the 2nd order surface from AFM image

Another type of distortions is due to non-linearity and non-orthogonality of the scanner movements in X, Y plane. This results in distortion of geometrical proportions in various parts of the SPM image. These distortions may be reduced using a correction procedure, with the help of correction coefficients, which are obtained by scanning test structures with a well-known topography.

Filtering of SPM images

Hardware noises, instabilities of the tip-sample contact during scanning, external acoustic noises and vibrations lead to SPM images affected by noise component. Partially the SPM image noises can be removed using software tools with help of filters of different types.

Median filtering

Median filtering provides good results during removal of a high-frequency random noise in SPM images. This is a nonlinear method of image processing, which main point can be explained as follows. The working window of the filter is selected, consisting of $n \times n$ points (as an example we take a 3×3 window, i.e. 9 points (Fig. 30)).

During filtering this window moves on the frame from point to point, and the following procedure is performed. Values of the SPM image amplitude in points within the window are lined up in ascending order, and the value in the center of the sorted line is moved to the window central point. Then the window is shifted to the next point, and the sorting procedure is repeated. Thus, major random peaks and dips during such sorting always appear at the ends of the sorted file and do not affect the final (filtered) image.


(a)

(b)

(c)
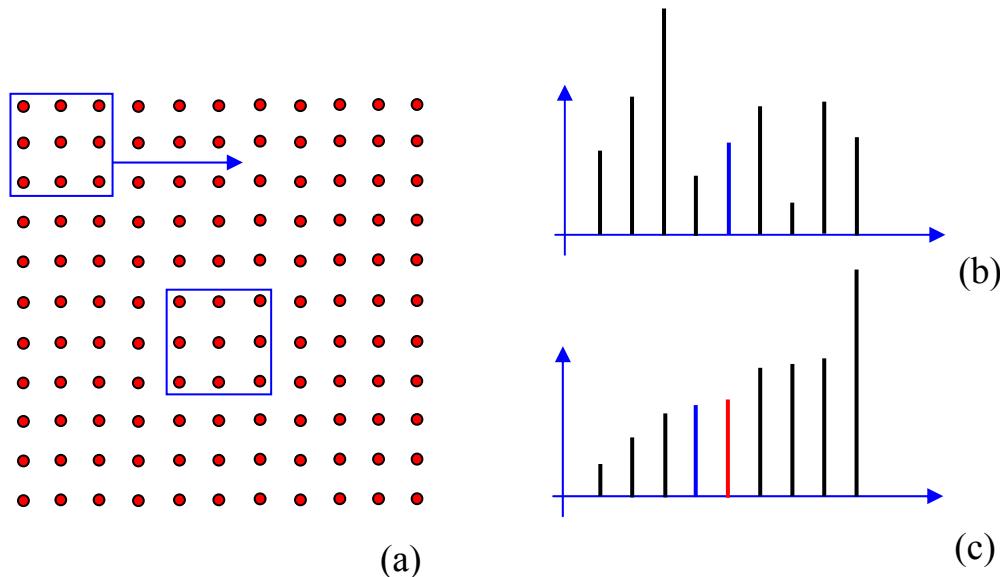
Fig. 30. Working principle of the median filter with a 3x3 window
(a) – displacement of a window during array filtering;
(b) –arrangement of elements in unsorted array
(central element marked in dark blue color);
(c) - arrangement of elements in the sorted array
(new central element marked with red color).

We shall notice that during such processing on the frame borders there are unfiltered areas which are discarded in the final image. The result of median filtering of a real AFM image is presented on Fig. 31.
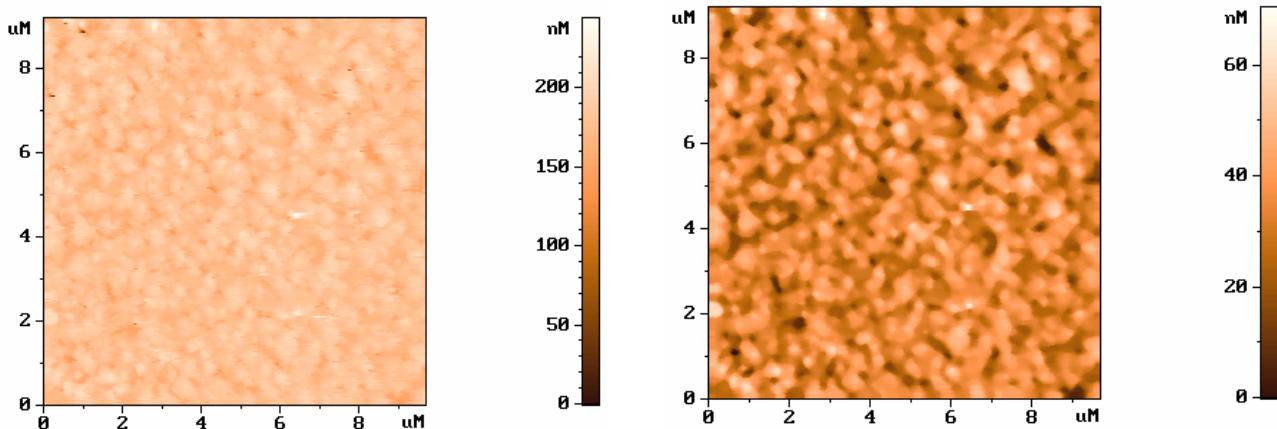

Fig. 31. Results of a 5x5 window median filter on AFM image

Line averaging

In the process of SPM scanning the frequency of data acquisition on each line strongly differs (at least, of two orders of magnitude) from the frequency of data acquisition of lines. As a consequence the high-frequency noise is contained basically in lines of the SPM image, while low-frequency noise affects the mean position of each line with respect to the adjacent lines. Moreover, the tip-sample distance changes frequently during scanning, due to micro movements in elements of the head structure, or due to changes in the tip working part (for example, capture by the tip apex of a micro particle from the surface, etc.). This produces steps parallel to the direction of scanning on the SPM image. These steps are caused by the displacement of one part of the SPM frame relative to another (Fig. 32 (a)). It is possible to get rid of such defects in SPM images using a line-by-line average procedure. The average topography value in each line is:

$$\overline{Z}_j = \frac{1}{N}\sum_i Z_{ij} \, .$$

And then the corresponding average values are subtracted from all values in each line:

$$Z'_{ij} = Z_{ij} - \overline{Z}_j \, ,$$

so that in every line of the new image the average value is equal to zero. This leads to removal of the steps produced by sharp changes of the average value in lines. An example of the effects of a line average in a real AFM image is presented in Fig. 32.
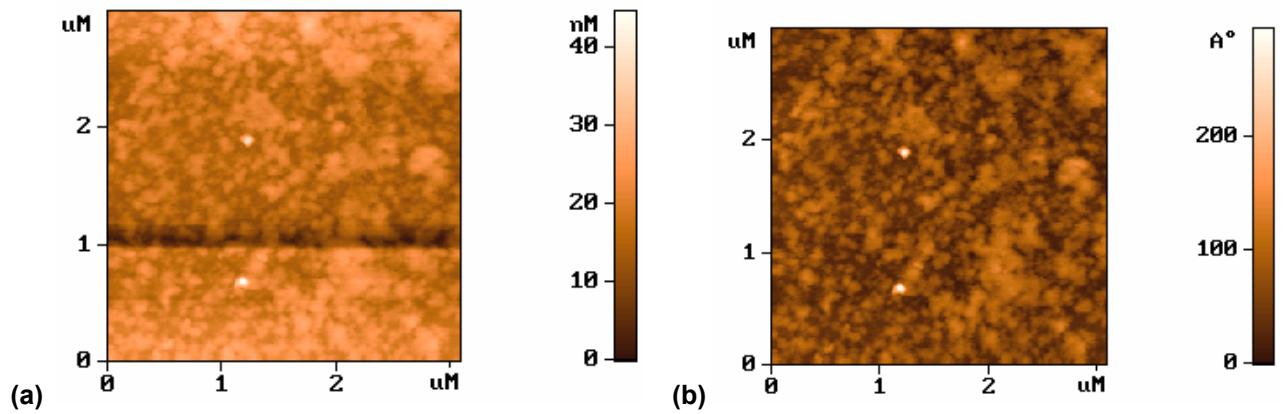
Fig. 32. Example of line-filtering
(a) — before line averaging; (b) — after line averaging.

Fourier filtration of the SPM images

The spectral filtration based on the Fourier transform is a powerful method for SPM images correction. Any function can be presented as a Fourier integral. In case of the SPM topographic function $Z=f(x,y)$ the Fourier transform is made by discrete values. Fourier image of the surface can be found using the following formulae (the imaginary unit $\sqrt{-1}$ is designated by v):

$$F_{\alpha\beta} = \frac{1}{N^2}\sum_{ij} Z_{ij}\, exp\left[2\pi v(\frac{\alpha \cdot i}{N} + \frac{\beta \cdot j}{N}) \right].$$

Accordingly, the inverse Fourier transform:

$$Z_{ij} = \sum_{\alpha\beta} F_{\alpha\beta}\, exp\left[-2\pi v(\frac{\alpha \cdot i}{N} + \frac{\beta \cdot j}{N}) \right].$$

The Fourier-filtration consists in applying a filter to the spatial frequency spectrum of the SPM image:

$$F'_{\alpha\beta} = F_{\alpha\beta} \cdot H_{\alpha\beta},$$

where $H_{\alpha\beta}$ represents the spectral function of the applied filter. Then the filtered image is obtained as a result of the inverse Fourier transform of the processed spectrum $F_{\alpha\beta} \cdot H_{\alpha\beta}$:

$$Z'_{ij} = \sum_{\alpha\beta} F_{\alpha\beta} \cdot H_{\alpha\beta}\, exp\left[-2\pi v(\frac{\alpha \cdot i}{N} + \frac{\beta \cdot j}{N}) \right].$$

The filters for low and high frequencies with circular and square windows are most commonly used. For low frequencies filters the spectral functions are defined as:

$$H_{\alpha\beta}^{cir} = \begin{cases} 1 \ for \ \sqrt{\alpha^2 + \beta^2} \le R \\ 0 \ for \ \sqrt{\alpha^2 + \beta^2} > R \end{cases}, \qquad H_{\alpha\beta}^{sqr} = \begin{cases} 1 \ for \ |\alpha| \le A \ ; \ |\beta| \le A \\ 0 \ for \ |\alpha| > A \ ; \ |\beta| > A \end{cases},$$

where R and A values are the radius of a circular window and the size of a square window of the filter function, respectively. By analogy, the high frequencies filters are:

$$H_{\alpha\beta}^{cir} = \begin{cases} 0 \ for \ \sqrt{\alpha^2 + \beta^2} \le R \\ 1 \ for \ \sqrt{\alpha^2 + \beta^2} > R \end{cases}, \qquad H_{\alpha\beta}^{sqr} = \begin{cases} 0 \ for \ |\alpha| \le A \ ; \ |\beta| \le A \\ 1 \ for \ |\alpha| > A \ ; \ |\beta| > A \end{cases}.$$

Results of the Fourier- filtration of one AFM image are shown in Fig. 33.

(a)   (c)

(b)   (d)
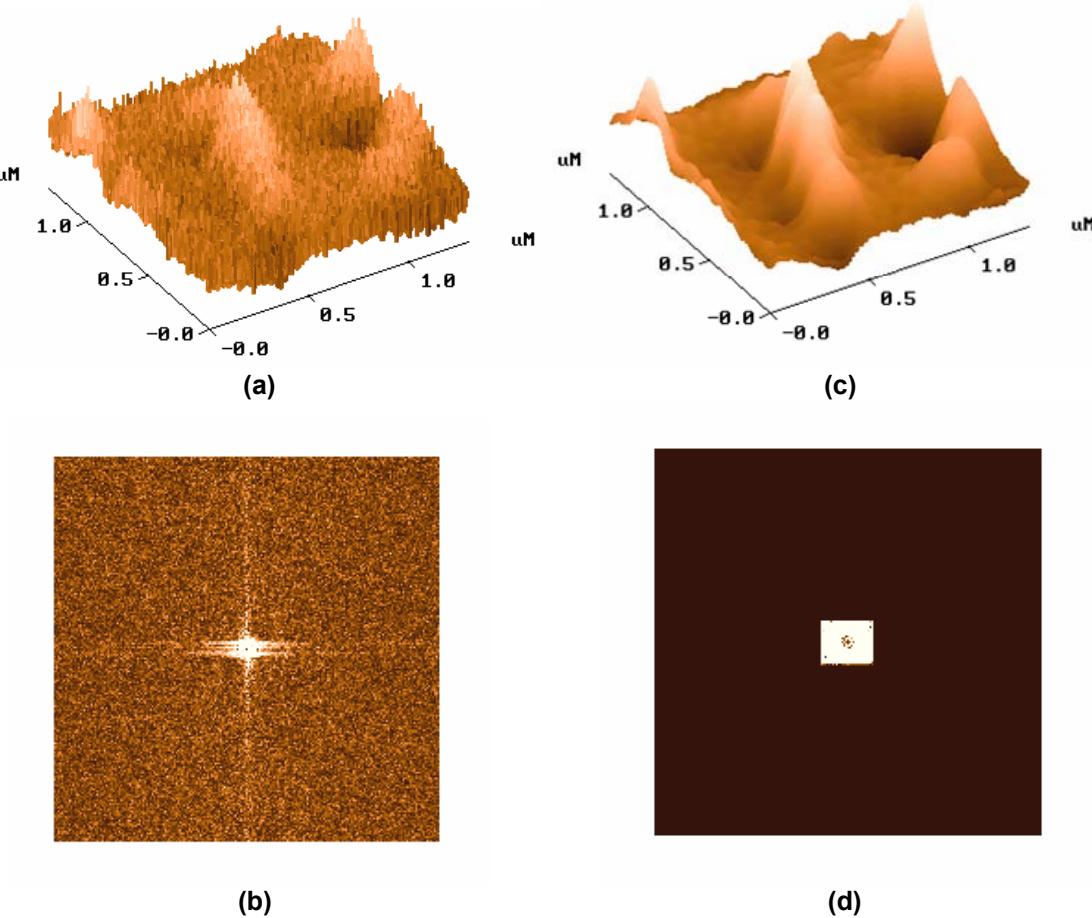
Fig. 33. Example of application of Fourier-filtration to one AFM image:
(a) – initial AFM image; (b) – spectrum of the initial image
(c) – filtered image; (d) – processing of spectrum by square low frequency filter

Filters with more complex spectral function are applied for elimination of undesirable effects due to the abrupt change of spectral function at the filter edge and on the frame borders. It is possible to calculate on the Fourier-image several useful characteristics of the surface. In particular, the power spectral density is:

$$S_{\alpha\beta} = \left| F_{\alpha\beta} \right|^2 = F_{\alpha\beta} F_{\alpha\beta}^* .$$

And the autocorrelation function is:

$$C_{ij} = \sum_{\alpha\beta} F_{\alpha\beta} F_{\alpha\beta}^* \, exp\left[2\pi v(\frac{\alpha \cdot i}{N} + \frac{\beta \cdot j}{N}) \right].$$

The standard SPM software includes a wide set of tools for image visualization and processing. Moreover, SPM images that can be stored in one of the graphic formats that allow using the additional opportunities given by the modern computer software for images processing and correction.

Surface restoration using a known tip shape

One of the drawbacks inherent to all modes of the scanning probe microscopy is the finite size of the tip apex. It leads to essential deterioration of the spatial resolution and to significant distortions in SPM images during scanning of surfaces with large aspect ratio irregularities. The aspect ratio is the ratio between the vertical and the horizontal typical sizes (of a relief or of a tip).

The acquired SPM image is a ″convolution″ of a tip and a surface. One-dimensional case of the "convolution" process is illustrated in Fig. 34.
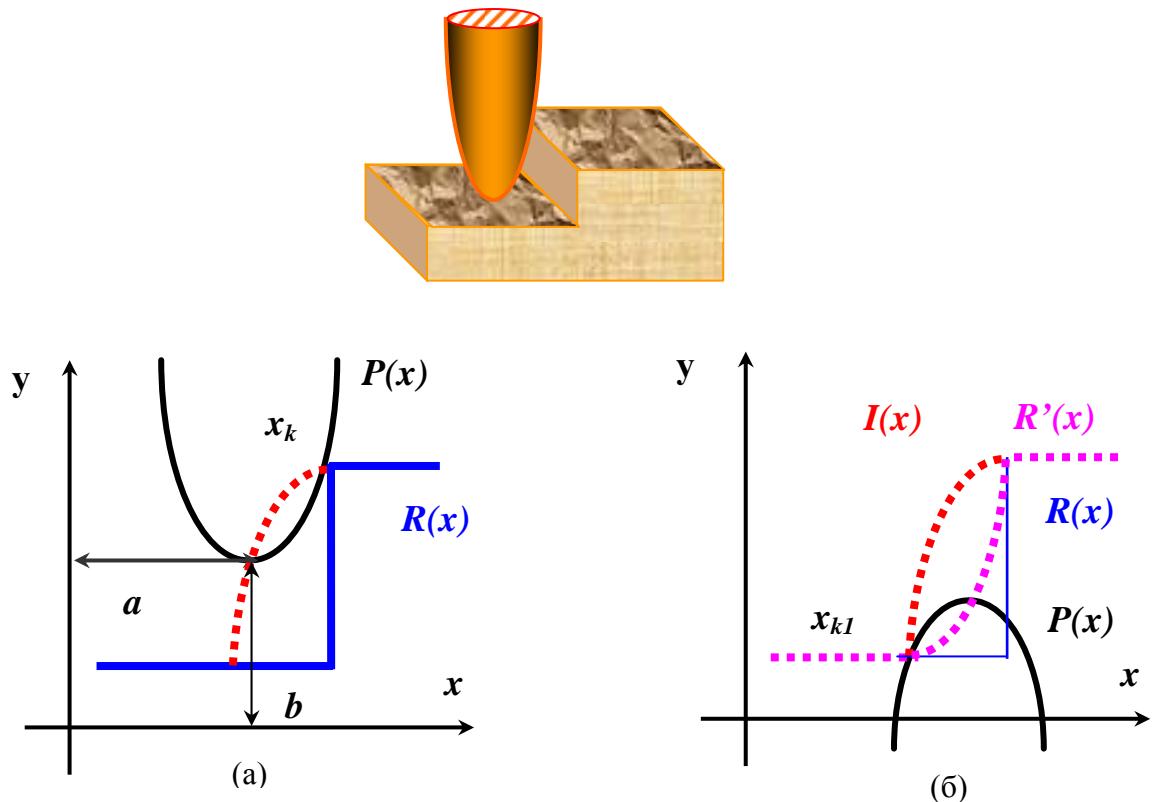

Fig. 34. Schematic drawing of an image acquisition process and restoration
(a): sample surface *R(x)* and initial image *I(x)*
(b) : partially restored image *R'(x)*, accounting for the tip form *P(x)*

The recently developed modes of restoration of the SPM images based on computer processing of the SPM data accounting the specific form of the tip allow only a partial solution of the problem [17,18]. The most effective mode of restoration is the numerical deconvolution [18], using the tip image obtained experimentally by scanning test structures with a well-known topography. We shall illustrate the procedure with a one-dimensional example. If the tip shape is described by the function $P(x)$, and the surface topography is described by the function $R(x)$, then the SPM image $I(x)$ is given by the following relation:

$$I(a) = R(x_k) - P(x_k-a),$$ under condition that $dR/dx = dP/dx$ in x_k points of contact.

where a is the tip bias in surface coordinates. Partial restoration of the initial surface topography is made by an inverse transformation: the SPM image is *numerically* scanned by an *inverted* tip. Then the restored topography image $R'(x)$ is:

$$R'(x) = I(x_{k1}) - P(x - x_{k1}),$$ under condition that $dI/dx = dP/dx$ in x_{k1} points of contact.

Here x_{k1} is the abscissa of the point of contact of the SPM image function with the inverted tip function (i.e. with reversed directions for Y and X axes).

It is necessary to note, that the full restoration of the sample surface would be possible only if the following two conditions were satisfied: first, during scanning the tip has touched all points of the surface, and, second, the tip has been always touching only one point of the surface. If the tip cannot reach some area of the surface during scanning (for example, if the sample has overhanging parts of topography), then only partial restoration of the topography can be performed. In conclusion, the more points of the surface were touched by the tip during scanning, the more faithfully it is possible to reconstruct the surface.
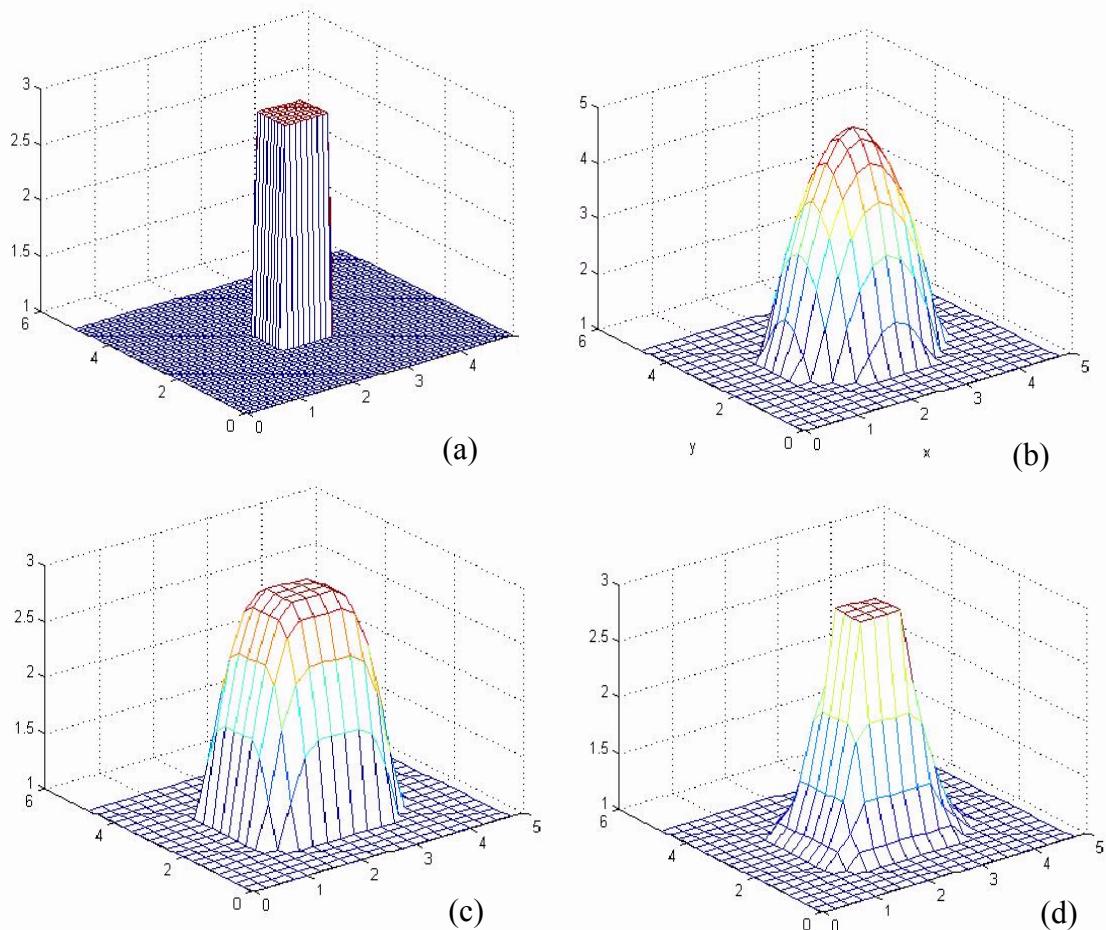
Fig. 35. Modeling of the surface topography restoration process

(a) – initial surface with a relief shaped as a parallelepiped;

(b) – modeling form of the tip as a paraboloid of revolution;

(c) – result of convolution of the tip and initial surface;

(d) – restored image of the surface.

(Dimensions of images on X, Y, Z axes are specified in relative units).

In practice the SPM image and the experimentally obtained tip shape are two-dimensional arrays of discrete values for which the derivative is an ill-defined value. Therefore in practice instead of derivation of discrete functions during numerical deconvolution of the SPM images, the requirement of minimality of the tip-surface distance is used during scanning with a constant average height [17]:

$$Min \; \{I(x_{kl}) - P(x - x_{kl})\} \; .$$

In this case it is possible to accept the minimal distance between the tip point and the corresponding point of a surface for the given position of the tip with respect to the surface as the topographic height. This requirement in its physical sense is equivalent to the requirement of equality of derivatives; however, it allows to search the points of a tip-surface contact with a more adequate method, which essentially reduces the time of topography reconstruction.

Special test structures with known topography are used for calibration and determination of the form of the working part of the tip. Two SEM images of the most commonly used test structures and their characteristic images, obtained by scanning-force microscope are shown in Fig. 36 and Fig. 37.
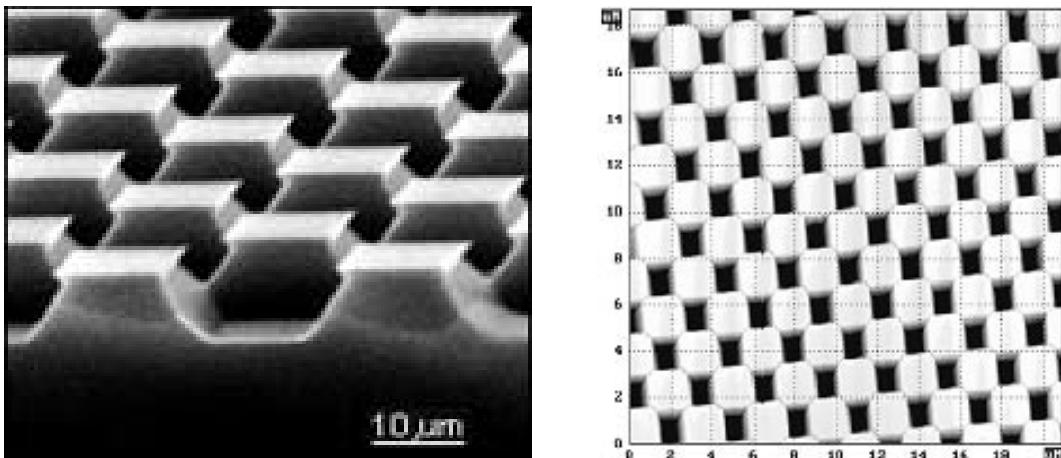
Fig. 36. Rectangular calibration lattice and its SFM image
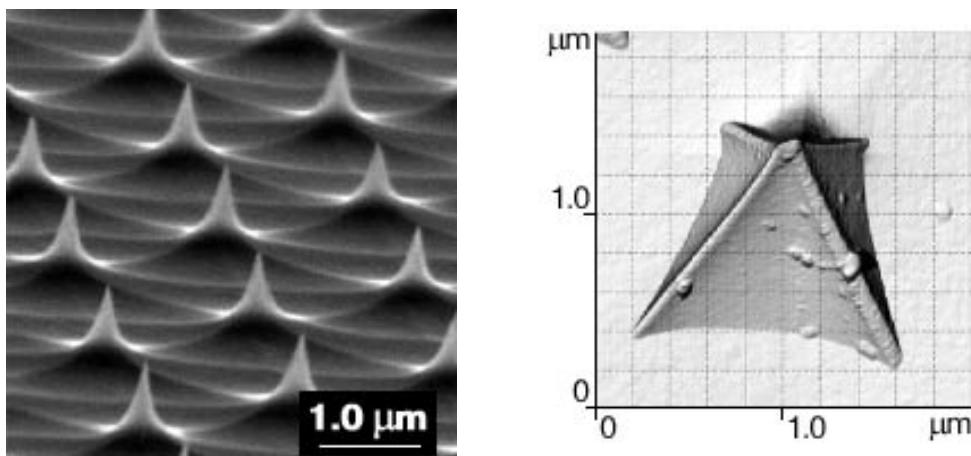
**Fig. 37. Calibration lattice made of sharp pins and its SFM image
obtained by a pyramidal tip**

The calibration lattice made of sharp pins allows to image the tip apex while the rectangular lattice helps to restore the form of the tip lateral surface. Combining the results obtained by scanning these lattices, it is possible to restore completely the form of the working part of tips.
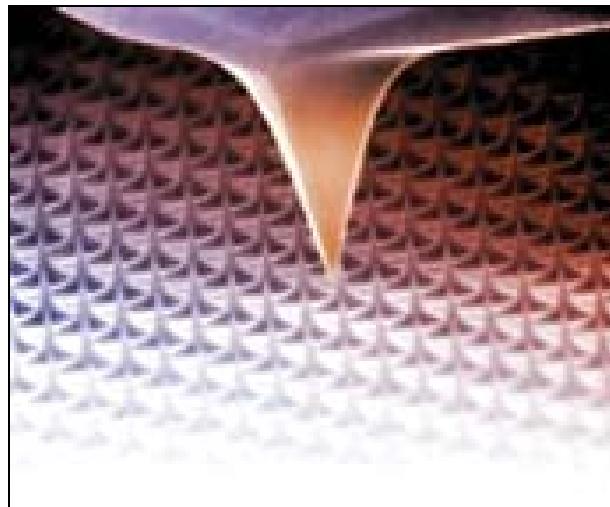
Fig. 38. Electron microscope image of an SPM tip during scanning of a test structure

2. Operating modes in scanning probe microscopy

2.1. Scanning tunneling microscopy

Historically, the first microscope in the family of probe microscopes is the scanning tunneling microscope. The working principle of STM is based on the phenomenon of electrons tunneling through a narrow potential barrier between a metal tip and a conducting sample in an external electric field.
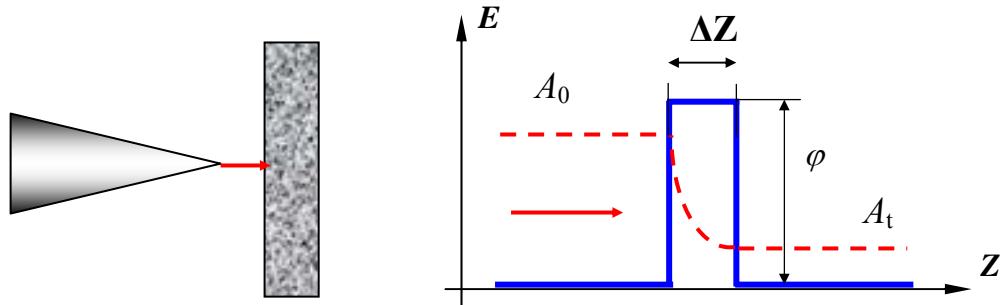

Fig. 39. Scheme of electrons tunneling through a potential barrier in STM

The STM tip approaches the sample surface to distances of several Angstroms. This forms a tunnel-transparent barrier, whose size is determined mainly by the values of the work function for electron emission from the tip (φ_T) and from the sample (φ_S). The barrier can be approximated by a rectangular shape with effective height equal to the average work function φ^*:

$$\varphi^* = \frac{1}{2}(\varphi_T + \varphi_S).$$

From quantum mechanics theory [19,20], the probability of electron tunneling (transmission coefficient) through one-dimensional rectangular barrier is :

$$W = \frac{|A_t|^2}{|A_0|^2} \cong e^{-k\Delta Z}$$

,

where A_0 is the amplitude of electron wave function approaching the barrier; A_t the amplitude of the transmitted electron wave function, k the attenuation coefficient of the wave function inside the potential barrier; ΔZ the barrier width. In the case of tunneling between two metals the attenuation coefficient is

$$k = \frac{4\pi\sqrt{2m\varphi^*}}{h},$$

where m is the electron mass, φ^* the average electron emission work function, h the Planck constant. If a potential difference V is applied to the tunnel contact, a tunneling current appears.
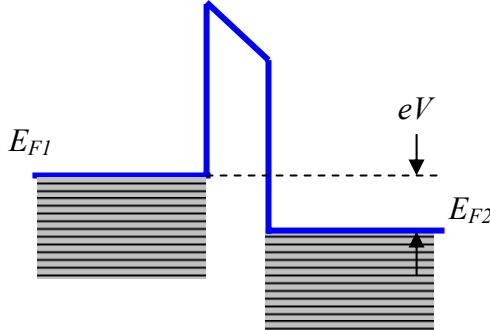

Fig. 40. Energy level diagram of tunneling contact between two metals

Basically, electrons with energy near the Fermi level E_F participate in the tunneling process.
In case of contact of two metals the expression for the tunneling current density (in one-dimensional approximation) is [21,22]:

$$j_t = j_0\left[\varphi^* exp(-A\sqrt{\varphi^*}\Delta Z) - (\varphi^* + eV)exp(-A\sqrt{\varphi^* + eV}\Delta Z)\right], \tag{1}$$

where the parameters j_0 and A are set by the following expressions:

$$j_0 = \frac{e}{2\pi h(\Delta Z)^2}, \qquad A = \frac{4\pi}{h}\sqrt{2m}.$$

For small values of the bias voltage ($eV < \varphi$), the current density can be approximated by a simpler expression. The first order approximation in the series expansion of $exp(-A\sqrt{\varphi^* + eV}\Delta Z)$ in expression (1) gives:

$$j_t = j_0 exp(-A\sqrt{\varphi^*}\Delta Z)\cdot\left(\varphi^* - (\varphi^* + eV)\cdot\left(1 - \frac{AeV\Delta Z}{2\sqrt{\varphi^*}}\right)\right).$$

Finally, for $eV \ll \varphi^*$, we get:

$$j_t = j_0\frac{A\sqrt{\varphi^*}eV\Delta Z}{2}exp(-A\sqrt{\varphi^*}\Delta Z) = \frac{e^2\sqrt{2m\varphi^*}}{h^2}\cdot\frac{V}{\Delta Z}exp\left(-\frac{4\pi}{h}\sqrt{2m\varphi^*}\Delta Z\right).$$

Since the exponential dependence is very strong, an even simpler formula is frequently used for estimations and qualitative reasoning:

$$j_t = j_0(V)e^{-\frac{4\pi}{h}\sqrt{2m\varphi^*}\Delta Z}, \qquad (2)$$

in which the value $j_0(V)$ is assumed to be not dependent on the tip-sample distance. For typical values of the work function ($\varphi \sim 4$ eV) the attenuation coefficient k is about 2 Å^{-1} so, when ΔZ changes of about 1 Å, the current value varies of one order of magnitude. Real tunneling contacts in STM are not one-dimensional and have more complex geometry; however, the basic features of tunneling, namely the exponential dependence of the current on the tip-sample distance, are the same also in more complex models, as proved by experimental results.

For large values of bias voltage ($eV > \varphi^*$), the well-known Fowler – Nordheim formula for electron field emission into vacuum is derived from expression (1):

$$J = \frac{e^3 V^2}{8\pi h \varphi^* (\Delta Z)^2} exp\left[-\frac{8\pi\sqrt{2m}(\varphi^*)^{\frac{3}{2}}\Delta Z}{3ehV} \right].$$

The exponential dependence (2) of the tunneling current on distance allows adjusting the tip-sample distance in a tunneling microscope with high accuracy. The STM is an electromechanical system with a negative feedback. The feedback system FS keeps the tunneling current value at the constant level (I_0), selected by the operator. The control of the tunnel current value, and consequently of the tip-sample distance, is performed by moving the tip along the Z axis with the help of a piezoelectric element (Fig. 41).
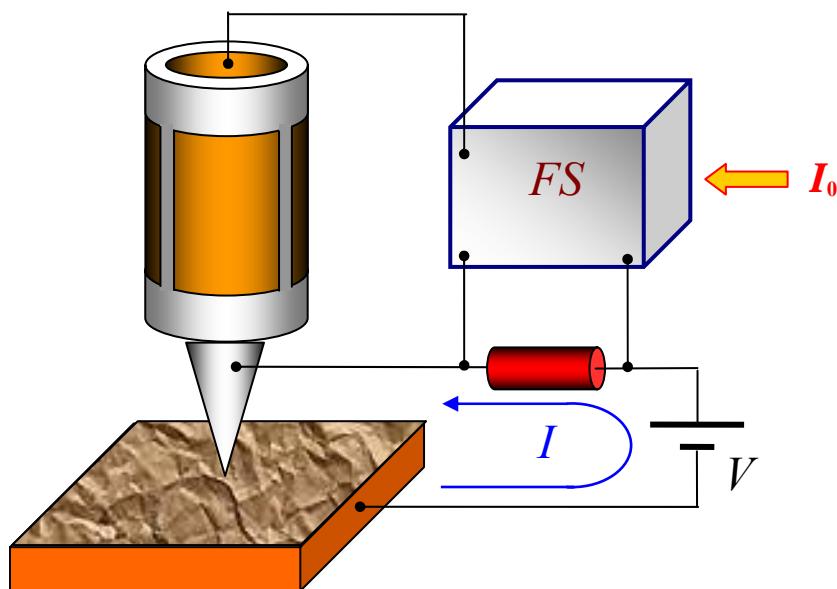

Fig. 41. Simplified block-diagram of the feedback in STM

The image of a surface topography in STM is formed in two ways. In the constant current mode (Fig. 42 (a)) the tip moves along the surface, performing raster scanning; during this the voltage signal applied to the Z-electrode of a piezoelement in the feedback circuit (keeping constant the tip-sample distance with high accuracy) is recorded into the computer memory as a $Z=f(x,y)$ function, and is later plotted by computer graphics.
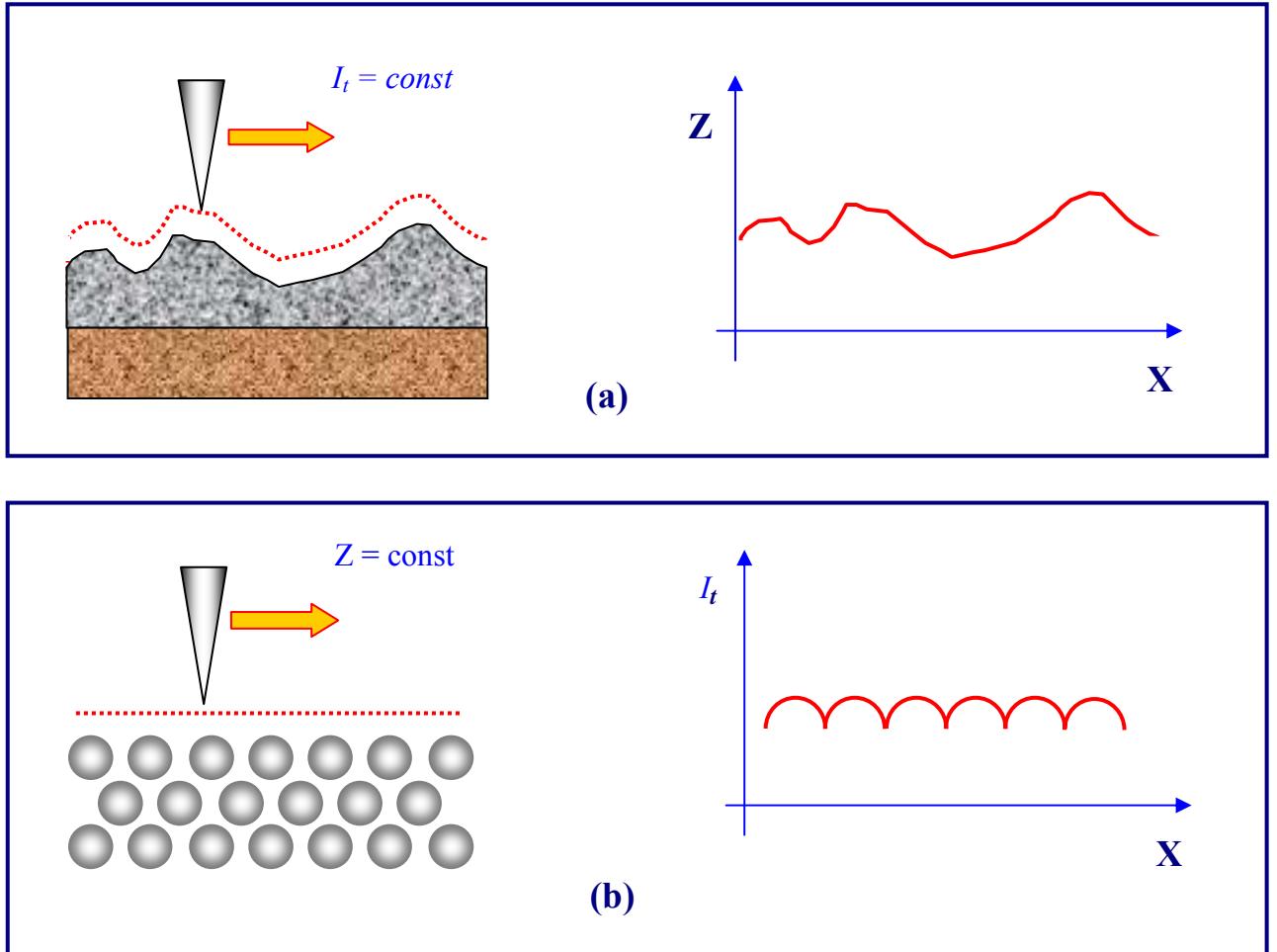

**Fig. 42. Formation of STM images in the constant current mode (a)
and in the constant average distance mode (b)**

During investigation of atomic-smooth surfaces it is often more effective to acquire the STM image in the *constant height mode* (Z = const). In this case the tip moves above the surface at a distance of several Angstrom, and the tunneling current changes are recorded as STM image (Fig. 42 (b)). Scanning may be done either with the feedback system switched off (no topographic information is recorded), or at a speed exceeding the feedback reaction speed (only smooth changes of the surface topography are recorded). This way implements very high scanning rate and fast STM images acquisition, allowing to observe the changes occurring on a surface practically in real time.

The high spatial resolution of the STM is due to the exponential dependence of the tunneling current on the tip-sample distance. The resolution in the direction normal to the surface achieves fractions of Angstrom. The lateral resolution depends on the quality of the tip and is determined

basically not by the macroscopic radius of curvature of the tip apex, but by its atomic structure. If the tip was correctly prepared, there is either a single projecting atom on its apex, or a small cluster of atoms, whose size is much smaller than the mean curvature radius of the tip apex. In fact, the tunneling current flows between atoms placed at the sample surface and atoms of the tip. The atom, protruding from the tip, approaches the surface to a distance comparable to the crystal lattice spacing. Since the dependence of the tunneling current on the distance is exponential, the current basically flows in this case between the sample surface and the projecting atom on the apex of the tip.
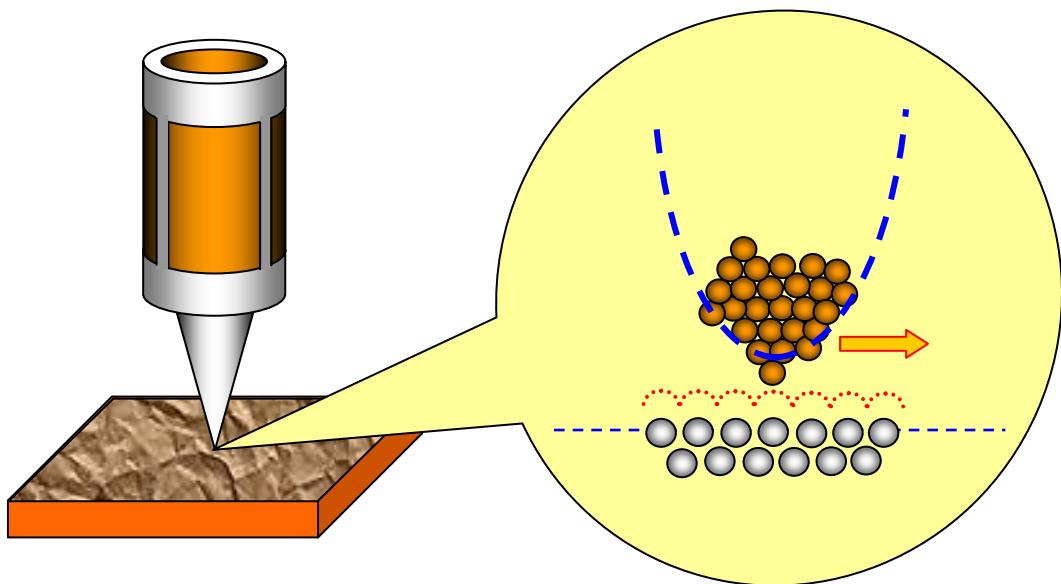
Fig. 43. Atomic resolution in a scanning tunneling microscope

Using such tips it is possible to achieve a spatial resolution down to atomic scale, as demonstrated by many research groups using samples from various materials.

<u>Tips for tunneling microscopes</u>

Tips of several types are used in scanning tunneling microscopes. In the beginning tips made from a tungsten wire by electrochemical etching were widely used. This technology was well known and was used for field-emission microscopes. The preparation of STM tips using this technology is the following. A tungsten wire segment is fixed so that one of its ends passes through a conducting diaphragm (D) that keeps a drop of alkali KOH in water solution (Fig. 44)
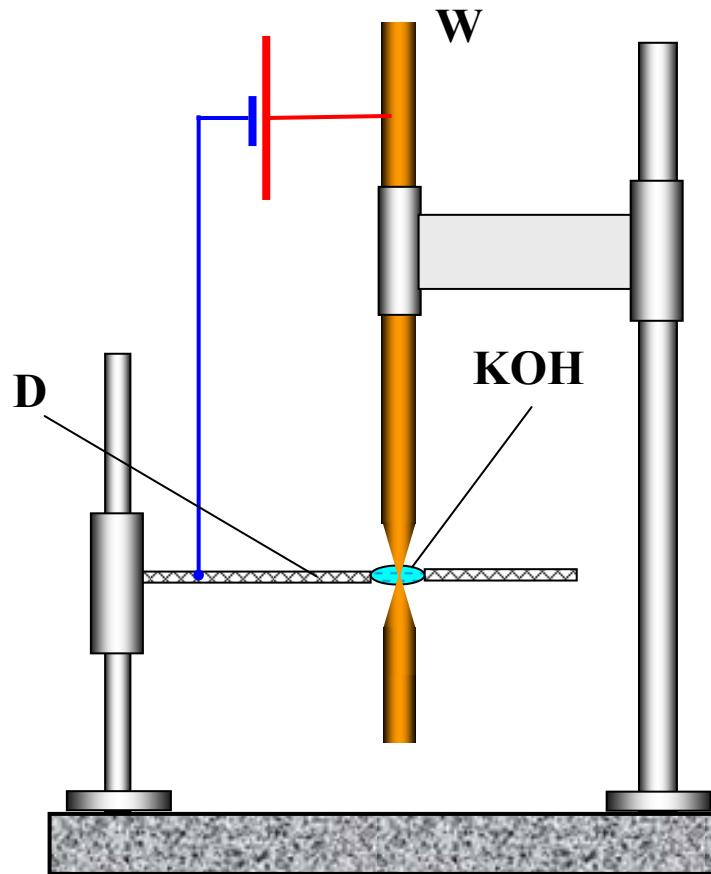
Fig. 44. Scheme of a device for tungsten wire electrochemical etching to prepare STM tips

Feeding an electric current through the wire and the KOH solution, tungsten etching occurs. As far as etching goes, the thickness of the etched area gets smaller until the wire breaks, due to weight of its bottom part. The bottom part falls down, automatically switching off the electric circuit and terminating the etching.

Another widely used technique of STM tips preparation is cutting of a thin wire from Pt-Ir alloy using ordinary scissors. The cutting is made at an angle about 45 degrees with simultaneous P tension of the wire to tear it apart (Fig. 45).
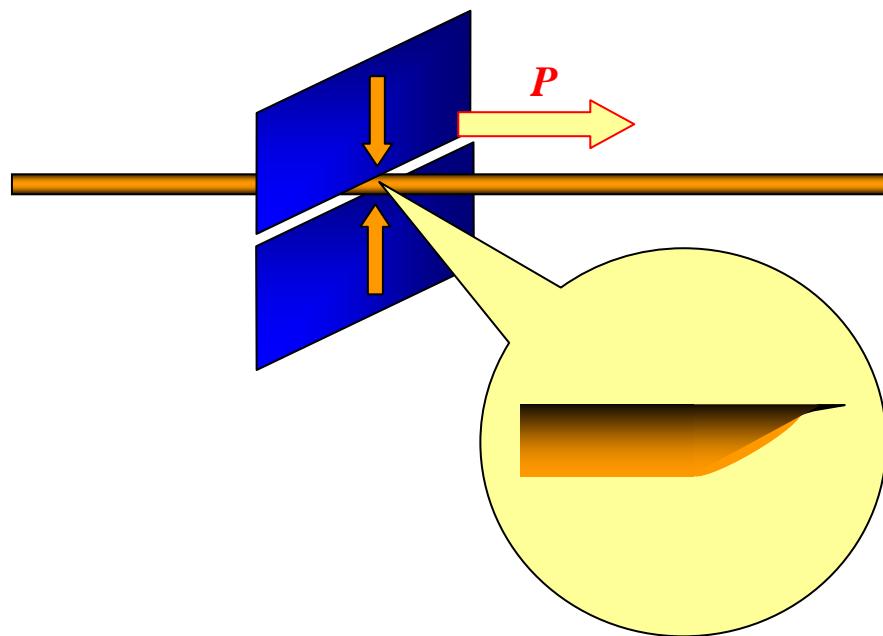
Fig. 45. Schematic picture of the STM tip preparation by cutting a Pt-Ir alloy wire

The wire is cut while applying a stretching force P that produces a plastic deformation of the wire. As a result, in the place of cutting an extended apex with a ragged (curled) edge is formed with several protrusive defects, one of which becomes the working element of the STM tip. This manufacturing technique of STM tips is now used in all laboratories and provides almost always the guaranteed atomic resolution.
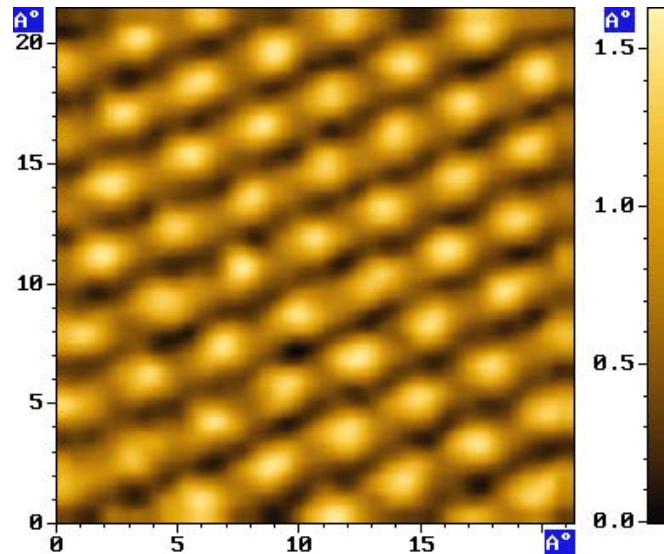
Fig. 46. STM image of atomic structure of pyrolitic graphite

Measurement of the local work function with STM

For non-uniform samples the tunneling current is not only a function of tip-sample distance, but also depends on the local value of the work function on the sample surface. The method of tip-sample distance modulation is used to obtain a map of the work function. For this purpose, during scanning, a variable voltage with frequency ω is added to the control voltage of the scanner Z-electrode. The voltage applied to the Z-electrode of the scanner is therefore

$$U(t) = U_0 + U_m \, sin(\omega t).$$

The tip-sample distance becomes modulated at the frequency ω:

$$\Delta Z(t) = \Delta Z_0 + \Delta Z_m \, sin(\omega t),$$ where ΔZ_m and U_m are related by the scanner piezoelectric coefficient K:

$$K = \frac{\Delta Z_m}{U_m}$$

The value of the frequency ω is selected higher than the maximum frequency of the bandwidth of the feedback loop so that the feedback system cannot react to the tip-sample distance modulation. The amplitude of the voltage U_m is small enough to be neglected in the weak dependence of the tunneling current on the applied voltage.
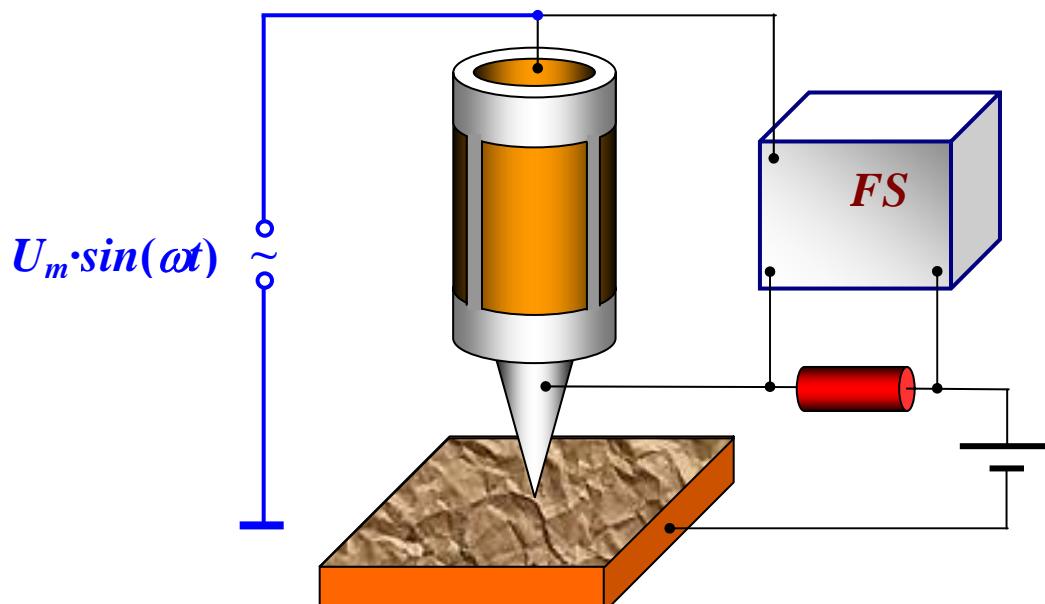
**Fig. 47. Setup for local work function measurement**

In turn, the oscillations of the tip-sample distance modulate the current at the frequency ω :

$$I_t \cong I_0(V) e^{-\alpha \sqrt{\varphi^*} \left[\Delta Z_0 + \Delta Z_m sin(\omega t)\right]},$$ where $\alpha = \frac{2}{\hbar} \sqrt{2m}$.

Since the modulation amplitude is small, the tunneling current can be written as

$$I_t(\omega t) \cong I_o(V)e^{-\alpha\sqrt{\varphi}\Delta Z_0}\left[1 - \alpha\sqrt{\varphi}\Delta Z_m \sin(\omega t)\right].$$

Thus, the amplitude of the small tunneling current oscillations with frequency $\rceil$ is proportional to the square root of the local work function:

$$I_\omega = I_0\frac{2KU_m}{\hbar}\sqrt{2m\varphi^*(x,y)}.$$

Measuring the tunneling current amplitude oscillations in each point of the frame, it is possible to build a map of the local work function $\varphi(x, y)$ simultaneously with the $Z = f(x, y)$ topography on the scanned area of a sample.

Measurement of tunnel contact volt-ampere characteristics

Using STM it is possible to measure the tunnel contact volt-ampere characteristics (VAC or I-V curves) that give information on the local conductivity of the sample and on the local density of electron states. The following procedure is the following. The sample area where measurements will be performed, is selected on a previously acquired STM image. The STM tip is moved by the scanner to the first point of the selected area. To acquire I-V curves the feedback is broken for a short time, and a linearly increasing voltage is applied to the tunneling junction. During the ramp, both the current flowing through the junction and the applied voltage are recorded.
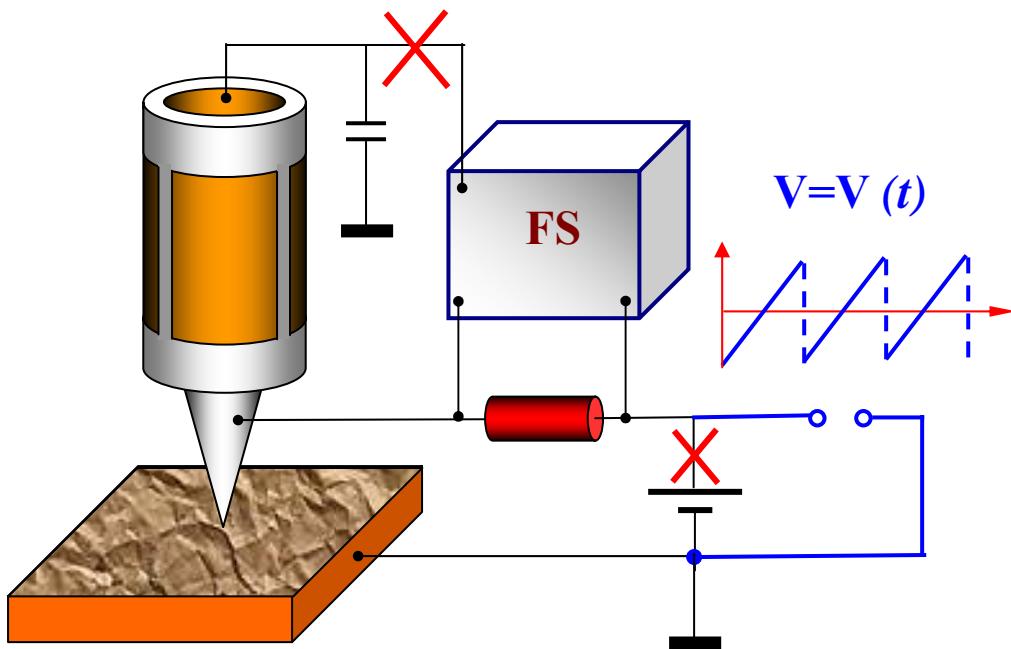

Fig. 48. Schematic picture of the tunneling junction I-V curves acquisition

Several I-V curves are measured in every point. Final volt-ampere characteristic is obtained by averaging the I-V set, measured in one point. Averaging allows to minimize the influence of noise.

STM control system

A simplified block diagram of the STM control system is presented in Fig. 49. The STM control system consists of a digital part implemented by a personal computer, and an analog part, provided usually as a standalone block. The digital part consists of DAC and ADC sets and is enclosed on the scheme by red dotted border. The analog part is enclosed by a blue dashed line. The voltage U applied to the tunnel junction is set by the operator through a DAC, and the current I, controlled by the feedback system, is also set through a DAC. Two-channel digital-to-analog converters (DAC-X and DAC-Y) provide horizontal and vertical raster-scanning. The feedback loop is made of the preamplifier PA (located in the STM measuring head), the differential amplifier DA, the low-frequency filter LFF, amplifiers A4 and A5, and the piezo-scanner, controlling the tunneling gap.
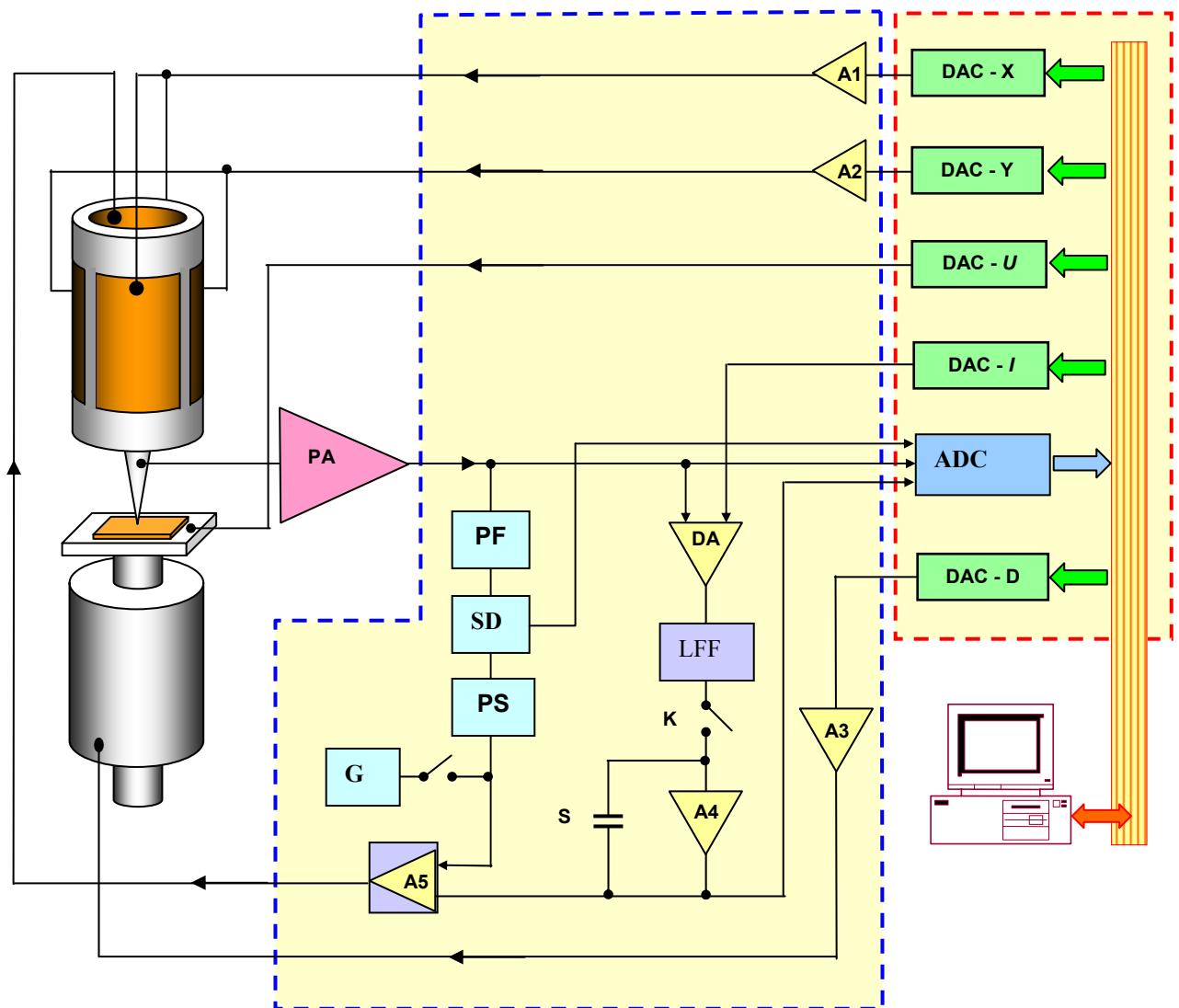
Fig. 49. The block diagram of an STM control system

The operator first select suitable values for the working parameters (tunneling current and applied voltage) then starts the procedure for the tip-sample approach, by feeding a control voltage to the motor through the DAC–D converter. In the initial state there is no current in the feedback loop, and the scanner is extended as much as possible toward the sample. When the tunneling current appears,

the feedback start retracting the scanner, while the system switches to a feedback mode. In this mode while the scanner is retracting the step motor approaches the sample to the tip until the scanner sets in the middle of its dynamic range. The value of a tunneling current set by the operator is kept constant in the feedback loop during the approach.

The sample scanning is performed by feeding a saw tooth voltage to external electrodes of the tubular scanner through the DAC–X and DAC–Y and the high-voltage amplifiers A1 and A2. During scanning the feedback system keeps the tunneling current constant. The real instantaneous value of the tunneling current I_t is compared by the differential amplifier to the value I_0, preset by the operator. The differential signal $(I_t - I_0)$ is amplified (by A4 and A5 amplifiers) and fed to the inner Z-electrode of the scanner. Thus, the voltage applied to the Z-electrode during scanning reproduces the surface topography. The signal from the A4 amplifier output is digitized by the ADC converter and stored in the computer memory.

To acquire the information on the local work function distribution the signal produced by the generator G is added by the amplifier A5 to the Z-electrode voltage. The signal corresponding to the tunneling current modulation at frequency ω is selected by band-pass filter (PF) and measured by the synchronous detector SD, driven by the reference voltage supplied by the signal generator G. The phase of the reference voltage is controlled by the phase shifter PS. The amplitude of the current modulation is recorded in the computer memory as a signal proportional to the local work function.

The measurement of the tunneling junction I-V curves in a set point of a sample is performed as follows. The feedback is switched off for a short time using the electronic switch K. The voltage on the inner electrode of the piezo-tube is kept constant by the capacitor C so that the tip hangs above the surface for a short time. After that the saw tooth voltage $U(t)$ is applied to the tunneling junction from the converter DAC $-U$, and synchronously with it the tunneling current from the preamplifier PU output is recorded in ADC. After that the switch K is closed, and the feedback system restores the tunneling contact state corresponding to the $I_t = const$ condition. If necessary, the measurement of I-V curves is repeated N times to calculate an average curve.

Scanning tunnel microscope design

Today hundreds of different scanning probe microscope designs are described in the literature. On one hand, such variety SPMs is caused by practical necessity, since certain SPM configuration is needed to solve specific tasks. On the other hand, the relative simplicity of some SPM mechanical part stimulates manufacturing of measurement heads customized for specific experiments designed in research laboratories.

The structure of STM measuring head must satisfy a lot of requirements in order to achieve a satisfactory performance. The most important requirement is high noise immunity. It is due to the high sensitivity of the tunneling gap to external vibrations, to temperature drifts, to electric and acoustic interference. Wide experience has been accumulated during last decade in this direction; many ways of shielding STM from influence of external factors have been developed. Finally, the choice of the vibration isolation and thermal compensation system is dictated, basically, by the convenience of use.

As an example, an STM head design, with thermal drift compensation of the tip position, is schematically shown on Fig. 50.
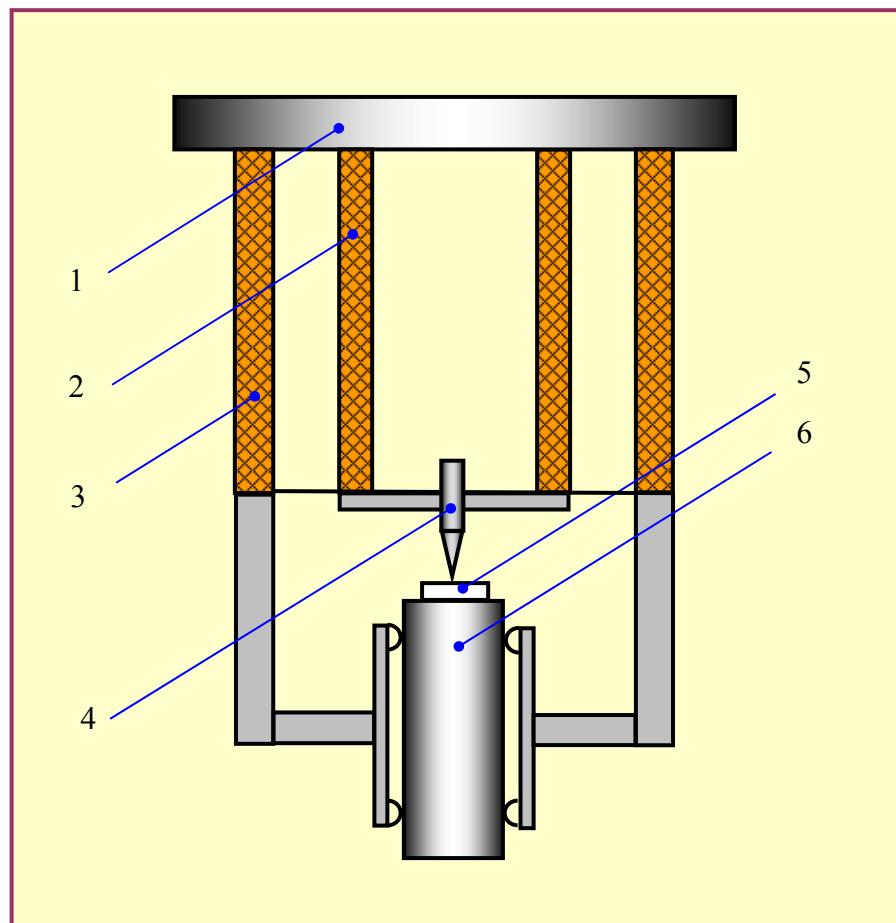
Fig. 50. An example of STM measuring head design
1 - base; 2 – tubular three-coordinate piezo-scanner;
3 – temperature-compensating piezo-tube, serving as a working element
of a step-by-step piezo-motor; 4 –tip; 5 – sample;
6 - cylindrical sample holder

The base (1) holds two coaxial piezoceramic tubes of different diameter. The internal tube (2) plays the role of a three-axes piezo-scanner. The external tube (3) performs a double task. First, the external tube cancels the deformations due to temperature changes, stabilizing the tip position in the direction normal to the sample surface. Second, it is the working element of a step-by-step piezo-motor, serving to approach the tip to the sample. The whole STM construction has axial symmetry that reduces tip position thermal drift in the plane of the sample surface.

Tunneling spectroscopy

The scanning tunnel microscope allows to record volt-ampere characteristics (VAC) of tip-surface tunneling contact in any point of a surface and to investigate the local electric properties of a sample. With the typical values of about 0.1–1 V for the bias of the tunneling contact and tunneling currents at a level of 0.1÷1 nA, the order of magnitude of the tunneling contact resistance R_t is $10^8 \div 10^{10}$ Ohm. As a rule, the R_S resistance of samples studied in STM is much less than R_t and the VAC is defined, basically, by the properties of a small sample area near the tunneling contact.

$$R_S \ll R_t$$
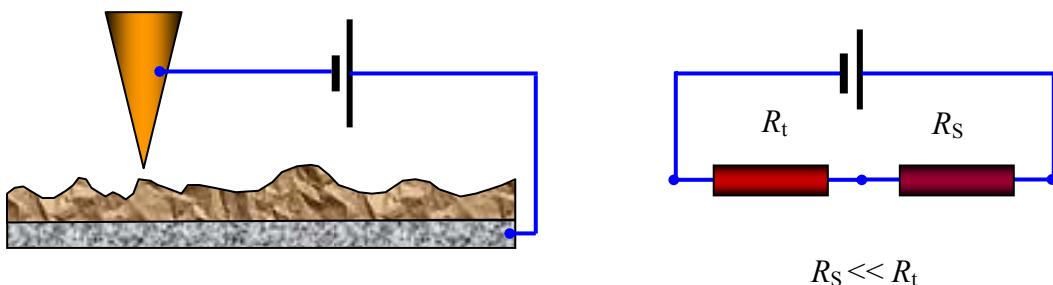
Fig. 51. Equivalent scheme of a tunneling contact

The tunneling VAC essentially depends on the electrons energy distribution in the sample. Fig. 52 shows a schematic picture of the electron energy states in a tunneling contact between two metals.
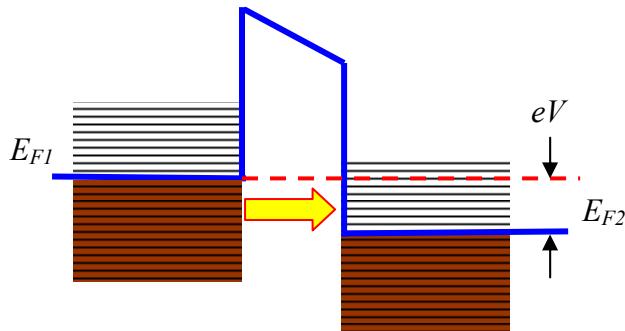

Fig. 52. Schematic picture of the electron energy states in a tunneling contact between two metals

Mainly electrons with energies near to Fermi level participate in the tunneling current. During forward bias (Fig. 52) the electrons are tunneling from the filled states in the conduction band of the tip to the free states the conduction band of the sample. During reverse bias the electrons are tunneling from the sample to the tip. The value of the tunneling current is defined by the bias voltage, the barrier transmission coefficient and the density of states near Fermi level. The expression for the tunneling current in case of a discrete electron energy spectrum has been calculated in the literature [23-25]. In the approximation of near-continuous electron energy spectrum the expression for the tunneling current is the following [22,26]:

$$dI = A \cdot D(E)\rho_P(E)f_P(E)\rho_S(E)(1 - f_S(E))dE,$$

where A is a constant; $D(E)$ the barrier transparency; $\rho_P(E)$, $\rho_S(E)$ the density of states in the tip and in the sample, respectively; $f(E)$ is the Fermi distribution function. In the simplest case of a rectangular barrier at low temperatures and with the assumption, that the density of states near Fermi level in the tip is practically constant, the expression for the current can be written as

$$I(V) = B \int_0^{eV} \rho_S(E)dE$$

In this case the dependence of the tunneling current on the voltage is determined, basically, by the density of states in the sample. In practice the $\rho_S(E)$ value is estimated from the value of the tunneling current derivative with respect to voltage:

$$\rho_S(eV) \approx \frac{\partial I}{\partial V}.$$

Measurements of local tunneling spectra of various materials is performed, as a rule, in high vacuum (since the tunneling current is very sensitive to the state of the sample surface) and at low temperatures (since the thermal excitations strongly dither the features in the collected spectra).

Metal - metal tunneling junction

Electron tunneling through a barrier between two metals was studied in many experimental works long before the STM invention [27,28]. As it has been shown above, for small bias voltages the dependence of the tunneling current on the bias voltage is linear, and the conductivity of the tunneling contact is defined, basically, by the barrier shape:

$$j_t = j_0(V)\, e^{-\frac{4\pi}{h}\sqrt{2m\varphi^*}\,\Delta Z}.$$

At very high voltages the barrier shape will strongly change, and the current will be described by the Fowler-Nordheim formula. A typical VAC, observed for metal-metal tunneling contacts, is represented schematically on Fig. 53.
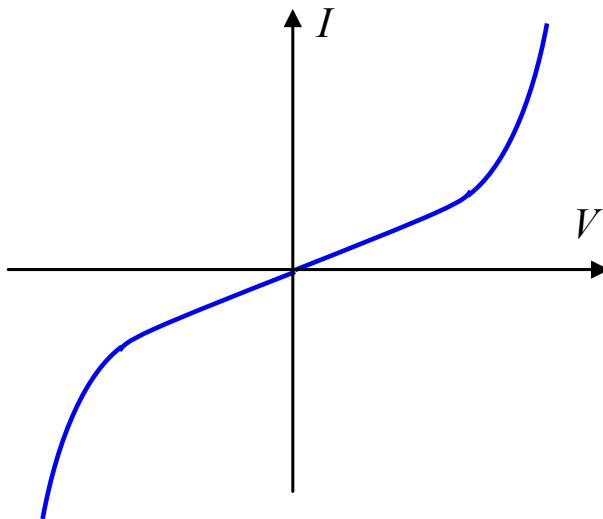

Fig. 53. Generic metal-metal tunneling contact VAC

As it can be seen from the figure, the volt-ampere characteristic of the metal-metal tunneling contact is nonlinear and, as a rule, it is practically symmetric.

Metal–semiconductor contact VAC

Semiconductor samples have more complex structure of the electron energy spectrum.
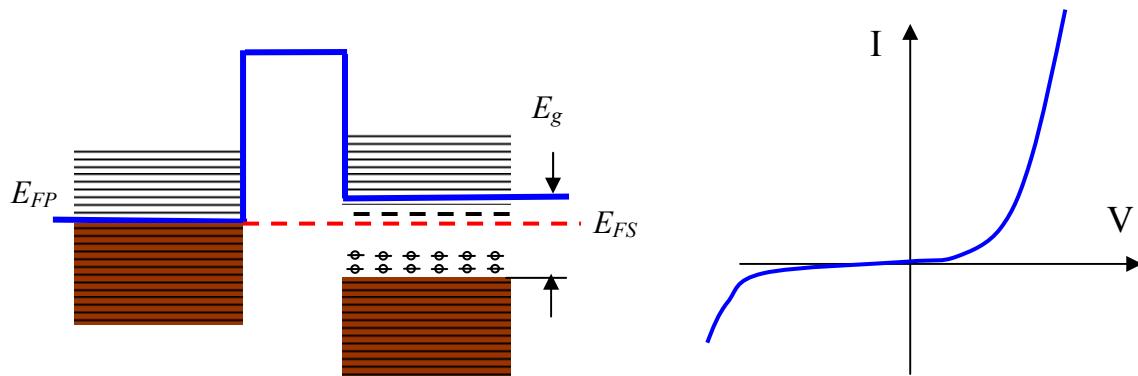

Fig. 54. Energy levels and generic VAC for metal-semiconductor tunneling contact

Presence of an energy band gap and impurity levels in semiconductor materials makes the VAC of a metal-semiconductor tunneling contact strongly nonlinear. Essential contribution to the tunneling current is made also by the surface states and by the energy levels due to foreign atoms adsorbed on the surface. Therefore measurements of local tunneling spectra of semiconductor materials are performed in high vacuum. Uncontrollable presence of adsorbed atoms on the surface strongly complicates the interpretation of the tunneling spectra obtained in experiment. Besides that, thermal excitations result in significant widening of discrete energy levels corresponding to localized states, and also strongly dither the position of the conduction and valence band edges. As an example, the tunneling spectrum of a GaAs sample [29] is presented on Fig. 55.
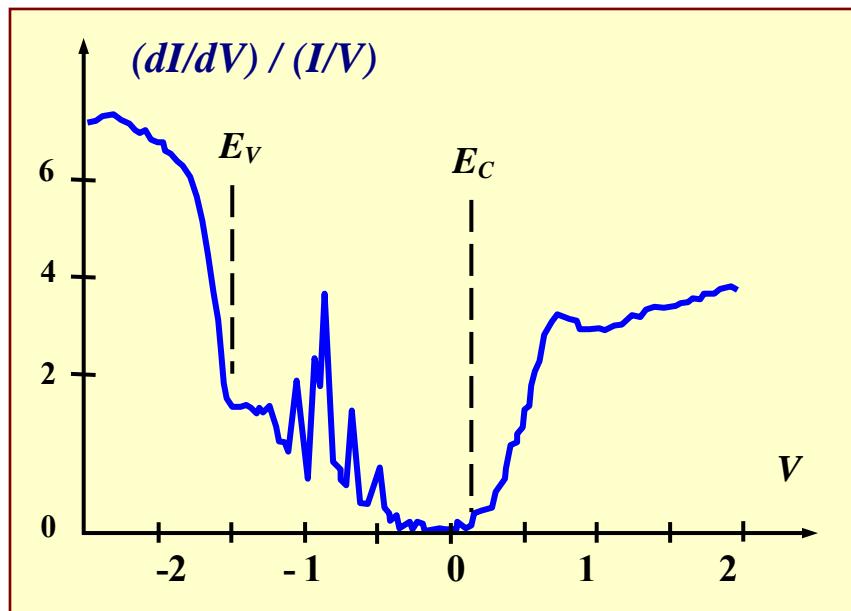

Fig. 55. STM spectrum of a n-GaAs crystal surface

Tunneling spectra allow to determine the position of the edges of the conduction and valence band with respect to the Fermi level, and also to identify the spectral peaks due to impurity states inside the energy gap in semiconductors.

Metal-superconductor contact VAC

In superconducting materials a phase transition occurs, with a reorganization of the electron energy level distribution at temperatures below the critical one. At low temperatures electrons form the superconducting pairs and are condensed at an energy level placed below the conduction band, and separated by an energy gap Δ. The energy levels distribution in a metal–superconductor contact is schematically shown in Fig. 56 [30].
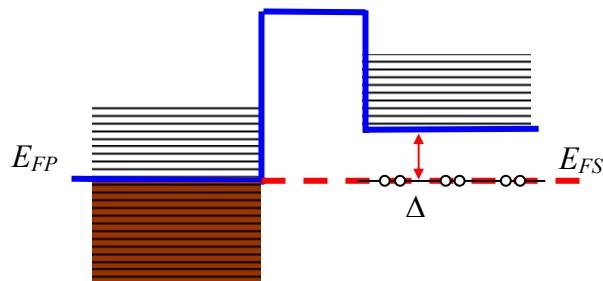
Fig. 56. Electron energy levels in a metal–superconductor contact

With forward bias the tunneling current flows only for eV > Δ voltage. For simplicity we neglect the potential drop across the thin barrier, and the electrons tunnel from the tip into the free states of the superconducting sample (Fig. 57 (a)).

(a)

(b)
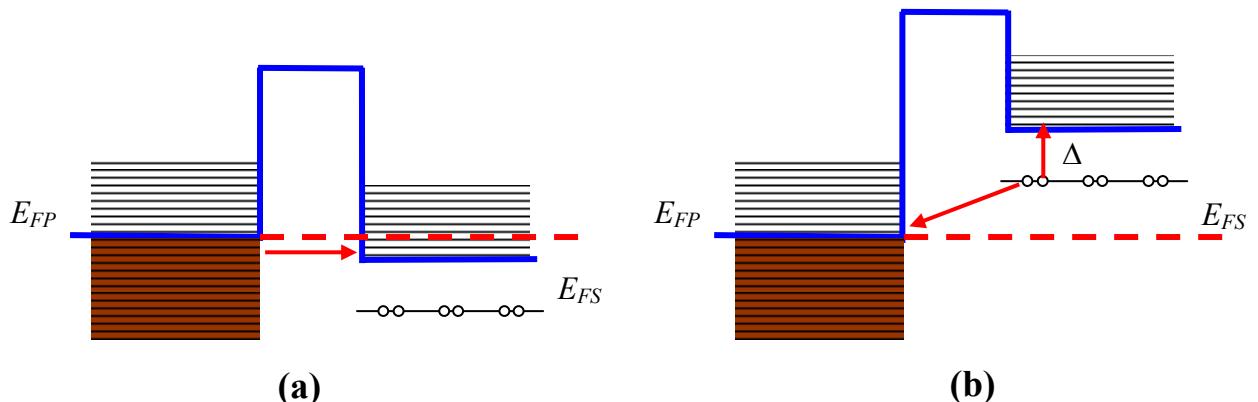
**Fig. 57. Electron energy levels in metal– superconductor contact
during forward (a) and reverse(b) bias**

During reverse bias the picture of tunneling is little bit more complex. Since during tunneling the energy of the system is conserved, the tunneling process in this case occurs as follows. The superconducting pair is split; thus one electron leaves with a loss of energy to the free state near the metal Fermi level, and the second electron, receiving the Δ energy, jumps to an excited state in the superconductor band. Thus, the volt-ampere characteristic of a metal-superconductor tunneling contact at temperature T = 0 contains two branches at $|eV| > \Delta$ (Fig. 58 (a)). The corresponding density of states in a superconductor spectrum is presented on Fig. 58 (b).
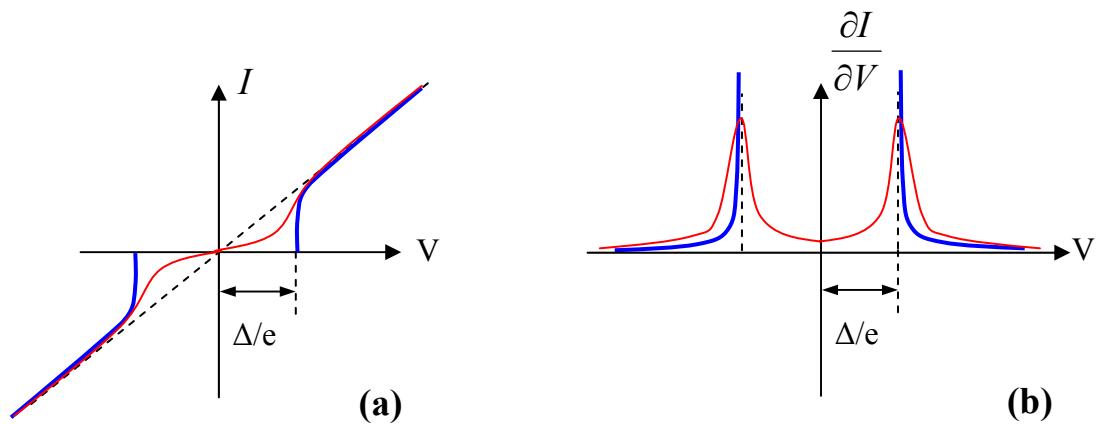
**Fig. 58. Volt-ampere characteristic of a metal-superconductor contact (a)
and density of states of a superconductor (b) at T = 0 (shown in dark blue color).
(Red color shows the VAC and the density of states at T ≠ 0)**

At non-zero temperatures the electron density of states is partly dithered, so the spectral features of superconductors are less precisely described by the measured volt-ampere characteristics.

One of the scanning tunnel microscopy and spectroscopy applications is the study of electric properties of heterogeneous samples. In this case the simultaneous analysis of the surface morphology and the volt-ampere characteristics (measured in various points of the surface), allows to investigate the distribution of various phases of composite structures, to investigate correlations between technological parameters and electronic properties. In particular, measuring a VAC in various points of a surface, it is possible to investigate the distribution of a superconducting phase in samples of non-uniform structure. For this purpose VAC is measured in every point during scanning simultaneously with the surface topography. The value of Δ parameter, which is recorded in a separate file, is calculated using local VAC. $\Delta = f(x,y)$ distribution is built henceforth, characterizing the structure of the superconducting state of the sample.

2.2. Atomic force microscopy

Atomic force microscope (AFM) was invented in 1986 by Gerd Binnig, Calvin F. Quate and Christopher Herber [31]. The AFM working principle is the measurement of the interactive force between a tip and the sample surface using special probes made by an elastic cantilever with a sharp tip on the end (Fig. 59). The force applied to the tip by the surface, results in bending of the cantilever. Measuring the cantilever deflection, it is possible to evaluate the tip–surface interactive force.
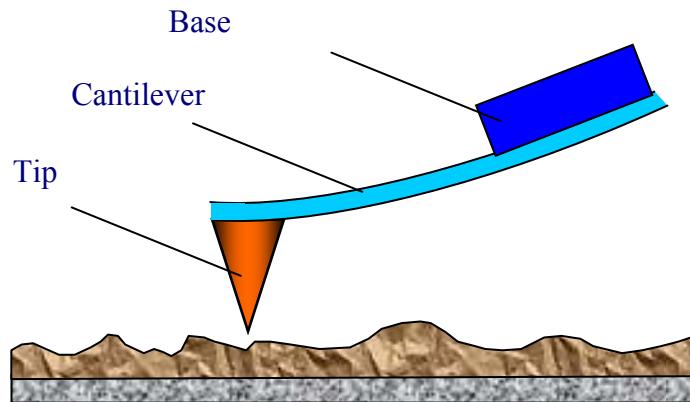
Fig. 59. AFM probe schematic picture

The interactive forces measured by AFM can be qualitatively explained by considering, for example, the van der Waals forces [32]. The van der Waals potential energy of two atoms, located at a distance r from each other, is approximated by the exponential function - Lennard-Jones potential:

$$U_{LD}(r) = U_0 \left\{ -2\left(\frac{r_0}{r}\right)^6 + \left(\frac{r_0}{r}\right)^{12} \right\}.$$

The first term of the sum describes the long-distance attraction caused, basically, by a dipole-dipole interaction and the second term takes into account the short range repulsion due to the Pauli exclusion principle. The parameter r_0 is the equilibrium distance between atoms, the energy value in the minimum.
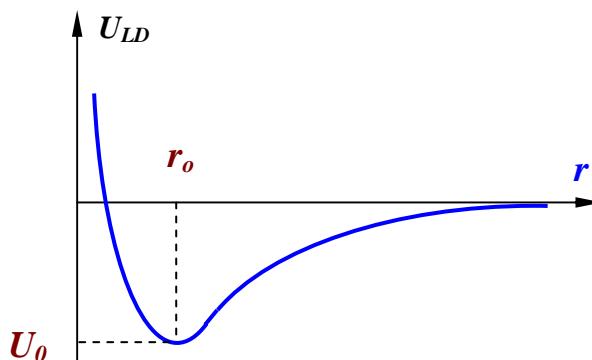
Fig. 60. Lennard-Jones potential qualitative form

Lennard-Jones potential allows to estimate the interaction force of a tip with a sample [33]. The energy of the tip-sample system can be derived, adding elementary interactions for all the tip and sample atoms.
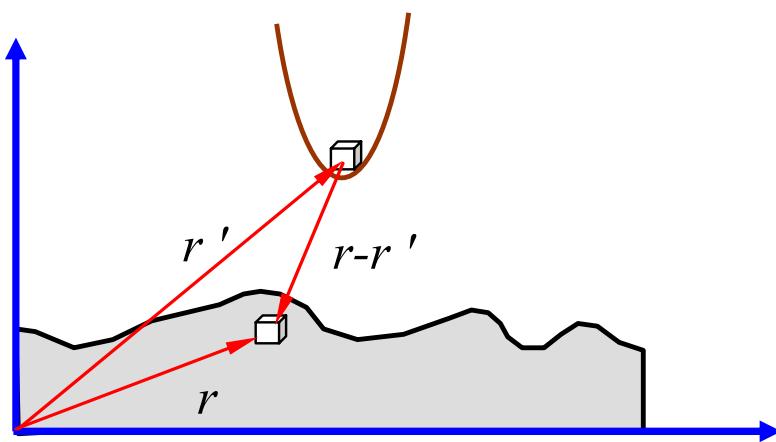
Fig. 61. How to calculate the energy of interaction between tip and sample atoms

Then for the energy of interaction we get:

$$W_{PS} = \iint_{V_P V_S} U_{LD}(r - r')\, n_P(r')\, n_S(r)\, dV\, dV' \;,$$

where $n_S(r)$ and $n_P(r')$ are the densities of atoms in the sample and in the tip. Accordingly, the force affecting the tip from a surface can be calculated as follows:

$$\vec{F}_{PS} = -grad(W_{PS})\,.$$

Generally this force has both a component normal to the sample surface and a lateral component (laying in the plane of the sample surface). Actual interaction of a tip with a sample has more complex character; however, the basic features are the same : the AFM tip is attracted by the sample at large distances and repelled at small distances.

Acquisition of an AFM surface topography may be done by recording the small deflections of the elastic cantilever. For this purpose optical methods (Fig. 62) are widely used in atomic force microscopy (the technique named *beam-bounce*).
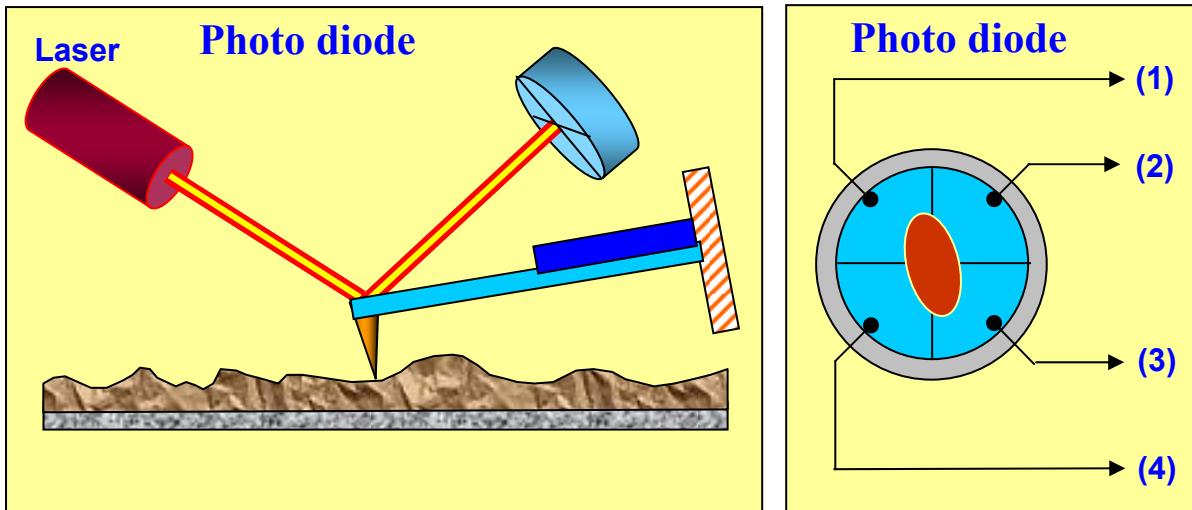
Fig. 62. Schematic description of the optical system to detect the cantilever bending

The optical system is aligned so that the beam emitted by a diode-laser is focused on the cantilever, and the reflected beam hits the center of a photodetector. Four-section split photodiodes are used as position-sensitive photodetectors.
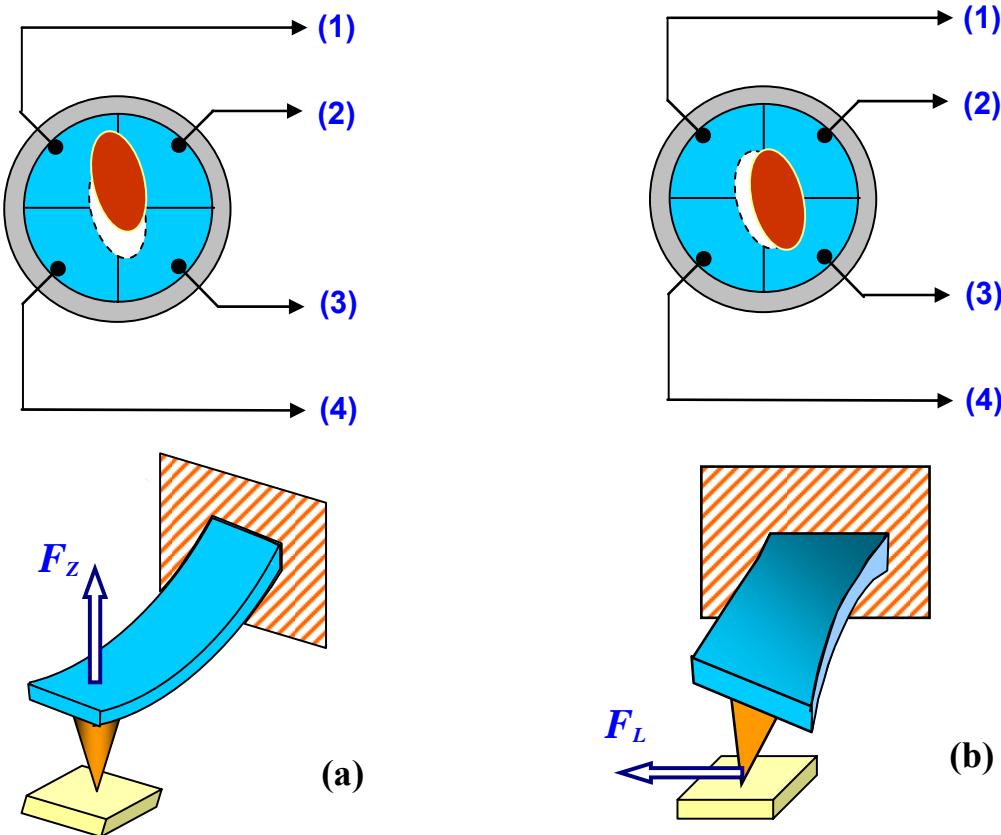
Fig. 63. Relation between the types of the cantilever bending deformations (bottom) and the change of the spot position on the split photodiode (top)

Two quantities may be measured by the optical system: the cantilever bending due to attractive or repulsive forces (F_Z) and the cantilever torsion due to lateral components (F_L) of the tip-surface interaction forces. If reference values of the photocurrent in the photodiode sections are designated as $I_{01}, I_{02}, I_{03}, I_{04}$, and I_1, I_2, I_3, I_4 are the current values after change of the cantilever position, then differential currents from various sections of the photodiode $\Delta I_i = I_i - I_{0i}$ will characterize the value and the direction of the cantilever bending or torsion. In fact, the following current difference

$$\Delta I_z = (\Delta I_1 + \Delta I_2) - (\Delta I_3 + \Delta I_4)$$

is proportional to the cantilever bending due to a force normal to the sample surface (Fig. 63 (a)), and the following combination of differential currents

$$\Delta I_L = (\Delta I_1 + \Delta I_4) - (\Delta I_2 + \Delta I_3)$$

characterizes the cantilever bending due to lateral forces (Fig. 63 (b)).

The ΔI_Z value is used as an input parameter in a feedback loop of the atomic force microscope (Fig. 64). The feedback system (FS) keeps $\Delta I_Z = const$ with the help of a piezoelectric transducer (scanner), which controls the tip-sample distance in order to make the bending ΔZ equal to the value ΔZ_0 preset by the operator.
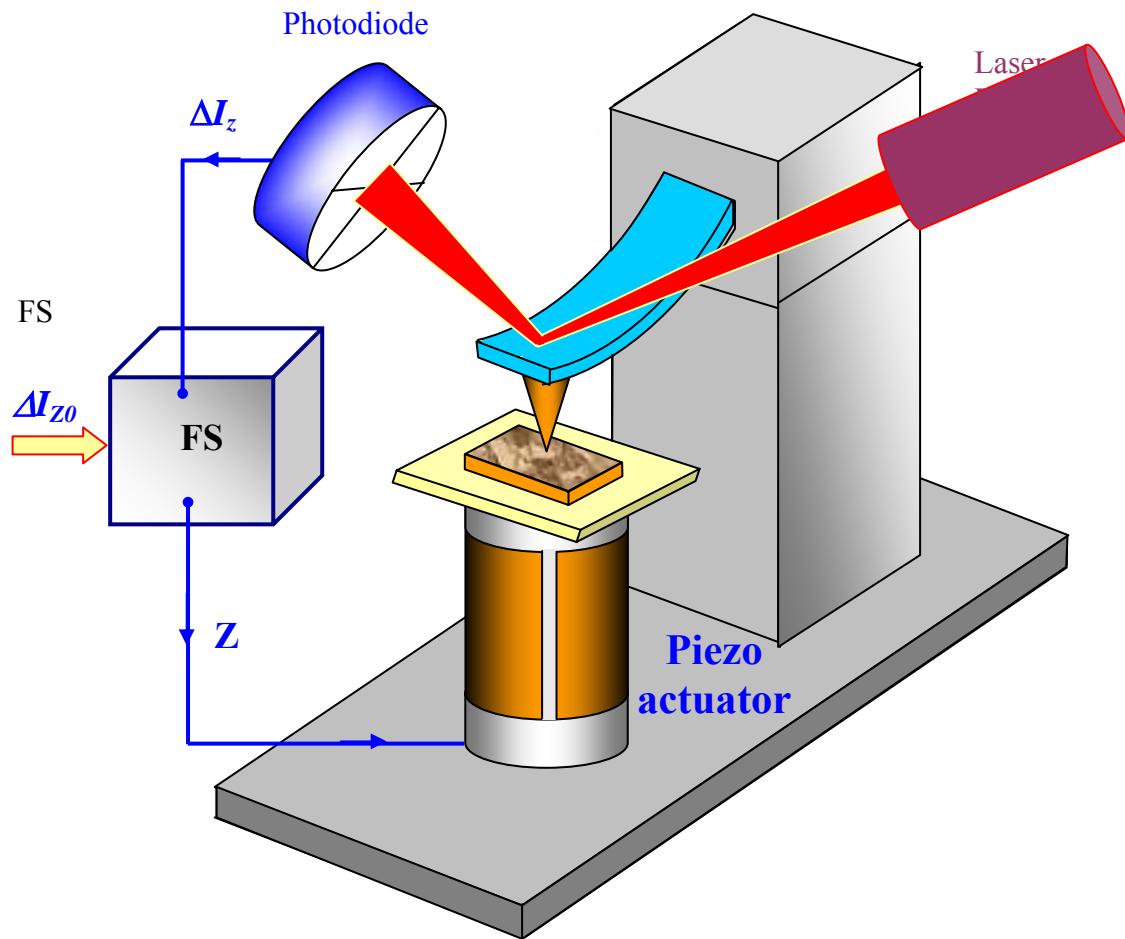
Fig. 64. Simplified scheme of the feedback in an optical lever detection AFM

When scanning a sample in a $\Delta Z = const$ mode the tip moves along the surface, thus the voltage on the scanner Z-electrode is recorded in the computer memory as a surface topography $Z = f(x, y)$. The AFM lateral resolution is defined by the radius of curvature of the tip and by the sensitivity of the system in detecting the cantilever deviations. Currently the AFM are designed to allow obtaining atomic resolution.

AFM probes

Surface sensing in the atomic force microscope is performed using special probes made of an elastic cantilever with a sharp tip on the end (Fig. 65). Such probes are produced by photolithography and etching of silicon, SiO_2 or Si_3N_4 layers deposited onto a silicon wafer.
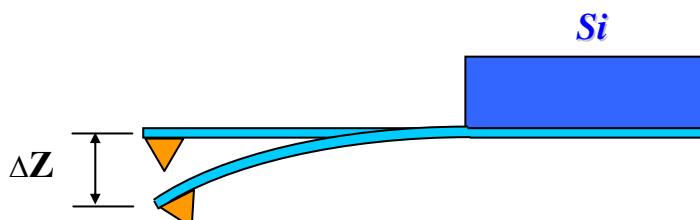
Fig. 65. Schematic picture of the AFM probe

One end of the cantilever is firmly fixed on the silicon base - the holder, and the tip is located on the free cantilever end. The curvature radius of AFM tip apex is of the order of $1 \div 50$ nanometers depending on the type and on the technology of manufacturing. The angle near the tip apex is $10 \div 20º$. The interaction force F of a tip with the surface can be estimated from the Hooke law:

$$F = k \cdot \Delta Z \;,$$

where k is the cantilever elastic constant; ΔZ is the tip displacement corresponding to the bending produced by the interaction with the surface. The k values vary in the range $10^{-3} \div 10$ N/m depending on the cantilever material and geometry. The cantilever resonant frequency is important during AFM operation in oscillating modes. Self frequencies of cantilever oscillations are determined by the following formula (see, for example, [34]):

$$\omega_{ri} = \frac{\lambda_i}{l^2} \sqrt{\frac{EJ}{\rho S}} \;, \tag{3}$$

where l is the cantilever length; E the Young's modulus; J the inertia moment of the cantilever cross-section; ρ the material density; S the cross section; λ_i a numerical coefficient (in the range $1 \div 100$), depending on the oscillations mode.

$$\lambda_1 = 3,52 \qquad \lambda_2 = 22,04 \qquad \lambda_3 = 61,7$$
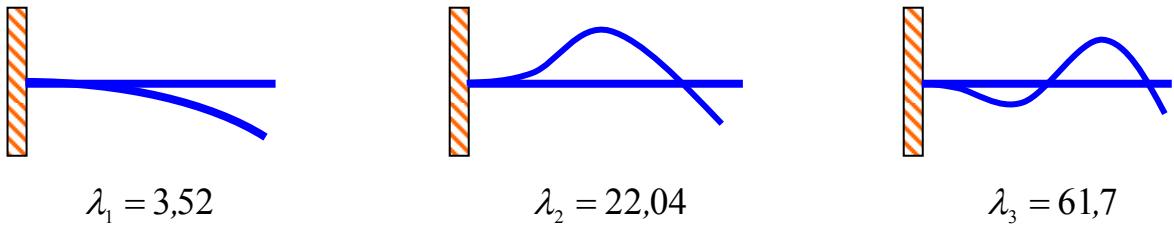
Fig. 66. Main cantilever oscillations modes

Frequencies of the main modes are usually in the $10 \div 1000$ kHz range. The quality factor Q of cantilevers mainly depends on the media in which they operate. Typical values of Q in vacuum are $10^3 - 10^4$. In air the quality factor drops to $300 - 500$, and in a liquid it falls down to $10 - 100$.

Basically, two types of probes are used in AFM –cantilever shaped as a beam of rectangular section and triangular cantilever, formed by two beams. A schematic picture of rectangular cantilever is presented in Fig. 67.
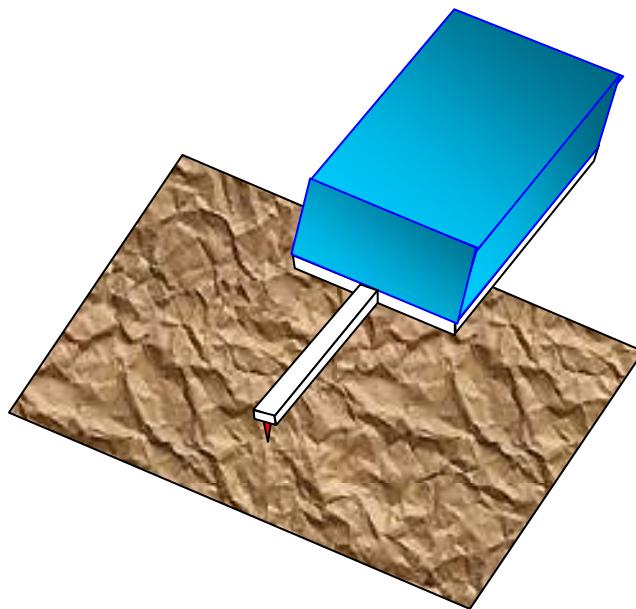
Fig. 67. A cantilever with rectangular section

Electron microscope images of commercial cantilevers with rectangular cross section (NSG - 11 probes produced by NT-MDT Company) are shown in Fig. 68.
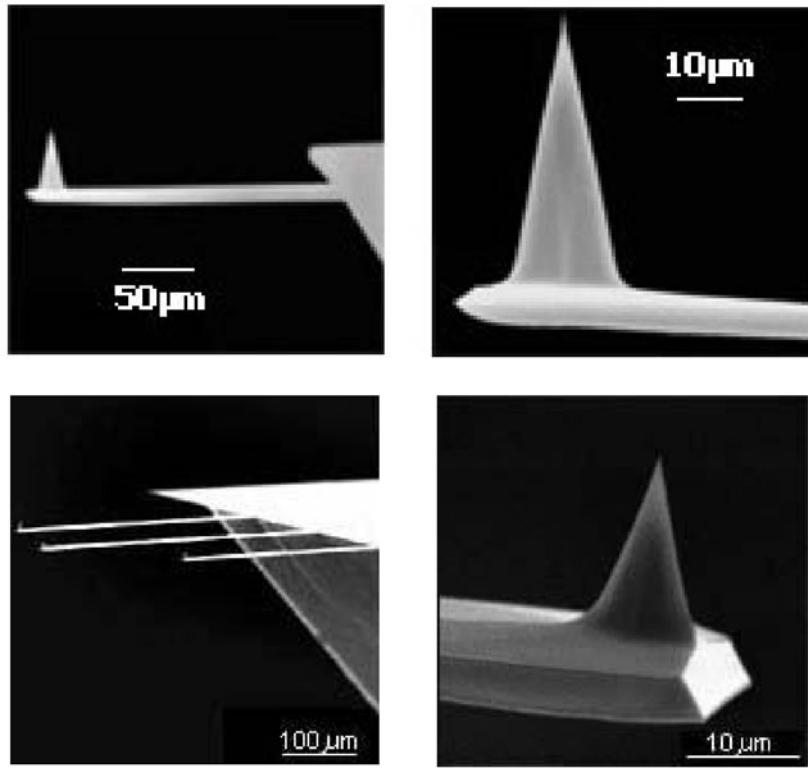
Fig. 68. SEM images of AFM tips on rectangular cantilevers [54]

Sometimes the AFM probes have few cantilevers of various length (hence, of various stiffness as well) on one base. In this case the working cantilever is selected by corresponding alignment of the AFM optical system.

Probes with triangular cantilever have higher stiffness and, hence, higher resonant frequencies. They are usually used in oscillating AFM techniques. A schematic picture of triangular cantilevers is shown in Fig. 69 and SEM images in Fig. 70.
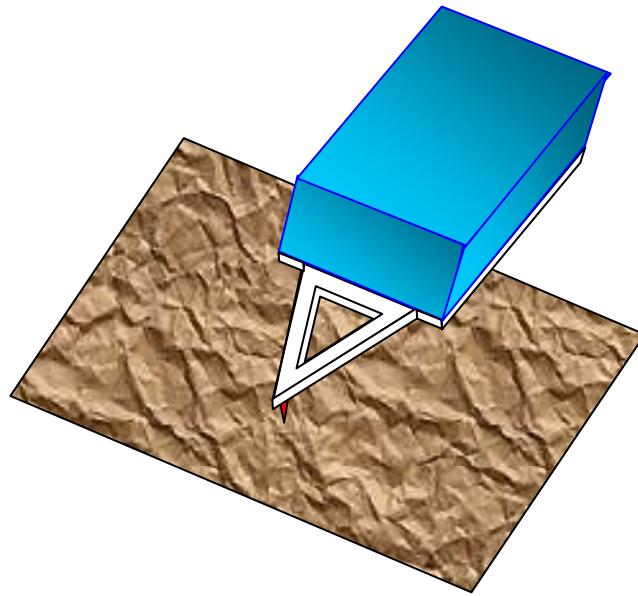
Fig. 69. Schematic picture of triangular cantilever
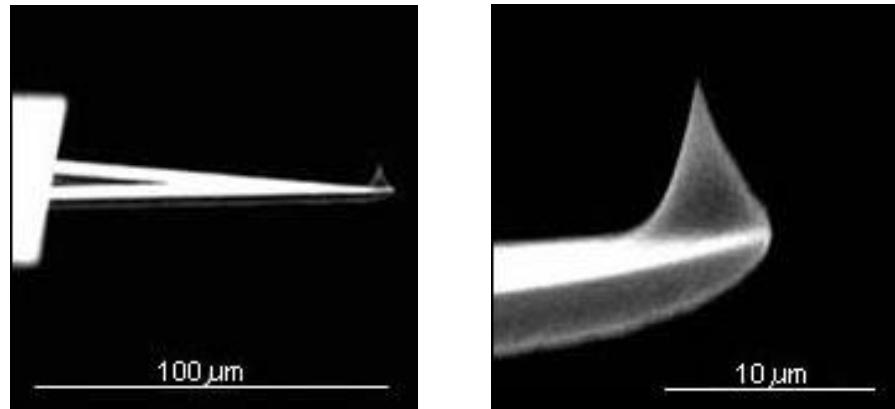
Fig. 70. SEM images of AFM tip on a triangular cantilever [54].

Manufacturing of AFM probes is a complex technological process including photolithography, ion-implantation, chemical and plasma etching operations. The basic stages of one of possible probe manufacturing techniques are presented in Fig. 71.

The AFM probe manufacturing techniques
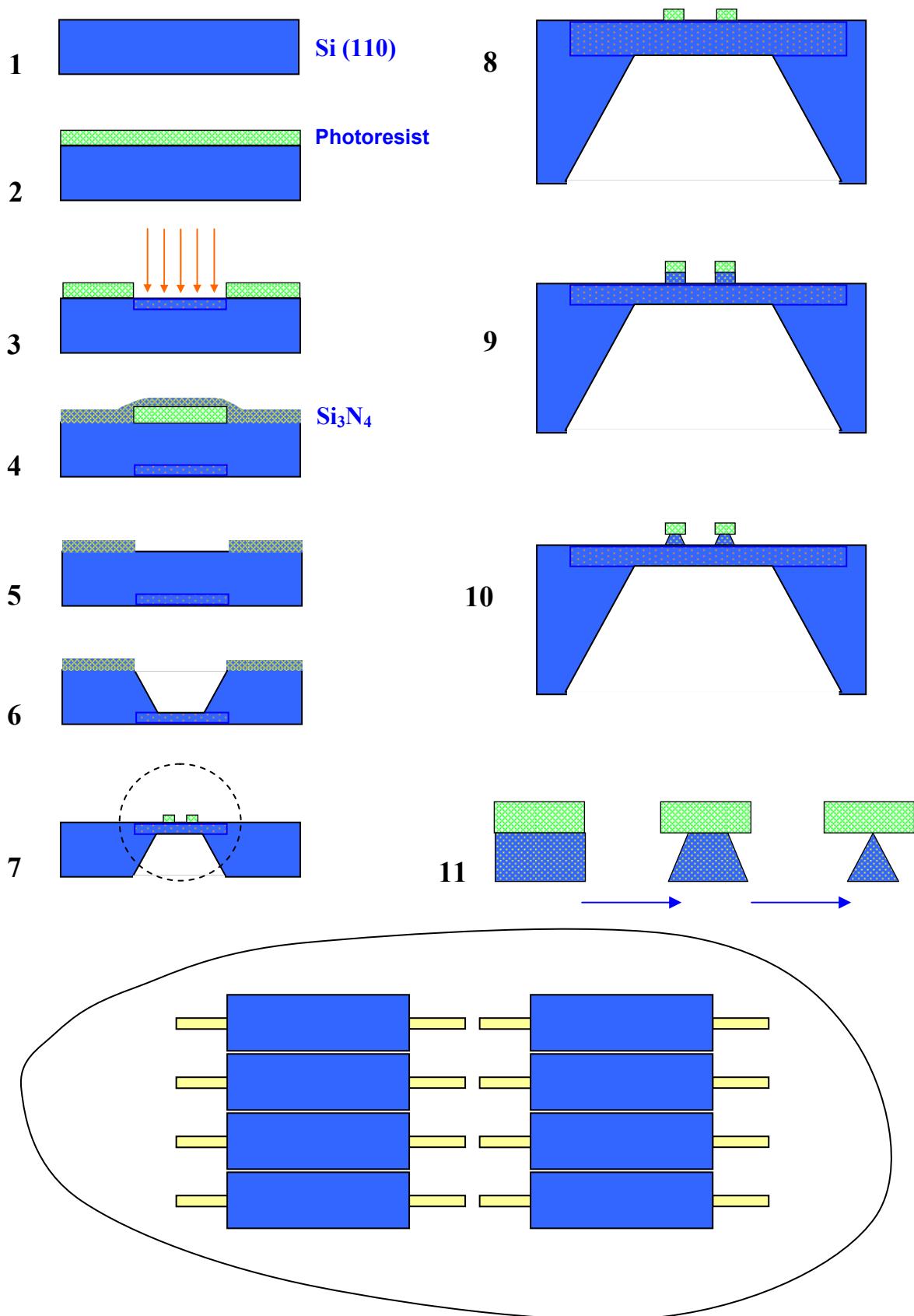
Fig. 71. Basic stages of the probe manufacturing process

Wafer of single crystal silicon (110) are used for probe manufacturing. A thin photoresist layer (Fig. 71, stage 2) is deposited on the wafer surface. Then photoresist is exposed through a photo mask, and a part of photoresist is removed by means of chemical etching. After that ions of boron are implanted to a depth of about 10 microns into the silicon area, unprotected by photoresist (stage 3). The photoresist is further washed off in a special etching agent, and then the wafer is thermally annealed, resulting in atoms of boron diffusing into the silicon crystal lattice. The silicon alloyed by boron, forms a so-called stop-layer which blocks the process of etching for some selective etching agents. Then on the reverse side of the wafer the photolithography is done again, as a result of which the photoresist layer is formed exactly above the area implanted by boron. After that the wafer is covered by a thin Si_3N_4 layer (stage 4). Then the photoresist is selectively etched, and during dissolution photoresist bloats and strips off the thin Si_3N_4 film located directly above it (stage 5). The silicon plate is etched through to the stop-layer by the selective etching agent, which reacts with silicon and does not react with alloyed silicon and Si_3N_4 layer, (stage 6). After that Si_3N_4 is washed off, and photoresist islands are formed on the reverse side of the wafer in the alloyed area by a photolithography method (stages 7,8). Then the silicon is etched, resulting in formation of columns of silicon under photoresist islands (stage 9). After that needles are formed with the help of plasma etching from silicon columns (stages 10,11). Cantilevers from the reverse side (with respect to the apex) are covered with a thin layer of metal (Al, Au) to improve the reflective properties. As a result of these operations a set of hundreds probes is made on one silicon wafer. For electric measurements the conducting coatings from various materials (Au, Pt, Cr, W, Mo, Ti, W_2C, etc.) are applied on a tip. Tips in magnetic AFM probes are covered with thin layers of ferromagnetic materials, such as Co, Fe, CoCr, FeCr, CoPt, etc.

The contact mode in atomic force microscopy

The methods used in AFM to acquire images (either topographic or related to local sample properties) can be split in two groups : the *contact modes* (quasi-static) and the *non-contact modes* (oscillatory).

In contact mode the tip apex is in direct contact with the surface, and the force (attractive or repulsive) acting between the atoms of tip and sample is counterbalanced by the elastic force produced by the deflected cantilever. Cantilevers used in contact-mode have relatively small stiffness, allowing to provide high sensitivity and to avoid undesirable excessive influence of the tip on the sample.

The contact mode may be carried out either at *constant force* or at *constant average distance* (between probe and sample). During scanning in constant force mode the feedback system provides a constant value of the cantilever bend, and consequently, of the interaction force as well (Fig. 72). Thus the control voltage in the feedback loop, applied to the Z-electrode of the scanner, will be proportional to the sample surface topography.

Scanning at constant average distance between the tip and the sample (Z = *const*) is frequently used on samples with small roughness (a few Angstrom). In this mode (also named *constant height mode*) the probe moves at some average height Z_{av} above the sample (Fig. 73) and the cantilever bend ΔZ, proportional to the applied force, is recorded in every point. The AFM image in this case describes the spatial distribution of the interaction force.
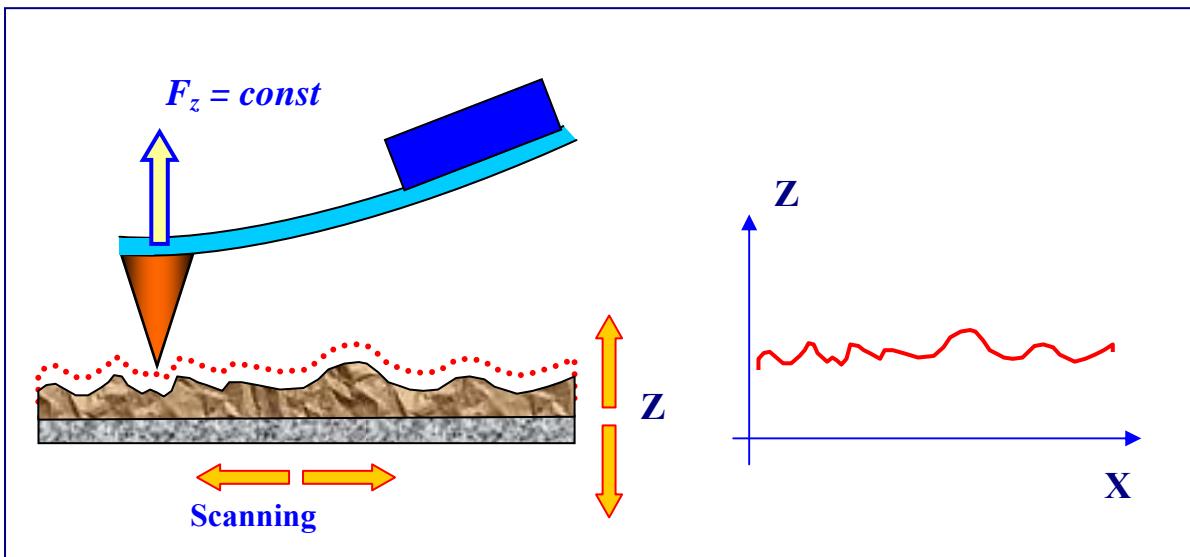
Fig. 72. AFM image acquisition at constant force
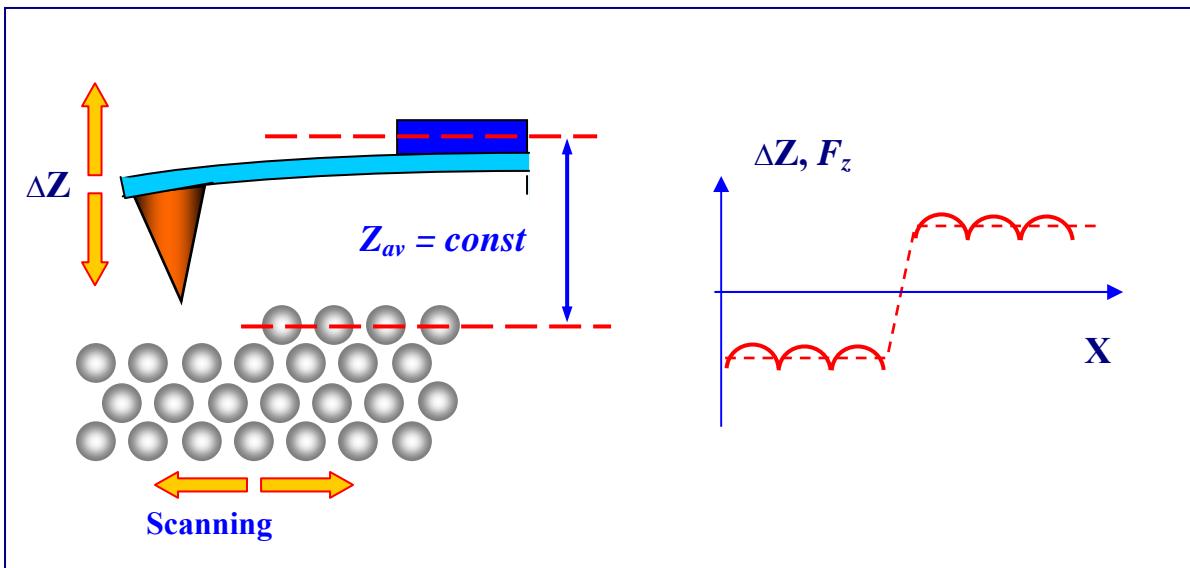
Fig. 73. AFM image acquisition at constant average distance (constant height)

A drawback of contact modes is the direct mechanical interaction of the tip with the sample. It frequently results in tips breakage and/or sample surface damages. Contact techniques are practically not suitable for soft samples such as organic and biological materials.

Dependence of the force on the probe-sample distance

With the help of the atomic force microscope it is possible to study detailed features of the local force interaction, yielding information on the sample surface properties. With this purpose the so-called *force-distance curves* (tip approaching to, or retracting from the surface) are measured. Actually these are the dependences of the cantilever bending ΔZ (and consequently, of the interaction force) on the coordinate z, i.e on the probe-sample distance. A typical $\Delta Z = f(z)$ curve is shown in Fig. 74.
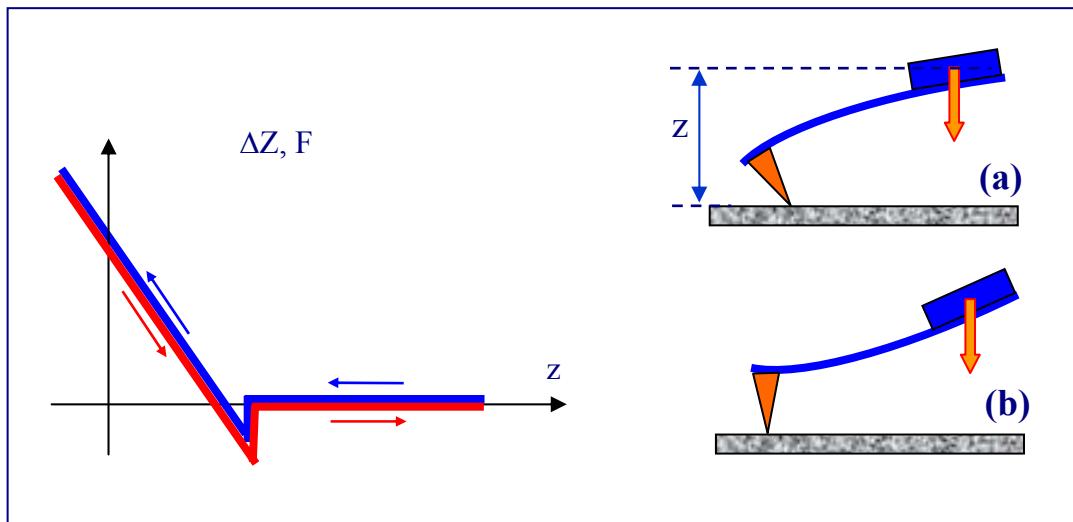
Fig. 74. Schematic picture of the cantilever deflection ΔZ (proportional to the applied force F) versus the probe-sample distance z. Blue: approaching. Red: retracting

During approach to the surface the tip gets in the reach of attractive forces. This causes a cantilever bend toward the surface (Fig. 74, insert (a)). The jump of the tip to the surface is due to the large gradient of the attractive force near the sample surface. For a Lennard-Jones type potential the range Z* of the attractive force, where the gradient $F_z^{'}$ is high, is about 1 nanometer. The behavior of the Lennard-Jones force and its derivative with respect to the tip-surface distance is schematically shown in Fig. 75.
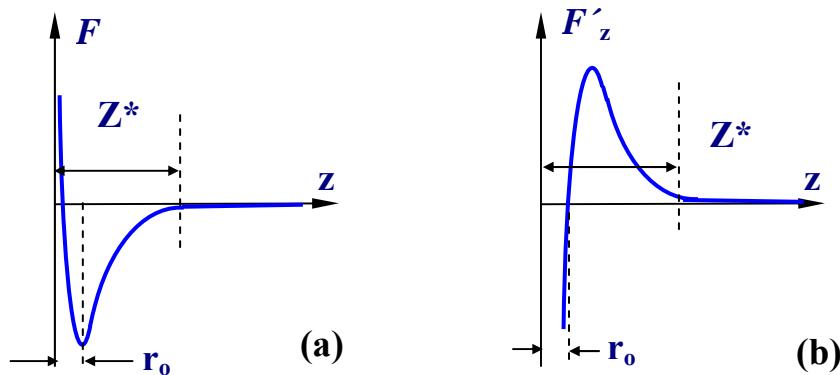
Fig. 75. Schematic picture of the force (a) and of the force gradient (b) as functions of the tip-surface distance z.

The jump of the tip to the surface may be observed only when the cantilever elastic constant is smaller than the maximum force gradient. This can be explained by considering the motion equation of an elastic cantilever near the surface:

$$m\ddot{z}_1 = -kz_1 + F(d + z_1),$$

where d is the tip-surface distance at equilibrium and z_1 the displacement from the equilibrium position, $F(z)$ the tip-surface interaction force, k and m are the cantilever elastic constant and mass.

Using a linear approximation of the function $F(z)$ we get:

$$F = F(d) + F'_z(d) \cdot z_1$$

$$m z''_1 + \left[k - F'_z(d) \right] z_1 = F(d).$$

With the substitution, $z_2 = z_1 - \dfrac{F(d)}{k - F'_z(d)}$, the motion equation takes the form:

$$z''_2 + \omega_0^2 z_2 = 0, \qquad \omega_0^2 = \frac{k - F'_z(d)}{m}.$$

In this form it becomes apparent that the oscillator frequency ω_0 depends on the distance d. If the force gradient at any distance is larger than the cantilever elastic constant, then $\omega_0^2 < 0$. This condition corresponds to the unstable equilibrium position of an inverted pendulum. Any small disturbance results in loss of stability, and the cantilever moves to the surface.

During further approach of the probe to the sample, the tip starts to experience a repulsive force, and the cantilever bends in the opposite direction (Fig. 74, insert (b)). The slope of the curve $\Delta Z = f(z)$ in this region is determined by the elastic properties of both sample and cantilever. If interaction is perfectly elastic, the dependence of the bend on the distance, recorded during reverse motion, coincides with the dependence obtained during forward motion (Fig. 74). For soft (plastic) samples, such as films of organic materials, biological structures, etc., and also for samples with adsorbed layers of various materials, the shape of the $\Delta Z = f(z)$ curves is more complex. In this case the shape of the curve is strongly influenced by the capillary and plasticity effects. As an example, approach-retraction curves for a sample coated by a layer of a liquid are schematically shown in Fig. 76, where the hysteresis due to capillary effect is apparent. During probe approach to the sample the tip is wetted by the liquid (at the "snap-on" distance z_1), and a meniscus is formed. The tip, submerged in the liquid, is affected by an additional force of surface tension. During retraction the tip-liquid separation occurs at a larger distance ("snap-off" distance $z_2 > z_1$).
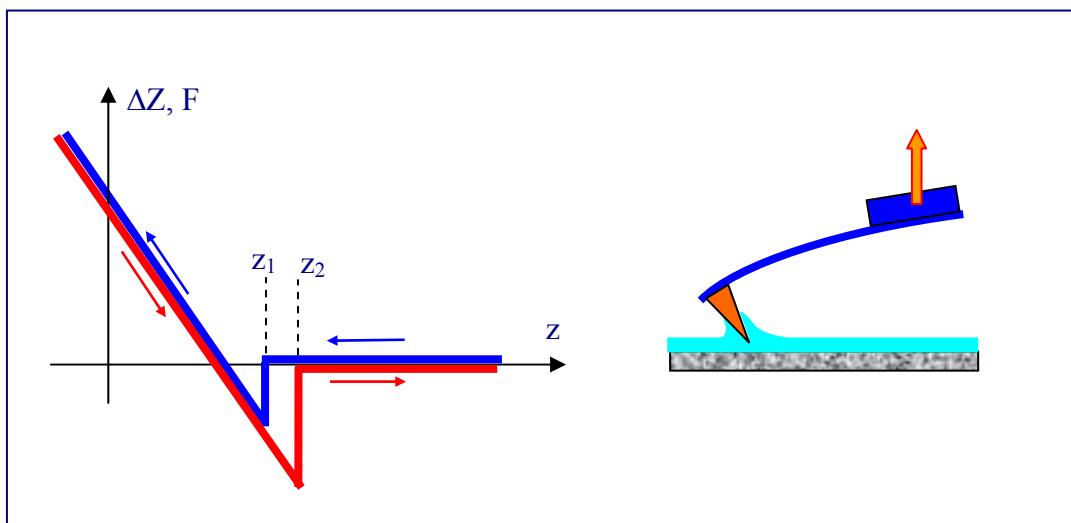
**Fig. 76. Schematic picture of the cantilever deflection ΔZ (proportional to the applied force F) versus the probe-sample distance z , on a sample with an adsorbed liquid layer**

Thus, by the shape of the $\Delta Z = f(z)$ curve it is possible to obtain information on the tip-surface interaction, to study the local stiffness of the sample and the distribution of the adhesion forces.

AFM control system in the contact mode

The simplified circuit of the AFM control system during cantilever operation in the contact mode is presented in Fig. 77. The control system consists of a digital part implemented by a personal computer, and an analog part, usually a stand-alone block. The digital part contains, basically, digital-to-analog (DAC) and analog-to-digital (ADC) converters. Two-channel digital-to-analog converters DAC-X and DAC-Y provide the sample raster-scanning. The feedback loop consists of the preamplifier PA structurally located in the AFM measuring head, a differential amplifier (DA), high-voltage amplifier A2 and a piezo-transducer, regulating the bend value of a cantilever, and consequently, the tip-surface interaction force. In the initial state the analog switch SW 1 is closed, and SW2 is open.
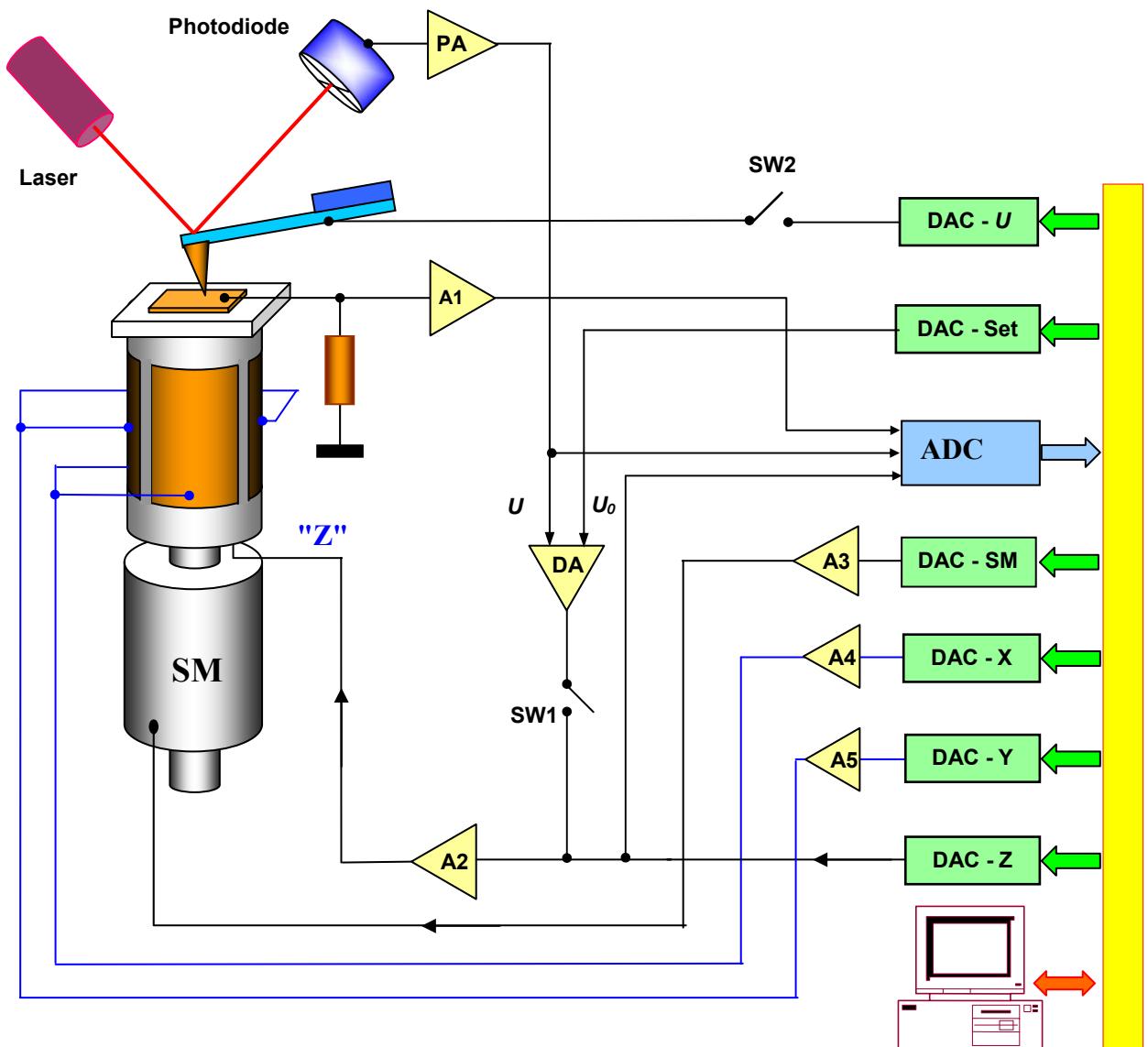
Fig. 77. Simplified circuit of the control system during operation in the contact mode

At first the operator aligns the optical system, focusing the laser spot onto the cantilever and maximizing the photodiode total current, while minimizing the difference between the opposite photodiode sectors. Then, a voltage U_0, proportional to the working value of the cantilever deflection ΔZ (which will be kept constant by the feedback system) is established by means of the DAC-Set. After that the procedure for tip-sample approach is switched on: a control voltage from DAC-SM is supplied to the stepping motor (SM). In the initial state the voltage in the feedback loop (proportional to the difference of currents between the photodiode vertical sectors) is smaller than the value established by the DAC-Set, and the scanner is extended as much as possible in the direction of the tip. During approach the cantilever is bent, the differential photodiode current increases, and the system of approach passes to the procedure for optimizing the scanner dynamic range. There is a further movement of the sample toward the tip provided by the stepping motor and a simultaneous retracting of the sample provided by the scanner (while the feedback keeps the cantilever bend constant) until the sample surface plane sets in the position corresponding to the middle of the dynamic range of the scanner. After that the microscope is ready for operation.

Scanning of a sample is performed by feeding a saw tooth voltage to the external electrodes of the tubular scanner through two-channel DAC-X and DAC-Y converters and two-channel high-voltage A4, A5 amplifiers. During the sample scanning, the value of the photodiode differential current selected by the operator (corresponding to a certain value of the cantilever bend) is kept constant. In the constant force mode (F_z = const) the voltage fed to the Z-electrode of the scanner is proportional to the surface topography. This happens as follows. The real time value of the voltage U, proportional to the differential photodiode current, is compared by the differential amplifier (DA) with the value U_0, set by the operator. The differential voltage (also named "error signal", $\Delta U = U - U_0$) is amplified (by A2) and supplied to the internal Z-electrode of the scanner. The scanner extends or retracts (with respect to the actual position set by the DAC-Z), depending on the sign of the signal ΔU, until ΔU becomes (practically) zero. Thus, during scanning the voltage applied to the Z-electrode of the scanner is proportional to the z-shift executed by the scanner in order to keep constant the tip-surface distance, i.e. to the surface modulation in the z-direction . The output signal of the differential amplifier is recorded by ADC as information on the surface topography.

It is possible to measure, in a selected point of the sample, the dependence of the cantilever deflection on the probe-surface distance: $\Delta Z = f(z)$. For this purpose the feedback is interrupted by the analog switch SW1, and a saw tooth voltage is applied to the Z-electrode of the scanner from the DAC-Z. Synchronously the ADC records the output voltage of the preamplifier PA, which is proportional to the cantilever deflection and consequently, to the tip-surface interaction force. The acquired data are transformed into a $\Delta Z = f(z)$ curve, which can be plotted on the computer display.

Acquisition of the AFM image in the constant average distance mode (also named *constant height* mode) is done in the following way. In the beginning the $\Delta Z = f(z)$ dependence is measured and a (small) distance of the tip above the surface is chosen. Then the feedback is broken, and the sample is scanned. The preamplifier output voltage, proportional to the cantilever deflection, is recorded as information of the force distribution $F(x,y)$ along the sample surface. For samples with small roughness the "constant height" image gives information similar to the "constant force" image.

Registration of volt-ampere characteristics of a tunneling tip-sample contact in a selected point of a surface is possible using cantilevers with a conducting coating. The SW2 switch is closed to obtain the VAC, and a saw tooth voltage from the *DAC-U* is applied to the cantilever. Synchronously the voltage, proportional to the current through the contact, is amplified (by A1), recorded by the ADC in the computer memory and plotted on the computer display.

The drawback of AFM contact techniques is the direct mechanical interaction of the tip with the surface. It frequently results in breakage of tips and damage of the samples surface. Contact techniques are therefore not appropriate for analysis of soft samples (organic materials or biological objects). Soft samples are more successfully studied using an oscillating cantilever. Oscillatory techniques strongly reduce the mechanical influence of the tip on the surface during scanning. Besides that, development of oscillatory techniques has essentially expanded the variety of surface properties that can be investigated with AFM.

Forced oscillations of a cantilever

The exact description of the AFM cantilever oscillations is a complex mathematical task. However, the basic features of the processes occurring during interaction of an oscillating cantilever with a surface can be understood on the basis of elementary models, in particular, using the approximation of a localized mass model [3]. Let us approximate the cantilever as an elastic massless beam (with elastic constant k), fixed at one end on the piezo-vibrator PV, plus a mass m localized on the other end (Fig. 78).
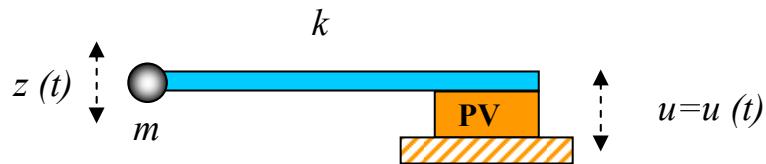
Fig. 78. Probe model as an elastic cantilever with a mass at one end

Let the piezo-vibrator oscillate with frequency ω:

$$u = u_0 \, cos(\omega t).$$

Then the motion equation of the system is,

$$m\ddot{z} = -k(z-u) - \gamma\dot{z} + F_0, \qquad\qquad (4)$$

where the term $\gamma\dot{z}$, proportional to the first derivative, takes into account the viscous force in air, and F_0 takes into account the gravity force and other possible constant forces. A constant force only displaces the equilibrium position of the system and does not influence the frequency, the amplitude and the phase of the oscillation. Therefore, with the variable substitution:

$$z = z_1 + F_0 / k,$$

the motion equation for the displacement z_1 from the equilibrium position takes the form:

$$m\ddot{z}_1 + \gamma\dot{z}_1 + kz_1 = ku_0 \, cos(\omega t).$$

With the definition $\omega_0 = \sqrt{k/m}$, and introducing the quality factor of the system $Q = \omega_0 m / \gamma$, we obtain:

$$\ddot{z}_1 + \frac{\omega_0}{Q}\dot{z}_1 + \omega_0^2 z_1 = \omega_0^2 u_0 \cos(\omega t). \tag{5}$$

The simplest solution is found in the domain of complex numbers η, by writing the equation in the form:

$$\ddot{\eta} + \frac{\omega_0}{Q}\dot{\eta} + \omega_0^2 \eta = \omega_0^2 u_0 e^{-i\omega t}.$$

where i is the imaginary unit.

The general solution is the superposition of dumped oscillations with decrement $\delta = \omega_0 / 2Q$ and persistent forced oscillations with frequency ω. Let us find the steady-state oscillations. We search for a solution in the form

$$\eta = a \cdot e^{-i\omega t}.$$

Substituting (5) in the equation (4), we obtain for the complex amplitude a:

$$a = \frac{\omega_0^2 u_0}{\omega_0^2 - \omega^2 - i\dfrac{\omega\omega_0}{Q}}.$$

The module of a is the forced oscillations amplitude $A(\omega)$:

$$A(\omega) = \frac{u_0 \omega_0^2}{\sqrt{(\omega_0^2 - \omega^2)^2 + \dfrac{\omega^2 \omega_0^2}{Q^2}}}. \tag{6}$$

The phase of the complex amplitude a is the phase difference $\varphi(\omega)$ between the system oscillation and the forcing term $u = u_o \cos(\omega t)$:

$$\varphi(\omega) = arctg\left[\frac{\omega\omega_0}{Q(\omega_0^2 - \omega^2)}\right]. \tag{7}$$

From expression (6) it follows, that the tip oscillation amplitude $A(\omega_0) = Q u_0$, at the frequency ω_0, is proportional to the quality factor. Besides that, presence of dissipation ($\gamma \neq 0$, i.e. $Q \neq \infty$) in the system results in a decrease of the resonant frequency of the cantilever oscillations. Indeed,

differentiating the radicand with respect to ω^2 in expression (6) and equating the derivative to zero, we obtain for the resonant frequency ω_{rd}:

$$\omega_{rd}^2 = \omega_0^2\left(1 - \frac{1}{2Q^2}\right).$$

The shift of the dissipative system resonant frequency is

$$\Delta\omega = \omega_0 - \omega_{rd} = \omega_0\left(1 - \sqrt{1 - \frac{1}{2Q^2}}\right).$$

Increasing dissipation, the amplitude-frequency characteristic of the system (response curve) is shifted to lower frequencies (Fig. 79).
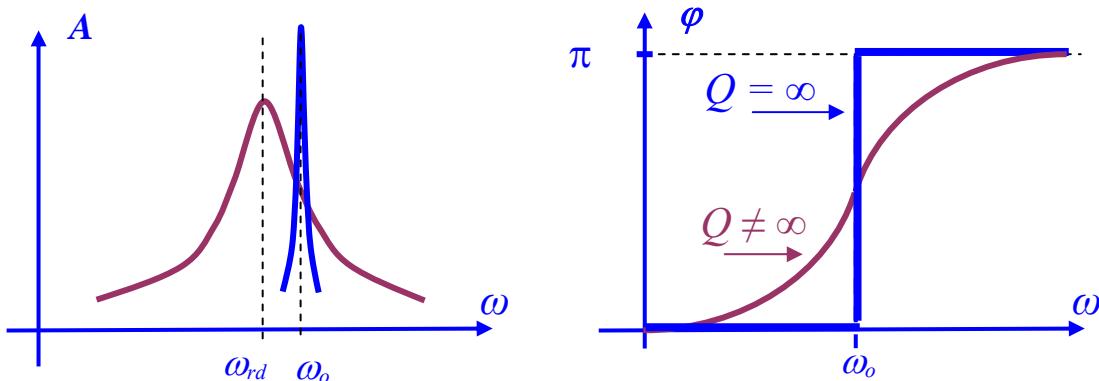
**Fig. 79. Change of the amplitude-frequency characteristic
and phase response in a system with dissipation.
Blue color shows characteristics of non-dissipative system.**

However, for typical values of quality factor of cantilevers in air, the resonant frequency shift due to dissipation is small. Influence of the dissipation amounts, basically, to essential reduction of the oscillations amplitude and to broadening of the amplitude and phase response curves of the system (Fig. 79).

Contactless mode of AFM cantilever oscillations

In a contactless mode the cantilever forced oscillations amplitude is small: about 1 nanometer. During tip to surface approach, the cantilever is affected by an additional force $F_{PS}(z)$ due to van der Waals interaction with the sample. For small oscillations of the cantilever around the distance z_0 from the surface, the force may be approximated by the first (linear) term in the series expansion:

69

$$F_{PS} = F_{PS0} + \frac{\partial F}{\partial z}(z_0) \cdot z(t) = F_{PS0} + F_z' \cdot z(t).$$

where F_z' is the gradient of the tip-surface interaction force at the distance z_0. Therefore an additional term must be included into the motion equation (4).

$$m\ddot{z} = -k(z - u) - \gamma \dot{z} + F_0 + F_{PS0} + F_z' z.$$

With the variables substitution: $z = z + (F_0 + F_{PS0})/k$, we come to the following equation:

$$m\ddot{z} + \gamma \dot{z} + (k - F_z') \cdot z = ku_0 \cos(\omega t).$$

I.e. presence of a force gradient results in a change of effective stiffness of the system:

$$k_{eff} = k - F_z'.$$

The motion equation (5) for the "free cantilever" oscillation (i.e. the cantilever at a distance from the surface that makes F_z' negligible) changes into:

$$\ddot{z} + \frac{\omega_0}{Q}\dot{z} + \left(\omega_0^2 - \frac{F_z'}{m}\right) \cdot z = \omega_0^2 u_0 \cos(\omega t).$$

Repeating the calculations carried out for the free cantilever, we get the amplitude-frequency characteristic for the cantilever in the force gradient F_z':

$$A(\omega) = \frac{u_0 \omega_0^2}{\sqrt{\left(\omega_0^2 - \omega^2 - F_z'/m\right)^2 + \omega^2 \omega_0^2 / Q^2}} \ . \tag{8}$$

And, accordingly, the phase response:

$$\varphi(\omega) = arctan\left[\frac{\omega \omega_0}{\left(\omega_0^2 - \omega_0 - F_z'/m\right)}\right]. \tag{9}$$

Thus, presence of a gradient in the tip-surface interaction force results in additional shift of the amplitude and phase response curves. The resonant frequency ω_{rf} in presence of external force can be written as

$$\omega_{rf}^2 = \omega_0^2\left(1 - \frac{1}{2Q^2} - \frac{F_z'}{k}\right) = \omega_{rd}^2 - \frac{F_z'}{m} \ .$$

Hence, additional shift of the amplitude-frequency characteristic is equal to

$$\Delta\omega = \omega_{rd} - \omega_{rd} = \omega_{rd}\left(1 - \sqrt{1 - \frac{F_z'}{m\omega_{rd}}}\right).$$
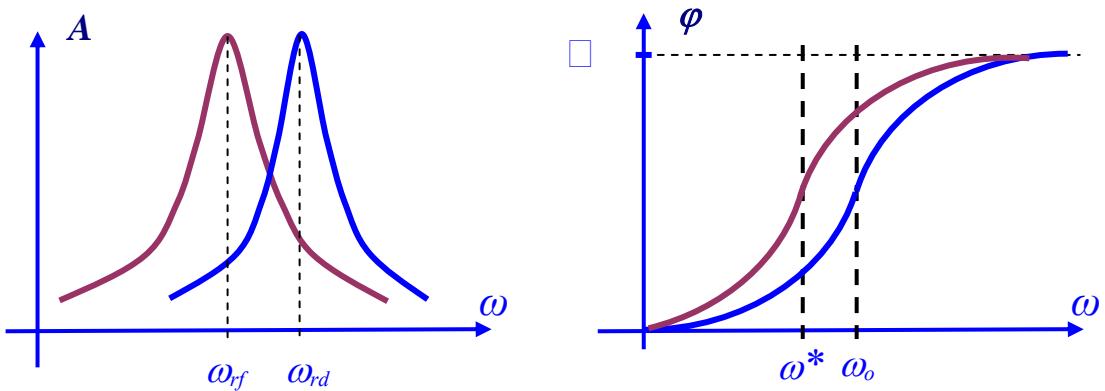
Fig. 80. Change of the amplitude-frequency characteristic and the phase response of a cantilever under influence of a force gradient.

From expression (9) it also follows, that the presence of a force gradient shifts the phase response curve so that the inflection point occurs at the frequency ω^*:

$$\omega^* = \omega_0 \sqrt{1 - \frac{F_z'}{k}} \qquad \text{And } \Delta\omega = \omega_0 - \omega^* = \omega_0 \left(1 - \sqrt{1 - \frac{F_z'}{k}}\right).$$

Let the cantilever perform forced "free" oscillations far from a surface with frequency ω_0, then the phase shift is π/2. During approach to the surface the phase (assuming $F_z' < k$) changes to

$$\varphi(\omega_0) = arctan\left[\frac{k}{QF_z'}\right] \approx \frac{\pi}{2} - \frac{QF_z'}{k}.$$

Hence, the additional phase shift in presence of a force gradient [35] will be equal to:

$$\Delta\varphi = \frac{\pi}{2} - \varphi(\omega_0) \cong \frac{QF_z'}{k}.$$

The phase shift is therefore proportional to the force gradient. This effect is used obtain the phase contrast AFM image.

"Semi-contact" mode of the AFM cantilever oscillations

In order to detect changes in the amplitude and in the phase of cantilever oscillations in non-contact mode high sensitivity and stability of the feedback is required. In practice the so-called "semi-contact mode" (also named "intermittent-contact mode" or "tapping mode") is used more frequently. In this technique the forced cantilever oscillations are excited near a resonance frequency with an amplitude about 10–100 nanometers. The cantilever is approached to the surface so that in the lower semioscillation the tip get in contact with the sample surface (this corresponds to the repulsive region in the force-distance diagram (Fig. 81)).
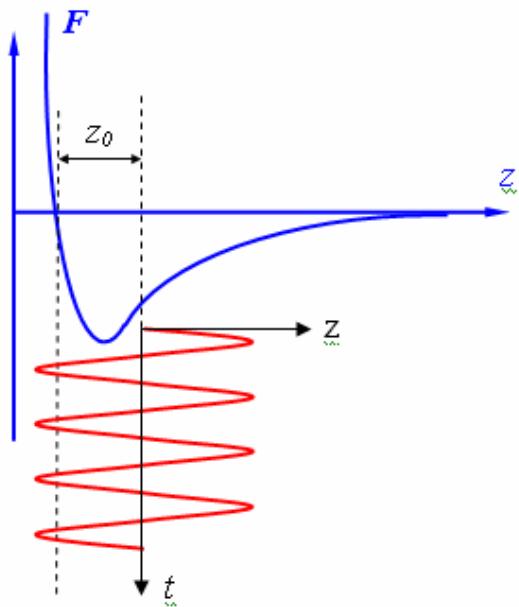
Fig. 81. Working point selection during "semi-contact" mode

During scanning, the changes of amplitude and phase of cantilever oscillations are recorded. The cantilever interaction with the surface in "semi-contact" mode consists in van der Waals forces plus the elastic force which is added during contact. If z_0 is the distance covered by the tip from the equilibrium position until contact with the surface, and $F_{PS}(z(t))$ is the combined force, then the motion equation of the cantilever is:

$$\ddot{z} + \frac{\omega_0}{Q}\dot{z} + \omega_0^2[z(t) - z_0 - u_0 \cos(\omega t)] = \frac{\omega_0^2}{k} F_{PS}[z(t)],$$

where the origin of z coordinate is at the surface. We shall notice, that the "semi-contact" mode is realized only when the z_0 distance is smaller than the amplitude of cantilever oscillations:

$$z_0 < Q u_0.$$

The theory of "semi-contact" mode is much more complex than the theory of contactless mode, since in this case the equation describing cantilever movement is essentially non-linear. The $F_{PS}(z(t))$ force now cannot be approximated by the first terms of a series expansion for small z values. However the characteristic features of this mode are similar to the features of a contactless mode - the amplitude and the phase of cantilever oscillations depend on the tip-surface interaction in the bottom part of cantilever oscillations. Since in the bottom part of oscillations the tip interacts mechanically with the surface, then in this mode the sample local stiffness has essential influence on the amplitude and phase changes.

The phase shift between the piezoelectric vibrator driving signal and the stationary cantilever oscillation can be estimated by considering the energy dissipation process during tip-sample interaction [36-38]. In stationary oscillations the energy entering the system is exactly equal to the

energy dissipated by the system. The energy E_{EX} supplied by piezo-vibrator during one oscillation period is equal to:

$$E_{EX} = \int_{t}^{t+2\pi/\omega} ku_0 cos(\omega t) \cdot \frac{dz}{dt} dt.$$

This energy is spent compensate the losses due to interaction of the cantilever with the atmosphere and with the sample. The energy E_{PA}, dissipated in the atmosphere during one period, is:

$$E_{PA} = \int_{t}^{t+2\pi/\omega} \frac{m\omega_0}{Q}\left(\frac{dz}{dt}\right)^2 dt.$$

The E_{PS} energy spent to compensate the losses during dissipative tip-sample interaction, is:

$$E_{PS} = \int_{t}^{t+2\pi/\omega} F_{PS}(z)\frac{dz}{dt} dt.$$

From the equilibrium condition it follows that:

$$E_{EX} = E_{PA} + E_{PS}.$$

Assuming stationary oscillations $z = A \cdot cos(\omega t + \varphi)$, we get:

$$E_{PS} = E_{EX} - E_{PA} = \frac{\pi ku_0 A}{Q}sin(\varphi) - \frac{\pi k\omega A^2}{\omega_0 Q}.$$

Therefore, the phase shift can be obtained from the following equation:

$$sin\,\varphi = \frac{\omega A}{\omega_0 u_0} + \frac{QE_{PS}}{\pi ku_0 A}.$$

Thus, the cantilever oscillations phase shift in "semi-contact mode" is determined by the amount of dissipative tip-sample interaction.

Formation of the AFM image in "semi-contact mode" is done as follows. The piezo-vibrator drives the cantilever oscillations at frequency ω (close to a resonant frequency) and with amplitude A_ω. During scanning the AFM feedback system keeps the oscillations amplitude constant at the A_0 level, set by the operator ($A_0 < A_\omega$). The voltage in the feedback loop (fed to the Z-electrode of the scanner) is recorded in the computer memory as topographic AFM image of the sample. Simultaneously, the change of the cantilever oscillation phase is also recorded as "phase contrast image". As an example, the topographic and the "phase contrast" AFM images of a polythene film, obtained in "semi-contact" mode [54] are presented in Fig. 82.
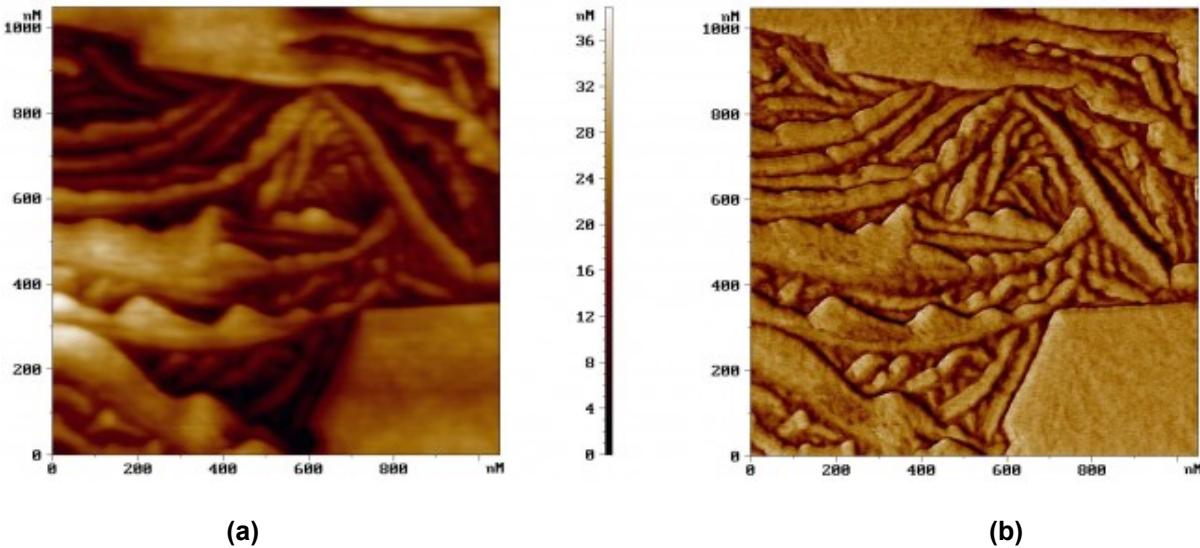
Fig. 82. AFM images of a polythene film area surface, obtained in a "semi-contact" ("tapping") mode
(a) - surface topography obtained in constant amplitude mode;
(b) - corresponding distribution of phase contrast

2.3. Electric force microscopy

In EFM the electric tip-sample interaction is used to collect information on the sample properties. Let us consider a system consisting of a probe, made of cantilever and tip with conducting coating, and a sample made of a thin layer of a material on a well conducting substrate.
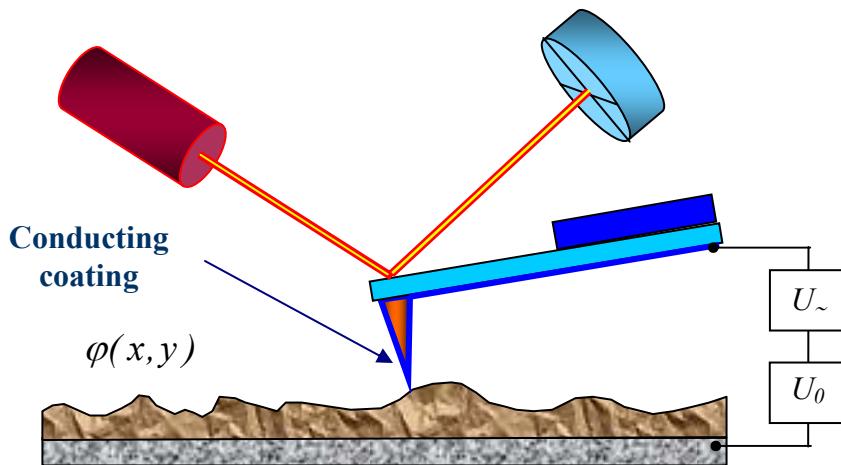
Fig. 83. Measurement circuit of the electric tip-sample interaction

Let the constant voltage U_0 and the variable voltage $U_\sim = U_1 \cdot sin\ (\omega t)$ be applied between the tip and the sample. If the thin layer on the substrate is a semiconductor or a dielectric the surface charge produces a potential distribution $\varphi\ (x,y)$ on the sample surface. The voltage between the tip and the sample surface is:

$$U = U_0 + U_1 \cdot sin(\omega t) - \varphi(x,y)$$

and the tip-sample capacity C, under the bias voltage U, stores the energy:

$$E = \frac{CU^2}{2} .$$

Then electric force of tip-sample interaction is

$$\vec{F} = -grad(E) .$$

And the Z-component of the electric force acting on the tip is

$$F_z = -\frac{\partial E}{\partial z} = -\frac{1}{2}U^2 \frac{\partial C}{\partial z} = -\frac{1}{2}[U_0 - \varphi(x, y) + U_1 sin(\omega t)]^2 \frac{\partial C}{\partial z} .$$

that, remembering the identity $sin^2(\omega t) = [1 - cos(2\omega t)]/2$, can be written:

$$F_z = -\frac{1}{2}\left\{[U_0 - \varphi(x,y)]^2 + 2[U_0 - \varphi(x,y)]U_1 sin(\omega t) + \frac{1}{2}U_1^2[1 - cos(2\omega t)]\right\}\frac{\partial C}{\partial z}$$

From the last expression it follows, that the interaction force is the sum of three components:

$$F_{z(\omega=0)} = -\left\{\frac{1}{2}\left((U_0 - \varphi(x, y))^2 + \frac{1}{2}U_1^2\right)\right\}\frac{\partial C}{\partial z} \quad \text{constant component;}$$

$$F_{z(\omega)} = -\left\{(U_0 - \varphi(x, y)) \cdot U_1 sin(\omega t)\right\}\frac{\partial C}{\partial z} \quad \text{component at frequency } \omega;$$

$$F_{z(2\omega)} = \left\{\frac{1}{4}U_1^2 cos(2\omega t)\right\}\frac{\partial C}{\partial z} \quad \text{component at frequency } 2\omega .$$

A synchronous detection of the cantilever oscillation amplitude at frequency 2ω allows to map, on the sample surface, the quantity $C_z'(x, y)$, i.e. the derivative of the capacity with respect to the z-coordinate. This technique is named Scanning Capacitance Microscopy (SCM) [39]. With SCM it is possible to study local dielectric properties of subsurface layers of samples.

In order to reach high resolution in SCM the electric force must be essentially due to the interaction between the sample and the tip. The tip-sample force F_{PS} may be written, assuming the rough approximation of a simple flat condenser, as:

$$F_{PS} = -\frac{1}{2}U^2 \frac{\partial C}{\partial z} \cong -\frac{1}{2}\alpha U^2 \frac{\pi R^2}{h^2} ,$$

where α is a constant, R the curvature radius of the tip apex, h the tip-surface distance (or thickness of a dielectric film on a conducting substrate). On the other hand, assuming the same

approximation for the cantilever-sample capacity, the cantilever-sample electric force F_{CS} may be written:

$$F_{CS} = -\frac{1}{2}U^2\frac{\partial C}{\partial z} \cong -\frac{1}{2}\alpha U^2\frac{LW}{H^2} \; ,$$

where L and W are the cantilever length and width, and H is the cantilever-surface distance (defined by the sizes of the tip). In order to make $F_{PS} > F_{CS}$ the distance h must be quite small, i.e.:

$$h < \sqrt{\frac{\pi R^2 H^2}{LW}} \; .$$

For typical values of the probe parameters ($L \sim 100$ μm, $W \sim 30$ μm, $H \sim 30$ μm, $R \sim 10$ nm) we get the following limit value for h:

$h < 10$ nm.

Since the $\partial C/\partial z$ value depends on the tip-sample distance, a "two-pass technique" is used in SCM. The following procedure is performed in each scan line. During the first pass cantilever oscillations are excited by the piezo-vibrator with a frequency close to the resonant frequency ω_0 and the AMF topography is recorded in a "semi-contact" mode. Then the probe is retracted from the surface to the distance h, a variable voltage (at frequency $\omega = \omega_0$) is applied between the tip and the sample, and scanning is repeated (Fig. 84). During the second pass the probe moves above a surface with a trajectory repeating the sample topography. Since during scanning the distance h between the probe and the surface is constant, changes of cantilever oscillation amplitude at frequency 2ω will be due to the change of the tip-sample capacity (i.e. to the local change of the sample dielectric properties).
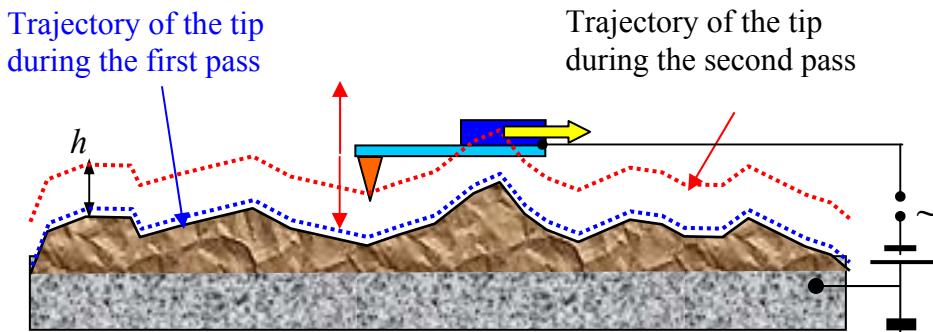

Fig. 84. EFM two-pass technique

Thus, the resulting EFM image is the two-dimensional function $C_z'(x,y)$ describing the local dielectric properties of the sample.

On the other hand the synchronous detection of the signal at frequency ω allows to study the distribution of the surface potential $\varphi(x,y)$ (the so-called "Kelvin probe microscopy" [40]).

Also the Kelvin probe microscopy is a "two-pass technique". Using a Voltage-Controlled-Voltage-Source, the voltage U_0 value is continuously adjusted in order to make the cantilever oscillation amplitude at frequency ω equal to zero. It occurs if $U_0(x,y)= \varphi(x,y)$ for each point (x,y) of the surface. The surface topography and the distribution of a surface potential for a composite film containing azobenzene [41] are presented as an example in Fig. 85. Molecules of azobenzene with a strong dipole moment are showing up on the image of surface potential.

(a)   **(b)**
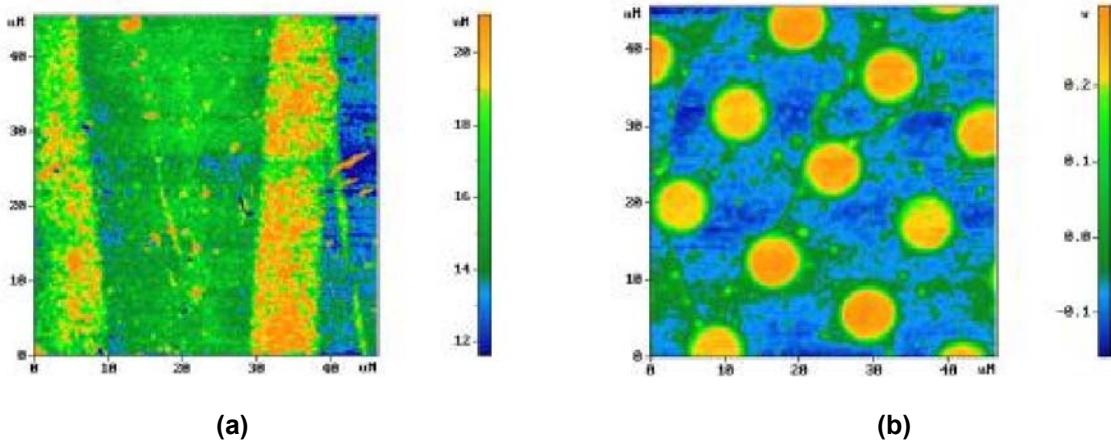
Fig. 85. Surface topography (a) and distribution of surface potential (b) of an azobenzene film

2.4. Magnetic force microscopy

Magnetic force microscope (MFM) [42,43] has been invented by Y. Martin and H.K.Wickramasinghe in 1987 for studying local magnetic properties. This device is an atomic force microscope using a tip covered by a layer of ferromagnetic material with specific $\vec{M}(\vec{r})$ magnetization.
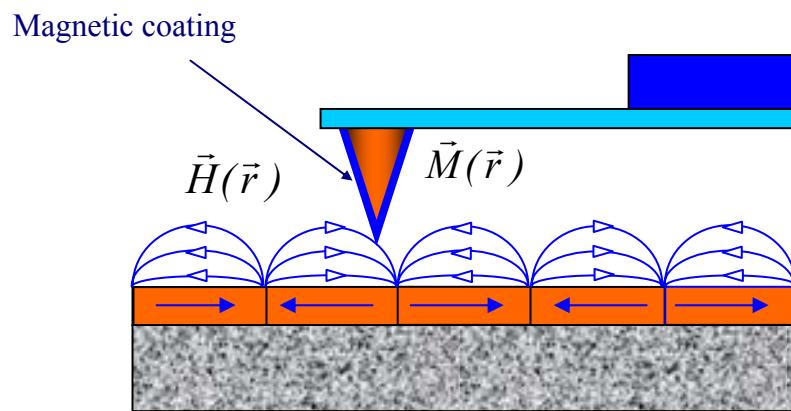
Fig. 86. The MFM tip in a magnetic field of a sample

The general description of the interaction of the MFM tip with the local magnetic field $\vec{H}(\vec{r})$ produced by a sample is a quite complex problem. We shall consider a simple model assuming the MFM tip as a single magnetic dipole described by the magnetic moment $\vec{m}$ [44]. Within this model the magnetic energy of the system is the scalar product of $\vec{m}$ and $\vec{H}$

$$w = -(\vec{m} \cdot \vec{H}).$$

The magnetic dipole in the $\vec{H}$ field is affected by the following force:

$$\vec{f} = -grad(w) = \vec{\nabla}(\vec{m} \cdot \vec{H})$$

and the moment of forces $\vec{N}$ is the vectorial product of $\vec{m}$ and $\vec{H}$

$$\vec{N} = [\vec{m} \times \vec{H}].$$

In a homogeneous magnetic field the force $\vec{f}$ is zero. In a non-uniform field the dipole is attracted to regions with larger intensity of the magnetic field $\vec{H}$.

Generally the magnetic moment of the MFM tip can be presented as a superposition of dipoles of the following form:

$$\vec{M}(\vec{r})dV,$$

where $\vec{M}$ is the specific magnetization of the tip coating and dV the elementary volume in the coating layer.
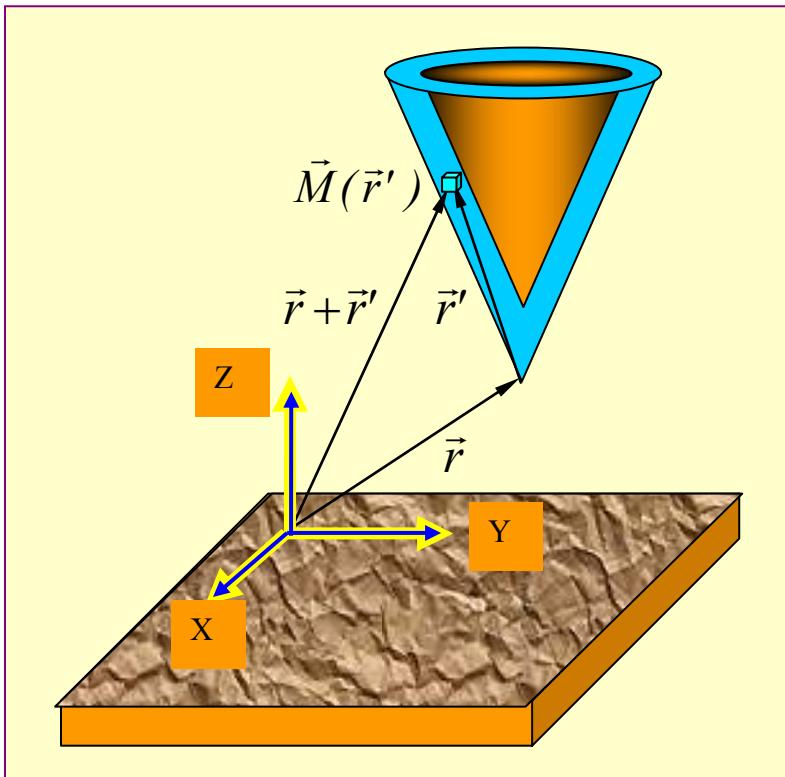

Fig. 87. Interaction of a MFM tip with the magnetic field of a sample

The total energy due to the tip-sample magnetic interaction is obtained by integrating over the magnetic layer of the tip). (see Fig. 87):

$$W_{layer} = -\int\limits_{V_{layer}} \vec{M}(\vec{r}\,') \cdot \vec{H}(\vec{r} + \vec{r}\,')dV'$$

The interaction force of the tip with the field of the sample is

$$\vec{F} = -grad\,(W_{layer}) = \int\limits_{V_{laer}} \vec{\nabla}(\vec{M} \cdot \vec{H})dV'\,.$$

Accordingly, the Z-component of the force is:

$$F_z = -\frac{\partial W_{layer}}{\partial z} = \int\limits_{V_{laer}} \left(M_x \frac{\partial H_x}{\partial z} + M_y \frac{\partial H_y}{\partial z} + M_z \frac{\partial H_z}{\partial z} \right)dV'\,.$$

In MFM the magnetic tip-sample interaction may be studied using either *static* technique or *oscillatory* technique.

The static MFM technique

In the static MFM technique, during scanning the tip moves above the sample at some $h=const$ distance. Thus the value of the cantilever bend, detected by the optical system, is recorded as MFM image $F\ (x,\ y)$, mapping the distribution of the magnetic tip-sample interaction force.

In order to perform the scanning at constant distance, a two-pass technique is used for samples with a considerable roughness. In each scanning line the following procedure is performed. On the first pass the AMF topographic image in contact or "semi-contact" mode is obtained. Then the tip is retracted from a surface to a distance h, and the scanning is repeated (Fig. 88). The value of the distance h must be large enough to make the van der Waals force smaller than the magnetic interaction force.
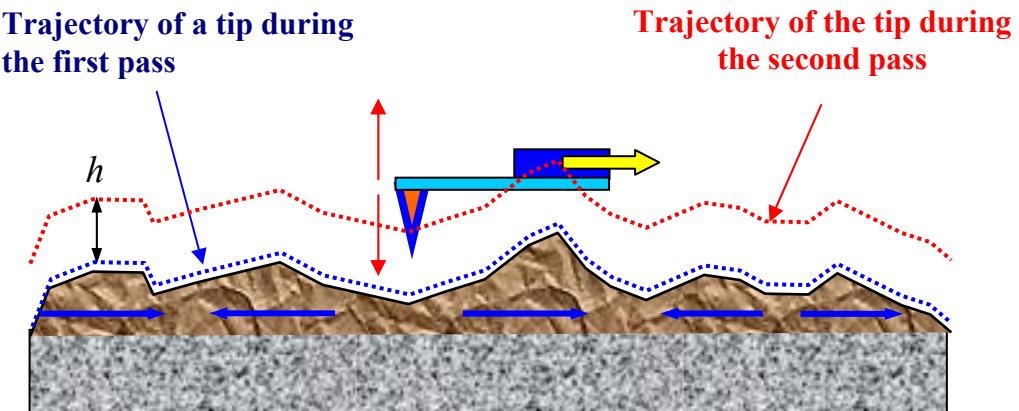
Fig. 88. Two-pass technique of the MFM acquisition

During the second pass the probe moves above a surface with a trajectory repeating the sample topography. Since the local distance between the tip and a surface in every point is constant, changes of the cantilever bend during scanning are due to the local heterogeneity of the magnetic forces. Thus, the final MFM image is a two-dimensional function $F(x,y)$, describing the distribution of tip-sample magnetic interaction.

Oscillatory MFM techniques

Application of oscillatory techniques in the magnetic force microscopy allows to implement high sensitivity (in comparison with static technique) and to produce better MFM images. As it has been shown in the section devoted to the contactless AFM technique, the presence of a force gradient results in resonant frequency changes, and consequently, in phase response shifts in the tip-sample system. These changes of the resonant properties are used to obtain information on the distribution of magnetization in the sample surface. The force gradient F_z in the case of magnetic interaction is:

$$F_z' = \frac{\partial F_z}{\partial z} = \int_{V_P} \vec{M}(\vec{r}') \frac{\partial^2}{\partial z^2} \vec{H}(\vec{r} + \vec{r}') dV' = \int_{V_P} \left(M_x \frac{\partial^2 H_x}{\partial z^2} + M_y \frac{\partial^2 H_y}{\partial z^2} + M_z \frac{\partial^2 H_z}{\partial z^2} \right) dV .$$

Also in the oscillatory MFM technique a two-pass technique is used. With the help of a piezo-vibrator cantilever oscillations are excited at a frequency ω close to resonance. During the first pass in "semi-contact" mode the surface topography is recorded. On the second pass the tip goes above the sample with a trajectory corresponding to the topography so that the average tip-surface distance is kept at a constant value h, defined by the operator. The MFM image is formed by recording the changes in the amplitude or in the phase of the cantilever oscillations.

The amplitude and phase of the cantilever oscillations can be approximated (provided that the changes in the force gradient F_z' along the surface are insignificant) as follows:

$$A(F_z') = A(F_{z0}') + A_{F_z'}'(F_z')\Big|_{F_{z0}'} \Delta F_z' ,$$

$$\varphi(F_z') = \varphi(F_{z0}') + \varphi_{F_z'}'(F_z')\Big|_{F_{z0}'} \Delta F_z' .$$

Then the changes of oscillation amplitude and phase shift, due to with variations of the force gradient, are:

$$\Delta A = A(F_z') - A(F_{z0}') = A_{F_z'}'(F_z')\Big|_{F_{z0}'} \Delta F_z' ,$$

$$\Delta \varphi = \varphi(F_z') - \varphi(F_{z0}') = \varphi_{F_z'}'(F_z')\Big|_{F_{z0}'} \Delta F_z' .$$
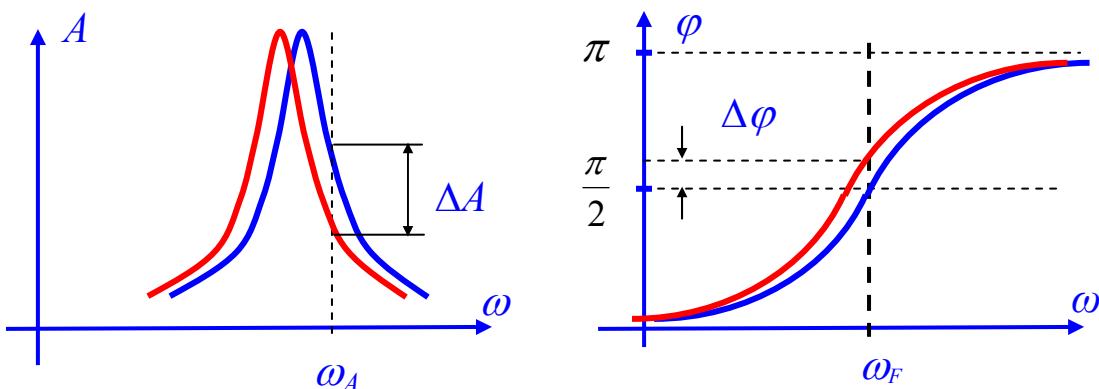

Fig. 89. Change of oscillation amplitude and phase at a change of a force gradient

The coefficients of $\Delta F'_z$ determine the sensitivity of the amplitude and phase measurement methods. The maximum sensitivity is achieved at the certain frequencies. For amplitude measurements this frequency is:

$$\omega_A = \omega_0 \sqrt{1 - F'_{z0} / k} \ (1 \pm \frac{1}{\sqrt{8Q}}),$$

Thus $A'_{F'_z}(\omega_A, F'_{z0}) = -\frac{8\sqrt{2}}{\sqrt{27}} \frac{Q^2}{k}.$

For phase measurements the maximum sensitivity is achieved, when the frequency of cantilever excitation coincides with the resonant frequency of the tip-sample system:

$$\omega_F = \omega_0 \sqrt{1 - F'_{z0} / k},$$

Thus $\varphi'_{F'_z}(\omega_F, F'_{z0}) = \frac{Q}{k}.$

The MFM images of the surface of a magnetic disk, acquired with the help of various techniques, are presented as an example on Fig. 90.
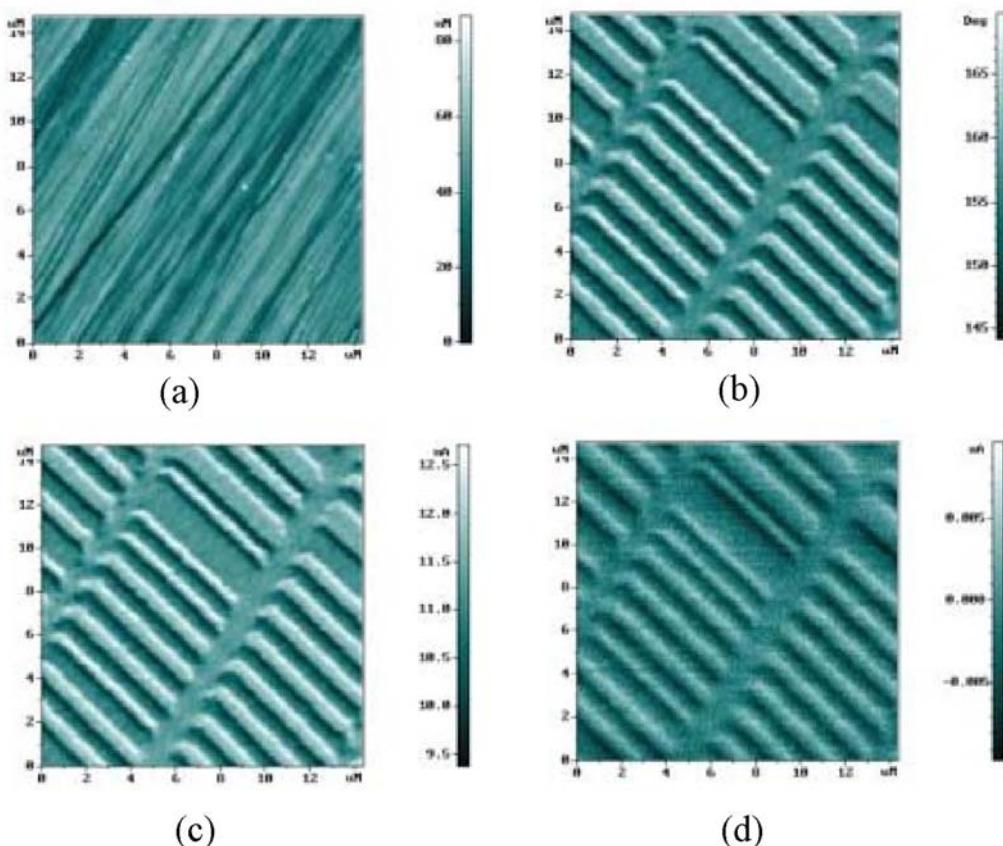

Fig. 90. MFM images of a magnetic disk surface:
(a) –AMF topography;
(b) – MFM phase contrast image;
(c) – MFM amplitude contrast image;
(d) – MFM image using static technique (magnetic force mapping)

Contrast in MFM images is connected, after all, to the magnetization distribution in the sample. The details on MFM images formation can be illustrated with the help of the approximation of a dipole-dipole interaction. In this case the magnetic sample is split into elementary volumes, whose magnetization is described by magnetic dipoles $\vec{m}_s^j$ (Fig. 91).
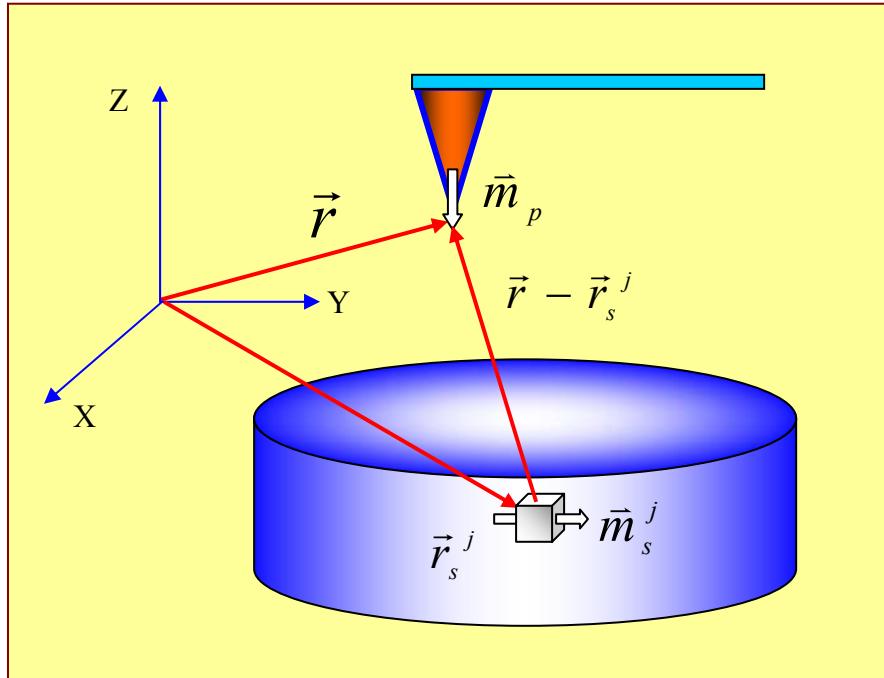
Fig. 91. Tip-sample interaction in a dipole approximation

The tip, in the simplest model, can be approximated as a single dipole $\vec{m}_p$. Then the Z-component of a force gradient may be described by the relation:

$$\frac{\partial}{\partial z} F_z(\vec{r}) = \sum_j \left[(\vec{m}_P \vec{\nabla}) \frac{\partial}{\partial z} H_z^j(\vec{r} - \vec{r}_S^j) \right],$$

where the magnetic field H_z^j of the j_{th} dipole of the sample at the tip apex is [45]:

$$H_z^j(\vec{r} - \vec{r}_s^j) = \frac{3(z - z_s^j)(\vec{m}_s^j \cdot (\vec{r} - \vec{r}_s^j))}{\left| \vec{r} - \vec{r}_s^j \right|^5} - \frac{m_{sz}^j}{\left| \vec{r} - \vec{r}_s^j \right|^3}.$$

Moving the tip above the magnetic structure at some height and calculating in every point the phase shift $\Delta\varphi = QF_z'/k$, it is possible to model the MFM image.

The results of modeling calculations of the MFM image for a homogeneously magnetized particle in form of an elliptic cylinder are presented in Fig. 92 as an example.

(a)   **(b)**
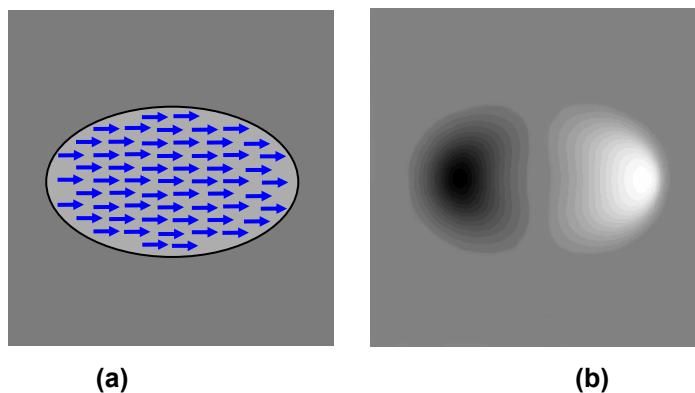
Fig. 92. Modeling of the MFM image of a homogeneously magnetized particle:
(a) – magnetization distribution in the particle;
(b) – corresponding MFM image

The experimental MFM image of an organized array of magnetic particles with elliptic form is presented in Fig. 93.
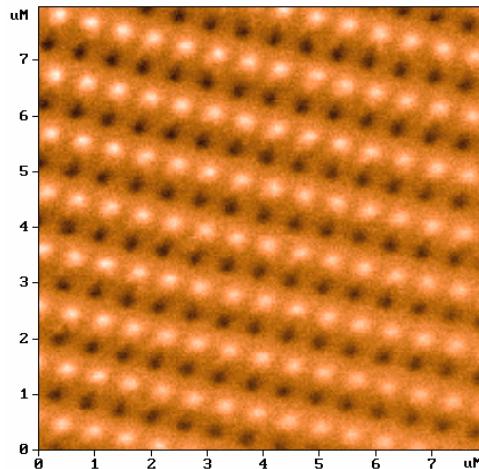
Fig. 93. MFM image of an array of magnetic nanoparticles,
formed by interferential laser annealing of Fe-Cr films [46]

AFM, EFM, MFM control system (oscillatory techniques)

A simplified circuit of AFM, EFM, MFM control system is presented in Fig. 94. Analog switches SW1 – SW5 are controlled by the voltages supplied from the output register (OR) and serve for configuration of the control system. A Voltage-Controlled-Oscillator (VCO) generates a sinewave driving the cantilever oscillations. The amplitude and frequency values of the driving signal are set by a DAC-O converter. Mechanical cantilever oscillations are excited by the piezo-vibrator (PV). The amplitude and the phase of these oscillations are detected by a synchronous detector (SD).

At the first stage the amplitude-frequency characteristics $A(\omega)$ and phase response $\varphi(\omega)$ of the "free" cantilever (far from surface) are measured. For this purpose the switch SW2 is closed, the switch SW3 is open, and the VCO output is fed to the piezo-vibrator and simultaneously to the synchronous detector as reference voltage. The laser beam reflected by the vibrating cantilever produces in the splitted photodiode (PD) a current with an a.c. component at the driving frequency. A sawtooth voltage, produced by DAC-O, sweeps the oscillator frequency in the range selected by the operator. The photodiode current is converted by the preamplifier (PA) into a signal supplied to the synchronous detector. The amplitude and the phase of the signal (synchronously with the DAC-O voltage) are recorded by the ADC in the computer memory. Then the amplitude $A(\omega)$ and phase response $\varphi(\omega)$ are displayed on the computer monitor.

The AFM images in contactless and "semi-contact" modes are built as follows. The VCO sets the forced oscillation frequency of the cantilever close to resonance. The oscillation amplitude is measured by the synchronous detector, and the output voltage U, proportional to the amplitude, is fed to the input of the differential amplifier (DA). A voltage U_0, ($U_0 < U$), set by the operator through DAC-Set, is compared to the voltage U and the feedback loop is closed through the switch SW4. The feedback moves the scanner bringing the sample towards the tip until the cantilever oscillation amplitude decreases so that the U voltage becomes equal to U_0. During sample scanning the oscillation amplitude is kept at the set level, and the control voltage in the feedback circuit is recorded as AFM image in the computer memory.

When the tip-sample distance decreases, the oscillation amplitude decreases due to the resonance curve shift caused by the increase of the force gradient. Therefore the AMF image, obtained keeping constant the cantilever oscillation, represents a surface of a constant force gradient, which, in absence of electric and magnetic interactions, is determined by van der Waals forces and coincides to a high accuracy with the surface topography. The phase signal is frequently recorded simultaneously with the surface topography. This allows to plot AFM images of phase contrast and to analyze the elastic properties of a surface in the "semi-contact" mode.
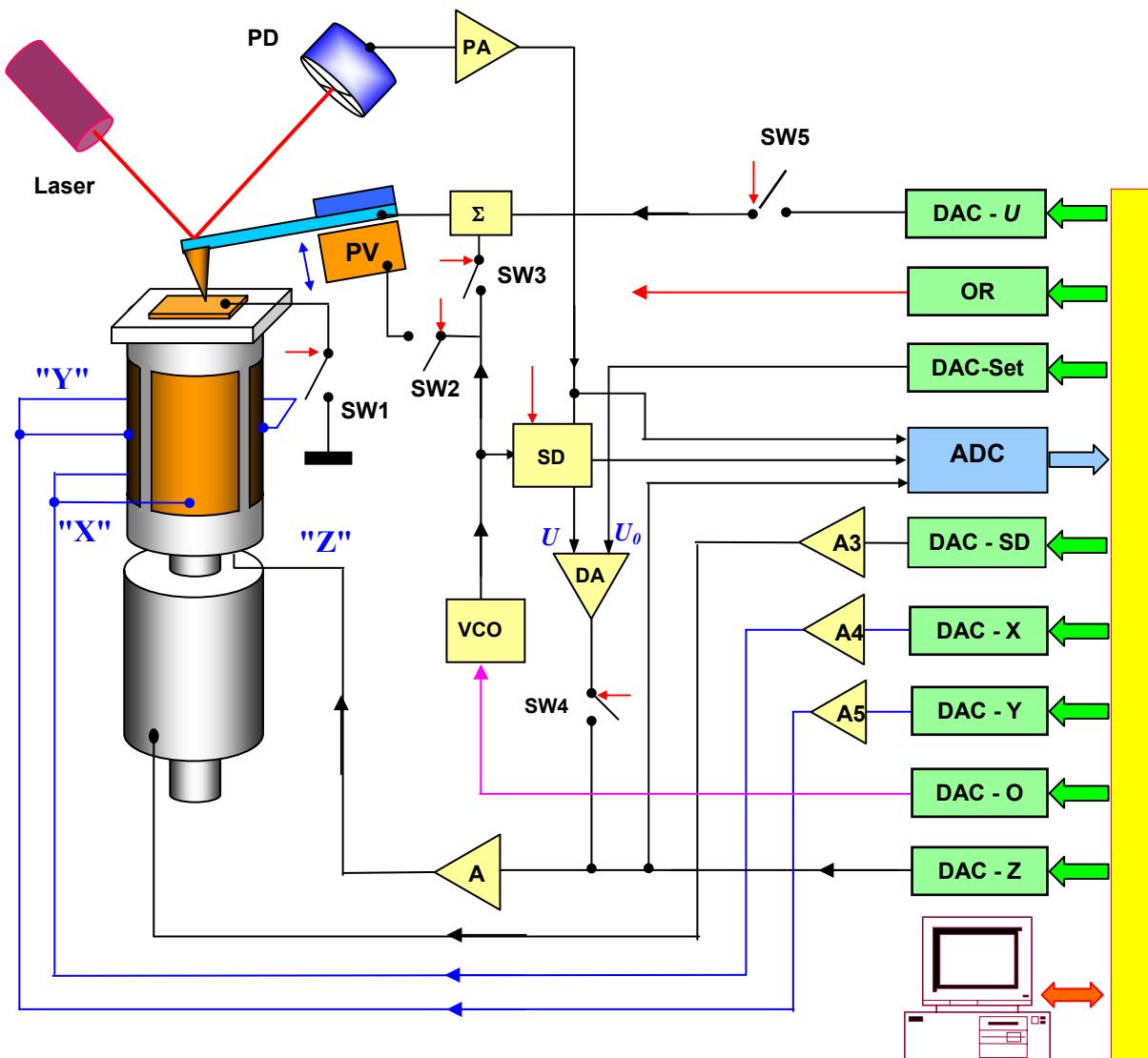

Fig. 94. Simplified schematic of the AFM, EFM, MFM control system

Investigation of magnetic samples is performed using special tips with a magnetic coating, and using the two-pass technique. During the first pass the surface topography is recorded in each scanning line in "semi-contact" mode. On the second pass the feedback is broken, and during scanning the probe is moved (under the control of a signal produced by DAC-Z) above a sample at a preset height with a trajectory repeating the recorded topography. Since the average tip-sample distance is constant in every point, changes of amplitude and phase of the cantilever oscillation will be due only to the changes of the gradient of the magnetic force acting between the tip and the surface.

Using conducting tips allows to investigate the local electric properties of samples in the EFM mode. In this case the sum of the a.c. voltage from the VCO and of a constant voltage from *DAC-U* (through switch SW5) is fed to the tip. The sample is grounded through the switch SW1. Cantilever oscillations are excited by the periodic electric force between the tip and the sample. The amplitude and the phase of oscillations at the driving frequency ω and at frequency 2ω are measured by the synchronous detector, using the two-pass technique. During the first pass the surface topography is recorded. On the second pass the tip moves following the recorded topography, at some distance above the surface, and the signal amplitude changes at frequency 2ω are recoded in the computer memory as a map of $C_z'(x,y)$, i.e. the derivative of the tip-sample system capacity with respect to the tip-sample distance. To measure the local surface potential using the Kelvin-probe method, the constant voltage component is changed by the *DAC-U* in each point of scanning until the oscillation amplitude at the driving frequency ω becomes equal to zero. The voltage corresponding to the given condition is recorded in the computer memory to build the surface potential image $\varphi(x,y)$.

2.5. Near-field optical microscopy

Traditional modes of optical images acquisition have essential restrictions due to the light diffraction. One of the basic laws of optics is the existence of the *diffraction limit* that sets the minimal size *R* of an object, whose image can be constructed by an optical system using light with wavelength λ:

$$R \approx \frac{\lambda}{2\,n} \; ,$$

where n is the index of refraction of the material surrounding the object. For the visible range of wavelengths the limit size is about 200÷300 nanometer. Different methods for image construction are used in the near-field optical microscopy. These methods allow to overcome the diffraction limit and to obtain a spatial resolution of the order of 10 nanometers.

The Scanning Near-Field Optical Microscope (SNOM) was invented by Dieter Pohl (IBM Laboratory, Zurich, Switzerland) in 1982 immediately after the invention of the tunneling microscope. The principle of operation of this device is based on the phenomenon of light passage through sub wavelength diaphragms (apertures with a diameter that is much less than a wavelength of the incident radiation).
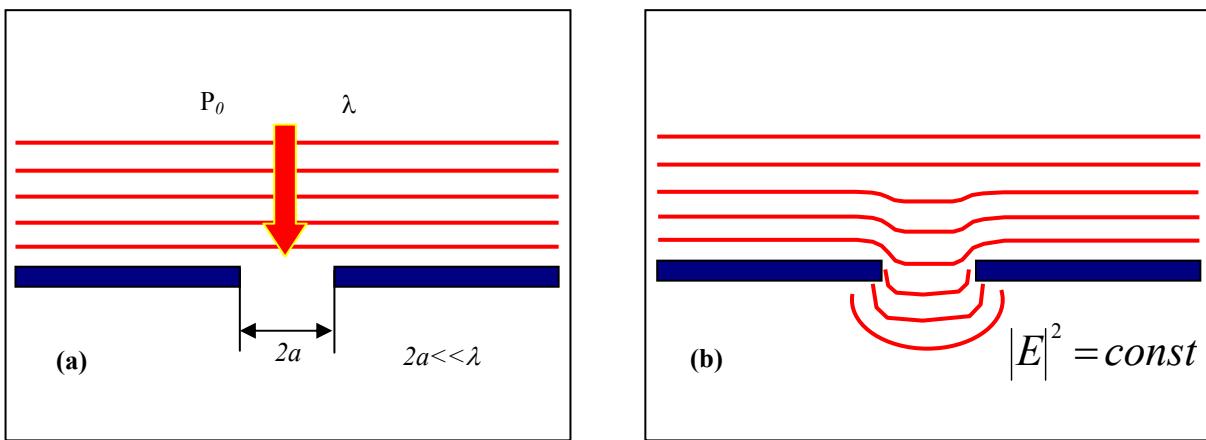
Fig. 95. (a) - Passage of light through an aperture in the screen with sub-wavelength size, (b) - Lines of constant intensity of optical radiation in sub wavelength aperture area

During the passage of light through a sub wavelength aperture a number of features are observed [47,48]. The electromagnetic field near the aperture has a complex structure. The so-called near-field region is located directly behind an aperture within the range $Z < 100\ a$, where the electromagnetic field exists as localized evanescent (not propagating). In the far-field region ($Z > 100\ a$) only radiating modes are observed. Radiation power behind a sub-wavelength aperture in the far-field region can be estimated with the following formula [48]:

$$P_{tr} = \frac{128}{27\pi} k^4 a^6 W_0 \; ,$$

where k is the wave vector, W_0 the incident radiation power density. Estimations show that for radiation with a wavelength of the order of 500 nanometers and diaphragms with aperture of about 5 nanometers the radiation power in the far-field region is about 10 orders of magnitude less than the incident radiation power. Therefore, at first sight it seems that the use of small apertures to obtain raster optical images is practically impossible. However, if the investigated object is placed directly behind an aperture in the near-field region, then due to the interaction of evanescent modes with the sample, part of the energy of the electromagnetic field transforms into radiating modes, which intensity can be recorded by a photodetector. Thus, the near-field image is formed by scanning the sample with a sub-wavelength diaphragm and by recording the intensity distribution of optical radiation as a two dimensional function of the diaphragm position $I(x,y)$. The SNOM image contrast is determined by processes of reflection, refraction, absorption and dispersion of light, which in turn depend on the local optical properties of the sample.

SNOM tips obtained from an optical fiber

Currently there are several schemes for constructing a near-field optical microscope. SNOM with tips made from an optical fiber, representing an axially-symmetrical optical waveguide, have found the widest application (Fig. 96).
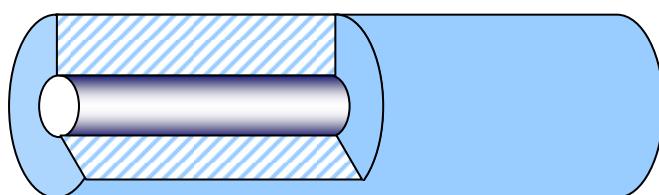

Fig. 96. Schematic drawing of an optical fiber structure

The optical fiber consists of a core and a cladding, plus an outer protective layer. As a rule, the core and the cladding are made of a special quartz glass. In this case the glass that is used for cladding has a smaller refractive index with respect to that of the core glass. (In practice the refractive index of glass is adjusted by adding elements so refractive indexes of core and cladding differ on about 1 %). Due to total internal reflection, such system allows to localize optical radiation in the core area and to transport it on large distances practically free of losses.

Tips for the SNOM are made as follows (see for example [49]). The end of an optical fiber, with protective layer removed, is immersed in a solution consisting of two immiscible liquids – mixture of HF, NH4F, H2O, which is an etching agent for quartz and a liquid with smaller density (for example, toluene). Toluene settles down atop the etching agent and serves to form a meniscus on the "toluene-etching agent-fiber" border (Fig. 97 (a)). Due to the etching, the fiber thickness decreases, resulting in reduction of the meniscus height. As a result, formation of a cone-shaped apex on the end of the fiber occurs during etching (Fig. 91 (b)). This apex has characteristic sizes of less than 100 nanometers. Then the apex of the tip is coated with a thin layer of metal. The overcoating is made by vacuum spraying at the angle of about 30º to the fiber axis so that the small aperture area remains uncovered on the apex in the shadow area. This area is the near-field source of radiation. The optimum angle at the apex of the tip is about 20º.
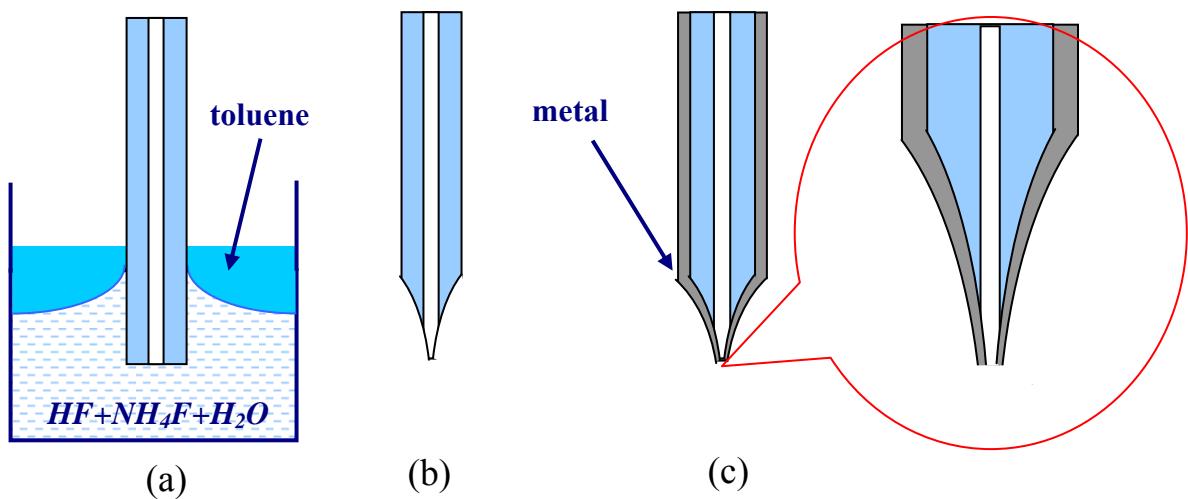
Fig. 97. Manufacturing of SNOM tips from optical fiber:

(a) - chemical etching of fiber;
(b) – appearance of a fiber apex after etching;
(c) –thin metal film evaporation.

"Shear-force" mode of monitoring the tip–surface distance in SNOM

During SNOM operation it is necessary to keep the tip above the surface at distances of about 10 nanometers and less. This can be achieved with different techniques; however the prevailing solution uses the SNOM in the so-called "shear force" mode.
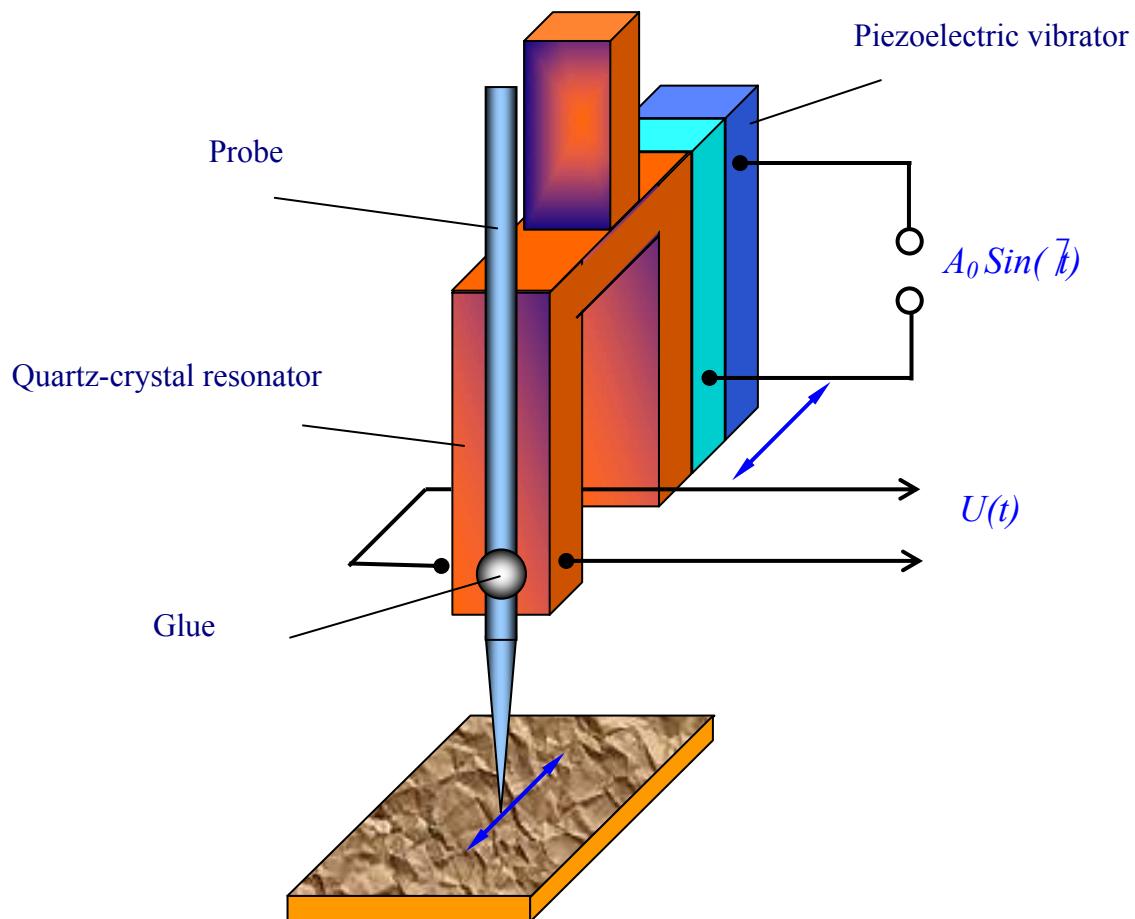
Fig. 98. "Shear-force" scheme of a tip-surface distance probe based on a tuning fork

Most often the "shear-force mode uses a piezoelectric transducer to drive a "tuning fork" (Fig. 98). The SNOM tip is glued to a quartz-crystal resonator ("fork"). The fork forced oscillations with a frequency close to the resonant frequency of the "tip+quartz resonator" system are induced by the piezoelectric vibrator. Thus the tip makes oscillatory movements in parallel with the sample surface. Measurement of the tip-surface interaction force is made by recording the changes of amplitude and phase shift (with respect to the driving voltage $U(t)$ applied to the piezo electrodes).

The theory of "shear force" control is complex enough, so here we give only a qualitative description. During the tip-sample approach several effects are observed. Firstly an additional dissipative interaction of the tip with the surface occurs, due to viscous friction (in a thin layer of air close to the surface and in a thin layer of adsorbed molecules on the sample surface).

This causes a reduction of the resonance quality factor, and consequently, a reduction of the oscillation amplitude and a broadening of the resonance peak and of the phase response curve.
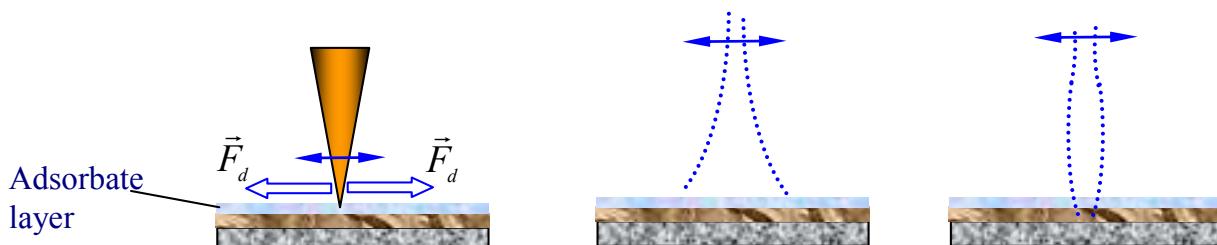
Fig. 99. Dissipative forces affecting the tip, and change of an oscillations mode of the tip near to the surface of a sample

Secondly, a change of the oscillations mode occurs at small tip-surface distances. The oscillation mode at large distance corresponds to oscillations of a rod with a free end, while at small distance (or with the tip in contact with the surface) it changes into oscillations of a rod with a fixed end. This causes an increase of the resonance frequency, i.e. the amplitude-frequency curve shift towards higher frequencies [50,51]. Changes of amplitude and phase of bending vibrations in the tip-resonator system are used as feedback signals to control the tip-surface distance in SNOM.

SNOM configurations

Several SNOM configurations were used and described in the literature [52]. The main SNOM configurations are shown schematically in Fig. 100.
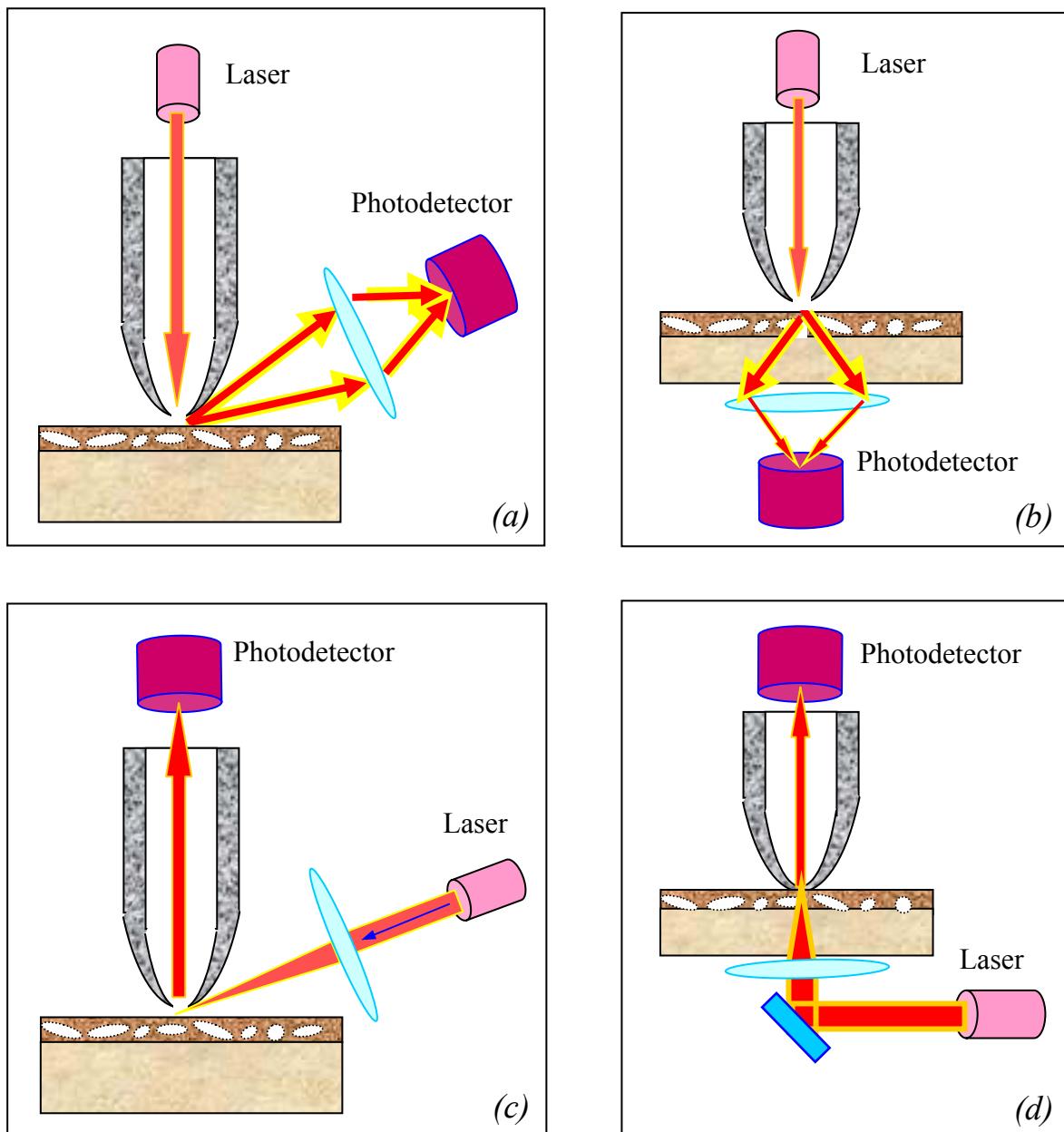
Fig. 100. Possible configurations of a near-field optical microscope

The arrangement in which optical radiation of the laser is localized in space by a fiber tip is the most frequently used. Such arrangement allows to receive the maximal emission power in the sub-wavelength aperture area and allows to investigate the sample both in reflection (Fig. 100 (a)), and in transmission (Fig. 100 (b)). The emission reflected from the sample or transmitted through the sample is focused onto a photodetector by a mirror or a lens to increase the sensitivity. This SNOM configuration is widely used in near-field optical lithography.

In experiments, when high levels of optical pumping are required (for example to study local nonlinear properties), a different configuration is used, in which powerful laser radiation is directed on the sample, and the radiation (reflected or transmitted) is collected by a near-field tip (Fig. 100 (c), (d)).
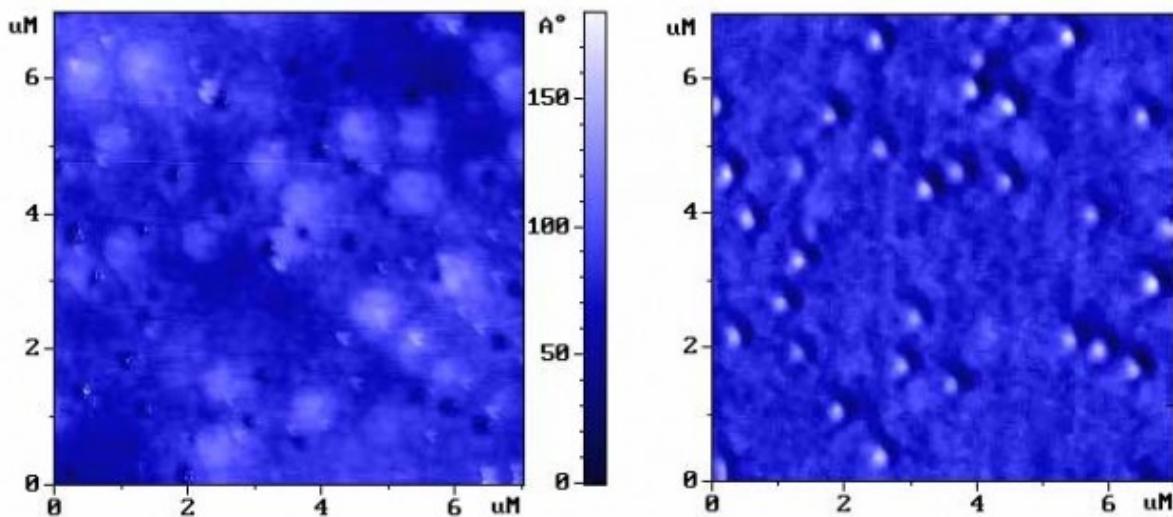
Fig. 101. ″Shear force″ topography (left) , and the near-field optical image (right) of a sample with InAs quantum dots [54]

The AFM/SNOM image (topography) of an InAs/GaAs sample with quantum dots acquired by a microscope working in the configuration shown on Fig. 100 (a) [54] is shown in Fig. 101. The HeCd laser (λ = 442 nm) was used in the experiment. The near-field optical image represents the accumulation of the radiation reflected from the sample surface and the luminescent emission that corresponds to the transition between levels of dimensional quantization in InAs dots.

A less widespread configuration, where both sample illumination and collection of the near-field emission are carried out through the tip, is presented in Fig. 102.
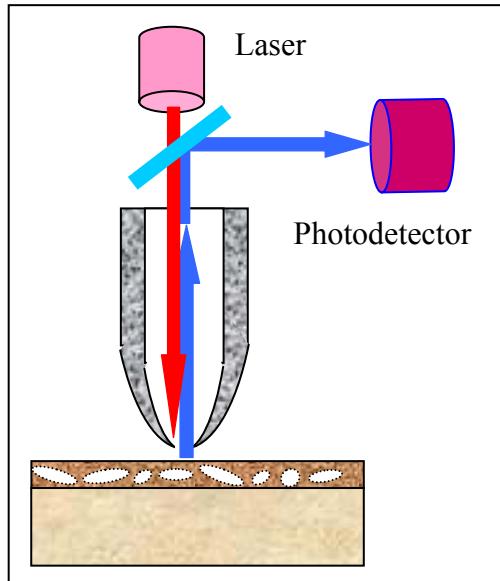
**Fig. 102. The SNOM scheme where the sample illumination
and the collection of emission are carried out by the same tip**

Such combination of a near-field source with a near-field receiver is a rather promising method providing very high spatial resolution. However, in this arrangement the radiation passes twice through a subwavelength aperture. As a result, the signal reaching the photodetector has a very low intensity, and hence high-sensitivity detection methods are required.

Integration of the SNOM with a monochromator allows to carry out local spectroscopic studies.

Typical applications of near-field optical microscopes are studies of local optical and photoelectric properties of semiconductor, of biological objects, and nanotechnology.

Conclusion

The fundamentals of scanning probe microscopy were briefly resumed in this study guide. Principles of operation of the basic types of probe microscopes, most widely used in scientific researches, were described (scanning tunneling microscope, atomic-force microscope, electric-force microscope, magnetic-force microscope, near-field optical microscope). There is a number of other devices working on the SPM principles left outside the scope of this book, and a large number of techniques using SPM.

The SPM development basic stages are partially described in the chronological table [53] on the next page of the book: it cannot be exhaustive because the scanning probe microscopy is today a rapidly developing technique.

Basic stages of SPM development

1981 - *Scanning tunneling microscope*. G. Binnig, H. Rohrer.
    Atomic resolution images of conducting surfaces.

1982 - *Scanning near-field optical microscope*. D. W. Pohl.
    Resolution of 50 nanometers in optical images.

1984 - *Scanning capacitive microscope*. J. R. Matey, J. Blanc.
    500 nm (lateral resolution) images of capacitance variation.

1985 - *Scanning thermal microscope*. C. C. Williams, H. K. Wickramasinghe.
    Resolution of 50 nm in thermal images.

1986 - *Atomic-force microscope*. G. Binnig, C. F. Quate, Ch. Gerber.
    Atomic resolution on non-conducting (and conducting) samples.

1987 - *Magnetic-force microscope*. Y. Martin, H. K. Wickramasinghe.
    Resolution of 100 nanometers in magnetic images.

   - *"Frictional" force microscope.* C. M. Mate, G. M. McClelland, S. Chiang.
    Atomic-scale images of lateral ("frictional") forces.

   - *Electric force microscope*. Y. Martin, D. W. Abraham, H. K. Wickramasinghe.
    Detecting of single charges on a sample surface.

   - *Inelastic tunneling STM spectroscopy*. D. P. E. Smith, D. Kirk, C. F. Quare.
    Detection of phonon spectra of molecules in STM.

   - *Laser driven STM.* L. Arnold, W. Krieger, H. Walther.
    Imaging by non-linear mixing of optical waves in STM.

1988 - *Ballistic electron emission microscope*. W. J. Kaiser.
    Schottky barriers investigation with nanometer resolution.

   - *Inverse photoemission microscope*.
    J. H. Coombs, J. K. Gimzewski, B. Reihl J. K. Sass, R. R. Schlittler
    Detection of luminescence spectra on nanometer scales.

1989 – *Near-field acoustic microscope*.
    K. Takata, T. Hasegawa, S. Hosaka, S. Hosoki. T. Komoda
    Low-frequency acoustic measurements with the resolution of 10 nanometers.

   - *Scanning noise microscope*. R. Moller A. Esslinger, B. Koslowski.
    Detection of tunnel current without voltage bias.

   - *Scanning spin - precession microscope*.
    Y. Manassen, R. Hamers, J. Demuth, A. Castellano.
    Visualization of spin in a paramagnetics with 1 nm resolution.

   - *Scanning ion-conductance microscope*.
    P. Hansma, B. Drake, O. Marti, S. Gould, C. Prater.
    Imaging in electrolyte with 500 nm resolution.

   - *Scanning electrochemical microscope*.
    O. E. Husser, D. H. Craston, A. J. Bard.

1990 - *Scanning chemical potential microscope.*
      C. C. Williams, H. K. Wickramasinghe.

      Atomic scale images of chemical potential variation.

  - *Photovoltage STM.* R. J. Hamers, K. Markert.
      Photovoltage images on nanometer scale.

1991 - *Kelvin probe force microscope.*
      N. Nonnenmacher, M. P. O'Boyle, H. K. Wickramasinghe.
      Measurements of surface potential with 10 nm resolution.

1994 – *Apertureless near-field optical microscope.*
      F. Zenhausern, M. P. O'Boyle, H. K. Wickramasinghe.
      Optical microscopy with 1 nm resolution.

REFERENCES

1.   D.Sarid - "Scanning Force Microscopy: With Applications to Electric, Magnetic and Atomic Forces", Publisher: Oxford Univ. Pr., 1994.

2.   R.Wiesendanger - "Scanning Probe Microscopy and Spectroscopy: Methods and Applications", Publisher: Cambridge Univ. Pr., 1995.

3.   D.Sarid - "Exploring Scanning Probe Microscopy With Mathematica", Publisher: John Wiley & Sons, 1997.

4.   "Scanning Probe Microscopy: Analytical Methods" Editor: R.Wiesendanger, Publisher: Springer Verlag, 1998.

5.   M.Paesler, P.Moyer - "Near-field Optics: Theory, Instrumentation and Applications" Publisher: John Wiley & Sons Inc, 1996.

6.   "Advances in Scanning Probe Microscopy" (Editors: T.Sakurai, Y.Watanabe) Publisher: Springer Verlag, 2000.

7.   D.A.Bonnell - "Scanning Tunneling Microscopy and Spectroscopy" Publisher: John Wiley & Sons Inc., 2001.

8.   E.Meyer, H.Hug, R.Bennewitz - "Scanning Probe Microscopy: The Lab on a Tip" Publisher: Springer-Verlag Berlin and Heidelberg GmbH & Co. K, 2003.

9.   K.S.Birdi - "Scanning Probe Microscopes: Applications in Science and Technology" Publisher: CRC Press, 2003.

10.   D.Courjon - "Near Field Microscopy and Near Field Optics" Publisher: Imperial College Press, 2003.

11.   B.Bhushan, H.Fuchs, S.Hosaka (eds.) - "Applied Scanning Probe Methods (Nanoscience and Technology)" Publisher: Springer Verlag; 2004.

12.   "Atomic Force Microscopy: Biomedical Methods and Applications (Methods in Molecular Biology) - Detailed methods for investigating biological structure" Editors: Pier Carlo Braga & Davide Ricci Publisher: Humana Press; 2004.

13.   "Springer Handbook of Nanotechnology" (Editor: B.Bhushan) Publisher: Springer-Verlag Berlin and Heidelberg GmbH & Co. K, 2004.

14.   G.Binnig, H.Rohrer - "Scanning tunneling microscopy". // Helv. Phys. Acta, vol. 55, # 6, p. 726 – 735 (1982).

15.   G.Binnig, H.Rohrer, Ch.Gerber, E.Weibel - "Tunneling through a controllable vacuum gap". // Appl. Phys. Lett., vol. 40, p. 178 (1982).

16.   "Ultrasound. The small encyclopedia". (Edited by I.P.Goljamin) // Moscow, "Sovetskaya entsiklopediya", 1979.

17.   P.M.Williams, K.M.Shakesheff et al. – "Blind reconstruction of scanning probe image data". // J. Vac. Sci. Technol. B 14 (2) p. 1557-1562 (1996).

18.   A.A.Bukharaev, N.V.Berdunov, D.V.Ovchinnikov, K.M.Salikhov - "Three-dimensional probe and surface reconstruction for atomic force microscopy using a deconvolution algorithm" // Scanning Microscopy, vol. 12, # 1, p. 225-234 (1998).

19.   D.I.Blohintsev – "Fundamentals of quantum mechanics", Moscow, Nauka, 1983.

20. L.D.Landau, E.M.Lifshits - "Quantum Mechanics: non-relativistic theory".
Publisher: Pergamon Press, Oxford, New York, 1977.

21. J.G.Simons – "Generalized formula for the electric tunnel effect between similar electrodes separated by a thin insulating film". // J. Appl. Phys., 34, 1793 (1963).

22. J.G.Simons-"Electric tunnel effect between dissimilar electrodes separated by a thin insulating film". // J. Appl. Phys., 34, 2581 (1963).

23. J.Tersoff and D.R.Hamann – "Theory and application for scanning tunneling microscope". // Phys. Rev. Lett. vol. 50, p. 1998-2001 (1983).

24. J.Tersoff and D.R.Hamann - "Theory of the scanning tunneling microscope". // Phys. Rev. B, vol. 31 (2), 805-813 (1985).

25. J.Tersoff – "Method for the calculation of scanning tunneling microscope images and spectra". // Phys. Rev. B, vol. 40 (17), 11990-11993 (1989).

26. G.E.Pikus – "Fundamentals of the theory of semiconductor devices", Moscow, Nauka, 1965.

27. C.B.Duke - "Tunneling in solids", Academic Press, New York, 1969.

28. "Tunneling phenomena in solids", edited by E.Burstein and S.Lundqvist.
Publisher: Plenum press, New York, 1969.

29. R.M.Feenstra, V.Ramachandran, H.Chen – "Recent development in scanning tunneling spectroscopy of semiconductor surfaces". // Appl. Phys., A 72, p. 193 – 199 (2001).

30. A.Rouz-Ins, E.Rederik "Introduction in physics of superconductivity".
Publisher: Moscow, Mir, 1972.

31. G.Binnig, C.F.Quate, Ch. Gerber – "Atomic force microscope". // Phys. Rev. Lett., vol. 56, #9, p. 930 – 933 (1986).

32. J.S.Barash – "Van der Waals forces", Moscow, Nauka, 1988.

33. M.Saint Jean, S.Hudlet, C.Guthmann, J.Berger – "Van der Waals and capacitive forces in atomic force microscopies". // J. Appl. Phys., vol. 86 (9), p. 5245 – 5248 (1999).

34. I.A.Birger, B.F.Shorr, G.B.Iosilevich – "Calculation on strength of details of machines".
Publisher: Mashinostroenie, Moscow, 1979.

35. S.N.Magonov, V.Elings, M.-H.Whangbo – "Phase imaging and stiffness in tapping-mode atomic force microscopy". // Surf. Sci., 375, L385 – L391 (1997).

36. J.P. Cleveland, B. Anczykowski, A.E. Schmid, V.B. Elings – "Energy dissipation in tapping-mode atomic force microscopy". // Appl. Phys. Lett. V. 72 (20), 2613 – 2615 (1998).

37. J.Tamayo, R.Garcia – "Relationship between phase shift and energy dissipation in tapping-mode atomic force microscopy". // Appl. Phys. Lett. V. 73 (20), 2926 – 2928 (1998).

38. J.Tamayo – "Energy dissipation in tapping-mode atomic force microscopy with low quality factors". // Appl. Phys. Lett. V. 75 (22), 3569 – 3571 (1999).

39. J.R.Matey, J.Blanc – "Scanning capacitance microscopy". // J. Appl. Phys., vol. 57, # 5, p. 1437 – 1444 (1985).

40. M.Nonnenmacher, M.P.O'Boyle, H.K.Wikramasinghe – "Kelvin probe force microscopy". // Appl. Phys. Lett., 58 (25), 2921 – 2923 (1991).

41. B.Stiller, P.Karageorgiev, et al. – "Scanning Kelvin microscopy as a tool for visualization of optically induced molecular switching in azobenzene self assembling films".
// Surf. Interface Anal. 30, 549-551, (2000).

42. Y.Martin and H. K.Wickramasinghe – "Magnetic imaging by "force microscopy" with 1000 Å resolution". // Appl. Phys. Lett. vol. 50, # 20, p. 1455-1457 (1987).

43. D.Rugar, H.Mamin, P.Guethner et al. – "Magnetic force microscopy: General principles and application to longitudinal recording media". // J. Appl. Phys., vol. 68, # 3, p.1169 – 1182 (1990).

44. I.E.Tamm - "Fundamentals of the theory of electricity"
Publisher: Moscow, Mir, 1979.

45. L.D.Landau, E.M.Lifshits - "The Classical Theory of Fields"
Publisher: Pergamon Press, Addison-Wesley, New York, 1987.

46. A.Alexeev, V.A.Bykov, A.F.Popkov, N.I.Polushkin, V.I.Korneev - "Remanent state studies of elliptical magnetic particles". // J. Magn. Magn. Mater., vol. 258-259, p. 42-44 (2003).

47. D.W.Pohl, W.Denk, M.Lanz – "Optical spectroscopy: image recording with resolution $\lambda/20$". // Appl. Phys. Lett., vol. 44, p. 651 – 653 (1984).

48. U.Durig, D.W.Pohl, F.Rohrer – "Near-field optical-scanning microscopy". // J.Appl. Phys. vol. 59, # 10, 3318-3327, 1986.

49. V.F.Drjakhlushin, A.J.Klimov, V.V.Rogov, S.A.Gusev – "Scanning near-field optical microscope probe". // Instrumental and Experimental Techniques, vol. 41, # 2, p. 275-276 (1998).

50. P.K.Wei, W.S.Fann – "The probe dynamics under shear force in near-field scanning optical microscopy". // J. Appl. Phys., vol. 83, # 7, p. 3461 – 3468 (1998).

51. D.G.Volgunov, A.V.Buryukov, S.V.Gaponov, V.L.Mironov – "Probe - surface interaction in the piezo-resonator "shear force" microscope". // Physics of Low – Dimensional Structures,
3/4, p. 17-23 (2001).

52. D.Courjon, C.Bainier – "Near field microscopy and near field optics". // Rep. Prog. Phys. 57,
p. 989 – 1028, (1994).

53. H.K.Wickramasinghe – "Progress in scanning probe microscopy". // Acta materialia, 48,
p. 347-358 (2000).

54. Internet site of NT-MDT company: http://www.ntmdt.com/